# DESIGN, ASSEMBLY AND CHARACTERIZATION OF THREE-DIMENSIONAL PHOTONIC BAND GAP STRUCTURES FABRICATED WITH BARIUM TITANATE: STRONTIUM TITANATE: BARIUM ZIRCONATE MIXTURES

By

SAROSH SRIKANTH NADKARNI

Bachelor of Technology in Chemical Engineering

Osmania University

Hyderabad, India

2001

Submitted to the Faculty of the
Graduate College of the
Oklahoma State University
in partial fulfillment of
the requirements for
the Degree of
DOCTOR OF PHILOSOPHY
December, 2006

DESIGN, ASSEMBLY AND CHARACTERIZATION OF THREE-DIMENSIONAL PHOTONIC BAND GAP STRUCTURES FABRICATED WITH BARIUM TITANATE: STRONTIUM TITANATE: BARIUM ZIRCONATE MIXTURES

Dissertation Approved:

Dr. James E. Smay

Dissertation Adviser

Dr. R. Russell Rhinehart

Dr. Khaled Gasem

Dr. Bruce J. Ackerson

Dr. Marty High

Dr. A. Gordon Emslie

Dean of the Graduate College

ACKNOWLEDGEMENTS

First and foremost, I would like to thank my parents for their faith in me and the love and support that I have received from them over the years, which made it possible for me to pursue my dreams and aspirations. I would like to thank my wife Asma for all the love and joy that she has given me during our time in graduate school together and continues to give and for always having a positive outlook. She inspires me to do my best and reach further than I would ever have imagined.

I am grateful to my advisor, Dr. Jim Smay, for his guidance and support during my Ph.D. Dr. Smay has always been a great inspiration to me in his work ethics. He sets high standards and motivates people working with him to strive harder and develop skills on multiple fronts. I have enjoyed my discussions with him in the lab whether they be technical or non-technical in nature and they have made my time in the lab much more enjoyable and pleasant. I have really enjoyed the open and friendly atmosphere that he has maintained in the group. I look forward to my association with him in the years to come. I would like to thank my committee for their time and help. I have been fortunate that I have been able to approach them "on demand" and ask questions which they always satisfactorily addressed. For this I owe deep gratitude to Dr. Bruce Ackerson, Dr. Khaled Gasem, Dr. Marty High, and Dr. Russell Rhinehart. Of these I have had the

pleasure of taking classes with Dr. Gasem and Dr. Rhinehart and have enjoyed their teaching styles immensely.

I have also been fortunate to have collaborated with some of the finest technical experts in their various fields. I would like to express my appreciation to Dr. Paul Clem and Dr. Jennifer Sigman at Sandia National Laboratories for their help and discussions on the dielectric characterization work. I would also like to thank Dr. Rana Biswas at Ames Laboratory for his modeling results on the photonic crystals and helpful suggestions. I specially thank Dr. Weili Zhang and Dr. Abul Azad at Oklahoma State University for their assistance with the time domain spectroscopy measurements. This work would not have been possible without the help of all these people.

I would like to specially thank Genny, Eileen, Carolyn and Mindy for all the help and assistance that they have given me in the Chemical Engineering office. I have always appreciated the pleasant and cheerful atmosphere in the chemical engineering office and I will dearly miss it. Finally, I would like to thank all my friends for their support.

TABLE OF CONTENTS

LIST OF TABLES

LIST OF FIGURES

# 1. INTRODUCTION

## 1.1.Overview

This dissertation summarizes efforts to design, fabricate, and characterize three-dimensional tunable photonic band gap (PBG) crystals operating in the microwave regime using a direct write, colloidal gel (ink) deposition process. A complex oxide dielectric consisting of a mixture of barium titanate (BT), strontium titanate (ST), and barium zirconate (BZ) ceramics was investigated for this purpose. The project may be sub-divided into three specific areas:

### *1.1.1. Processing*

Inks of BT, ST, and BZ were formulated with the goal of compatible mixing in various molar ratios in the direct write process hitherto referred to as robocasting. The studies required for understanding the relevant process variables included rheology (steady shear and oscillatory), zeta potential analysis, flocculation behavior of ceramic slurries and analysis of inorganic salts and poly(electrolytes) for dispersion-flocculation behavior, co-deposition, co-firing, microstructure analysis, and phase analysis by X-ray diffraction.

### *1.1.2. Electro-optic characterization*

A PBG crystal was designed based on the dielectric constant and tunability of the BT-ST-BZ mixture used. A combinatorial technique enabled by the robocasting process was used to screen for the appropriate molar ratios of these materials. The dielectric constant, loss, and tunability were analyzed via capacitance measurement techniques and refractive index/loss measurements using terahertz-time domain spectroscopy (THz-TDS).

### *1.1.3. Fabrication and characterization of the tunable PBG crystal*

Using the appropriate BT-ST-BZ mixture, a 3-D PBG crystal based on a priori calculations of the band gap was fabricated using the robocasting process. The PBG crystal was tested in transmission mode using THz-TDS measurement technique.

## 1.2.Project description

Semiconductor technology has revolutionized computing and electronics in the last century leading to advancements in the fields of health care, information technology, communications, space travel and countless others. However, progress in electronic device performance is approaching a bottleneck in terms of the signal bandwidth and speeds. High frequency electronic devices can produce significant ohmic heating losses prohibiting the creation of faster computers or lossless communications which limit progress in information processing. The use of electromagnetic (E.M.) waves to transmit (e.g. fiber optics) and process data may remove this bottleneck and seed next generation technologies. Photons have minimal material interaction away from absorption bands as

compared to electrons. Furthermore, photons travel at great speeds, allowing faster transmissions and may possess higher frequencies allowing for greater amount of signal to be carried per unit time. Fiber optic systems already carry photonic transmissions across distances as large as oceans with minimal signal losses. These cables use total internal reflection, where signals are not allowed to deviate from the cable path. It is well known that, below the minimum bending radius, the light guiding characteristic of the fiber optic cable can be compromised. While long range data transmission by photons is a realized technology, the inability to efficiently pack optical systems on a "chip" limits their acceptance for replacing the electronic processor. In fact, optically transmitted data are converted to an electronic signal at the termination of the optical cable for further processing. The success of electronic processing is firmly based on the existence of transistors. For a competitive optical processor to exist, a light analogue of the transistor coupled with efficient light guiding must be invented.

Photonic crystals are devices which offer hope that optical transistors and efficient light guides may be realized. Photonic crystals are one-, two-, or three-dimensional periodic arrangements of dielectric materials with certain symmetries that can selectively control propagation of electromagnetic radiation of specific frequencies and directions.[1] As E.M. waves transmit through the structure, periodicity of the dielectric constant establishes certain selective E.M. modes (i.e., frequency and direction).[2] These E.M. modes are allowed to propagate through the crystal whereas the rest are either reflected or can be guided along strategically placed defects. This control over selective transmission of radiation frequencies may be harnessed to create an optical filter for photonic signals similar to a transistor regulating the flow of electronic ones.

The nature of light guiding in photonic crystals is phenomenologically different from fiber optic systems. The former is due to a macroscopic variation in dielectric constant leading to scattering whereas the latter relies on a total internal reflection effect due to electronic transitions at the atomic level. Furthermore, photonic crystals may be used to cause sharp $90^{\circ}$ bends in propagation direction over very short distances (e.g., 1/2 wavelength), offering hope for space-efficient light circuits.

Potential photonic crystal devices may include[1]

- reflecting dielectrics: to design a band stop filter
- resonant cavities: to prevent loss of EM radiation
- waveguides: lossless guiding of EM radiation through predetermined channels

Together these may be used to make devices (such as high speed optical computers, photonic integrated circuits), prevent radiation losses in applications (such as microwave antennas, LASERS, light emitting diodes) and thereby provide applications in multiple fields.


Figure 1.1 Classification of photonic crystals into 1-D, 2-D, and 3-D depending on direction of periodicity and propagation of E.M. waves

Figure 1.1 shows a broad classification scheme for photonic crystals.[1] Periodicity of the two phases, comprising the photonic crystal, may occur in 1, 2, or 3 dimensions. Under constraints of symmetry the propagation of E.M. waves is prohibited in as many directions and the structures are appropriately labeled as 1-D, 2-D and 3-D photonic crystals respectively. Scattering due to a contrast in the refractive index at the dielectric interfaces leads to the phenomena of a photonic band gap. As E.M. waves traverse the photonic crystal and scatter at regular intervals (due to a regular periodicity in arrangement of interfaces), a periodic potential is introduced. A density of states with respect to the energy or frequency of the transmission is established. A zero density of state is a photonic band gap- a frequency band of radiation which is not permitted to exist in the direction of propagation within the crystal and either reflects back or may be guided along defects. Other frequencies transmit unhindered, only attenuated due to loss mechanisms in the material.

Significant work at Sandia National Laboratories by Lin *et al.*[3] resulted in the fabrication of a 3-D photonic crystal operating at infrared frequencies. Standard microelectronic fabrication techniques were utilized to fabricate a photonic crystal using a layer by layer assembly process.[3] The resulting structure was a woodpile style lattice with a face centered tetragonal symmetry made of polycrystalline silicon.

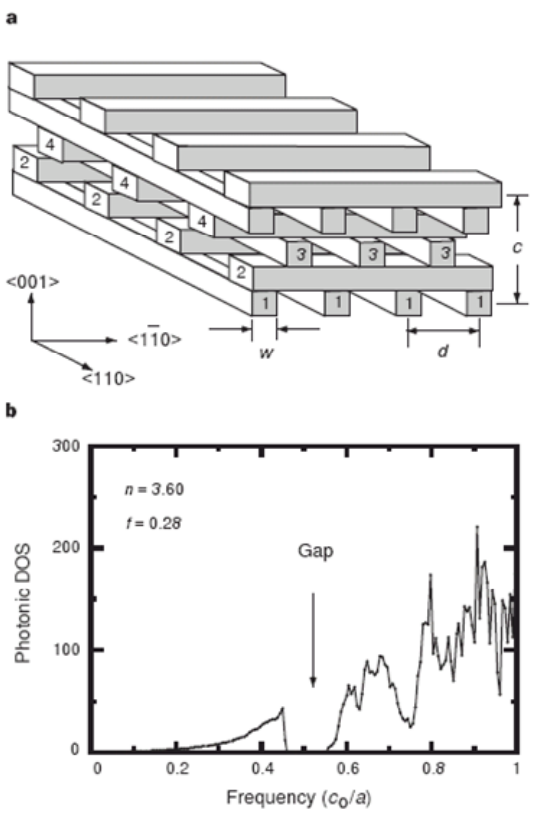


Figure 1.2 Structure and properties of a photonic crystal fabricated at Sandia (a) Diagram of the layer by layer 3-D photonic crystal, and (b) Computed photonic density of states plotted as a function of frequency in the units of co/a

Figure 1.2(a) is a schematic showing the arrangement of the rods in the photonic crystal and Figure 1.2(b) shows the computed photonic density of states (DOS) and the predicted existence of a complete band gap for frequencies ranging from $0.46c_o/a$ to $0.56$ $c_o/a$ where $c_o$ is the velocity of light in vacuum and a is the lattice constant (represented as c in Figure 1.2(a)). The band edge frequencies (lower and upper) and band width depend on two primary factors[4] (i) the refractive index contrast between the materials comprising the crystal (usually crystals consist of an arrangement of a high refractive

index material in air to provide sufficient contrast) and, (ii) the structure of the crystal i.e. the periodicity, lattice spacing and dimensions. The classical treatment of electromagnetic waves in periodic dielectric, isotropic and non-magnetic media by Maxwell's equations is appropriate for modeling photonic crystals.[1, 2, 4, 5] Mathematically and physically the photonic band gap frequencies scale inversely with the dimensions of the photonic crystal and the refractive index contrast.[1, 4] Therefore, a photonic crystal of a given geometry, with millimeter dimensions, exhibiting a band gap in the microwave regime may be used to test proof of concept for finer structures, on the micron scale, having band gaps in the infrared regime.

Commercial photonic crystal fabrication will most probably employ high throughput semiconductor fabrication techniques already in place. However, theoretical modeling has outpaced materials and design testing. High end fabrication techniques such as lithography are expensive to test incremental changes in design and have a limited materials palette. Solid freeform fabrication (SFF) is a rapid prototyping process whereby objects and shapes may be fabricated in a layer by layer assembly process based on a computer aided design (CAD). SFF has already been used to print the types of three-dimensional, periodic structures necessary for photonic crystals.[6-8] SFF techniques are relatively inexpensive, can precisely control macroscopic photonic crystal structure, and can use a broad array of materials. An extrusion based robotic deposition process also known as Robocasting [9, 10] is one such SFF method that utilizes aqueous, colloidal gel inks to print three dimensional structures. Colloidal gel inks for the robocasting process need to satisfy two important criteria[10]:

(i) They must be able to flow through fine deposition nozzles while being able to maintain shape and elastic properties on extrusion to print 3-D patterns: inks must possess shear thinning with yield stress rheology

(ii) They must possess a high solids concentration to resist drying stresses to prevent cracking and warping

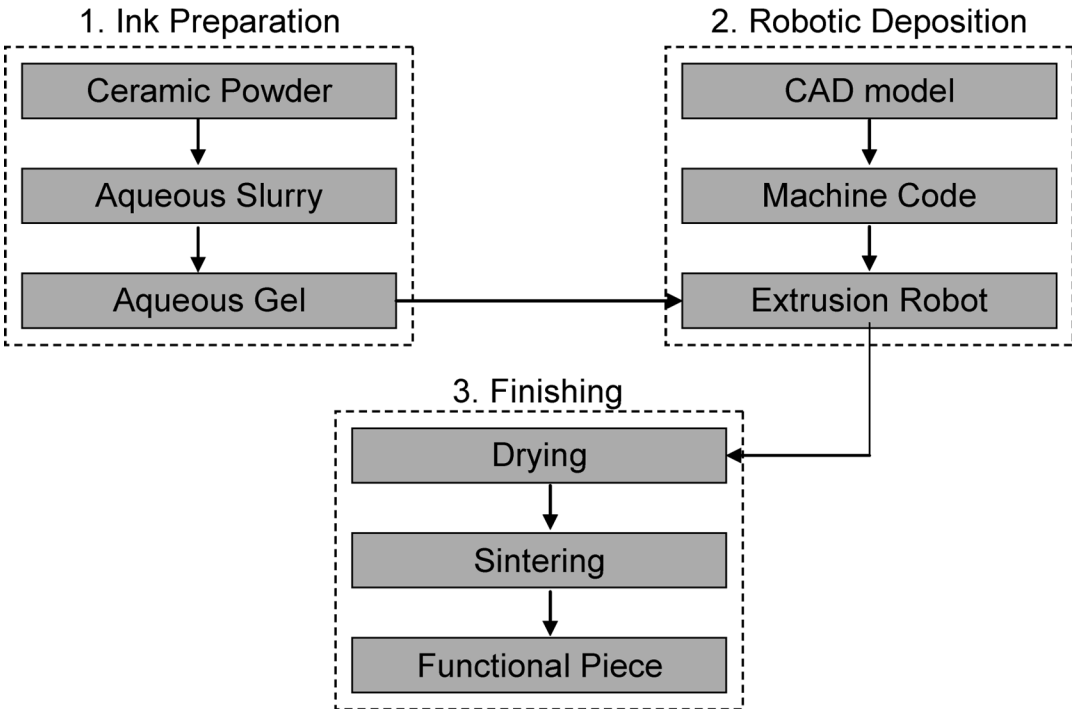


Figure 1.3 Relevant steps of the robocasting technique. Three main components are (1) Ink Preparation, (2) Robotic deposition, (3) Finishing operations

A generalized robocasting process flow chart is displayed in Figure 1.3. First, the ink is prepared by dispersing ceramic powder in water with the aid of polymeric dispersants. The desired ink rheology, shear thinning with yield stress, is obtained by

flocculating the particles by one or more mechanisms. Second, a CAD model is created and converted to machine code to command the robocasting tool, shown in Figure 1.4.

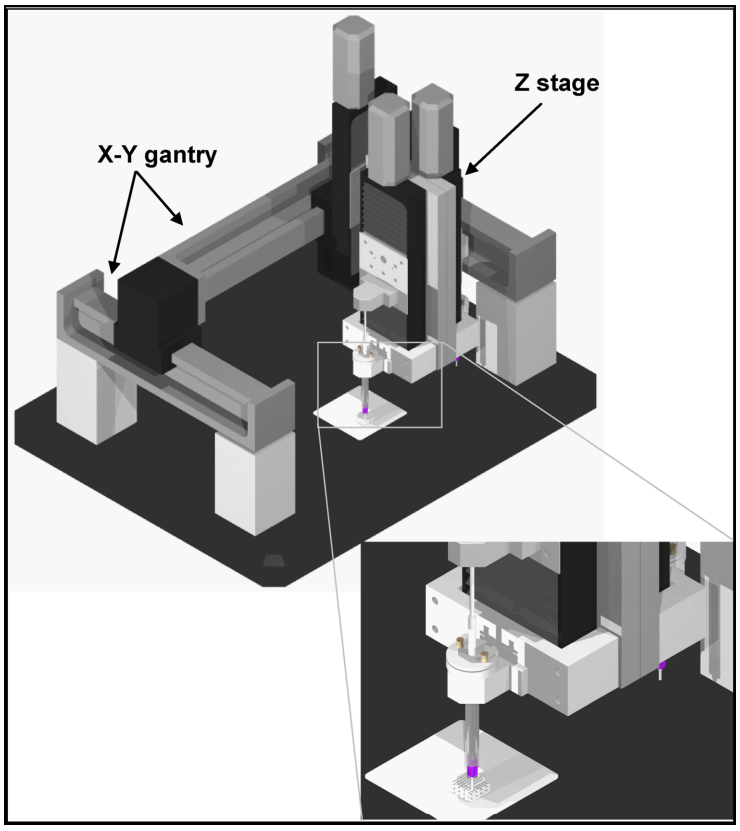


Figure 1.4 The extrusion based robotic deposition tool showing the x-y-z gantry system

The robocasting tool consists of a z-stage attached to an x-y gantry system. The syringe holding the material to be deposited (usually a ceramic, metal or polymer gel hitherto referred to as the ink) is affixed onto the z stage. A syringe pumps the ink through a fine diameter nozzle, onto a flat substrate or underlying layers. The x-y-z axes are able to determine the spatial positioning of the extrudate and thus simple and complex patterns may be printed. After printing, the third step is to dry the printed structure

followed by densification in a high temperature sintering operation. In some cases, finishing operations such as polishing or cutting may be required.

This thesis details the development of direct writing of colloidal gels to assemble photonic crystals from electro-optically tunable ferroelectric ceramics. The guiding hypothesis is:

***The robocasting process is a viable tool to assemble photonic crystal structures and can be used to test materials, methods and designs such as those required for fabrication of three dimensional tunable photonic crystals***

To test the hypothesis the following approach was adopted:

(1) A map for the colloidal processing of ternary ceramic feedstock materials composed of a mixture of barium titanate (BT), strontium titanate (ST) and barium zirconate (BZ) ceramics for use in the robocasting process was developed. A mixture of BT, ST, BZ was chosen due to high electro-optic tunability[11] and the ability to modify the zero field refractive index of the ternary composition. Experiments included ink development based on electro-steric colloidal stabilization using poly-electrolytes and various mechanisms for modulating their static and dynamic visco-elastic properties. The developed gels were suitable to fabricate photonic crystal lattice structures capable of displaying a complete 3-D photonic band gap. A schematic example of one such structure is shown in Figure 1.5. [12]

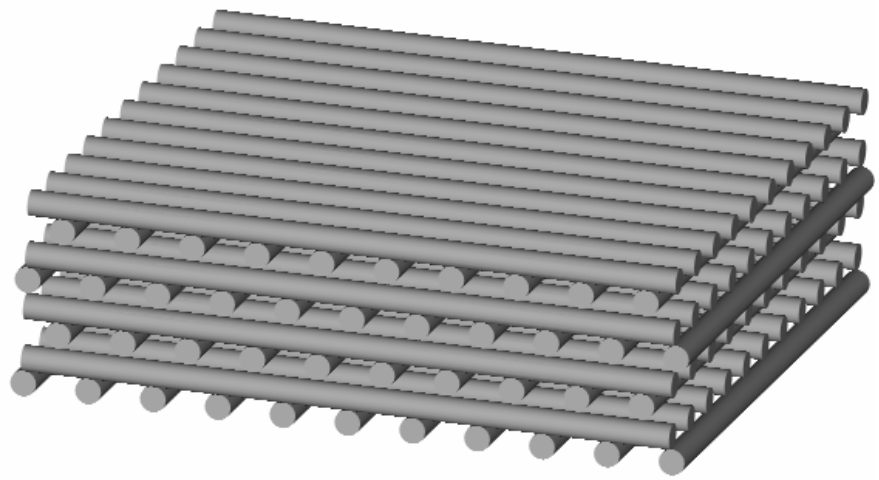

Figure 1.5 Woodpile style structure having a face-centered-tetragonal lattice symmetry which was previously shown to have a complete 3-D photonic band gap.

(2) Screening of the ternary mixtures of BT, ST, and BZ for electro-optic and dielectric properties suitable for photonic crystals was conducted. An impedance measurement technique was used to determine the low frequency (100 KHz) dielectric properties as a function of composition for these mixtures and tunability under the application of an external bias was investigated. Subsequently, high frequency measurements (100 GHz- 1 THz) were conducted to determine the refractive index and absorption of these materials for electro-magnetic wave transmission.

(3) Fabrication, modeling, and characterization of photonic crystals with 3-D tunable band gaps in the GHz-THz regime were done. Photonic crystal modeling was conducted based on results from Step 2 and appropriate geometries were determined for the photonic crystals. Fabrication was conducted using the colloidal processing map from Step 1 and appropriate composition determined from the modeling. Lattices thus

fabricated were tested for photonic band gaps using terahertz-time domain spectroscopy (THz-TDS).

### 1.3.Thesis scope

This thesis is subdivided into three main areas: (1) development of feedstock materials (inks) composed of mixtures of barium titanate, strontium titanate, and barium zirconate for the robocasting process, (2) fabrication and characterization of the electro-optic and dielectric properties of test samples composed of the mixtures, and (3) fabrication, modeling, and characterization of photonic crystals using the processing technique from area (1) and the low frequency properties from area (2). Each area is important for the ultimate goal of producing a tunable photonic crystal. Since both geometric structure and electro-optic properties are critical variables for successful photonic crystals, stringent demands are placed on the gels. The colloidal gels must not only be formulated of the correct material, but deposited lines must be strong enough to support their own weight and that of layers deposited over them. Electrically, the dielectric must have high tunability, low dielectric constant and low loss; properties which are difficult to achieve simultaneously.

### 1.4.Thesis organization

In Chapter 2, a brief literature survey reviews photonic crystals, the robocasting process, and the electro-optic effect in ferroelectric materials. Chapter 3 outlines the processing steps, detailed chemistry, and rheological characterization for colloidal gel inks. Chapter 4 is devoted to the characterization of electrical properties of the BT: ST:

BZ compositions involving measurements of dielectric constant, loss and tunability. Chapter 5 outlines the modeling, fabrication, and characterization of photonic crystals and evaluation of dielectric properties for E.M. wave propagation. Chapter 6 critically assesses the hypothesis and draws conclusions about the processing, fabrication, and characterization of the photonic crystals. Finally, recommendations for future development of tunable photonic crystals via both direct write and otherwise are made. Appendix A describes some preliminary results on an extension to robocasting of be able to print in-situ ternary ceramic mixtures.

# 2. REVIEW OF LITERATURE

## 2.1.Photonic crystals

### *2.1.1. Introduction*

The control of propagation of electromagnetic radiation by using reflectors, refractors, and wave guides is the subject of traditional optics. Many advances have been achieved with these elementary approaches such as fiber optics and advanced holography using laser light. However, using light for digital logic and memory elements has been limited due to miniaturization difficulties since the characteristic length scales for manipulating light waves is of the order of centimeters to millimeters for wave guides because of critical angles. Photonic band gap materials or photonic crystals offer a new approach to control light at the single wavelength scale.

Photonic crystals are spatial periodic arrangements of dielectric materials, in 1, 2, or 3 dimensions, which allow for control and manipulation of the propagation of electromagnetic (E.M.) waves. In semiconductors, electronic waves traveling through a periodic potential are arranged into energy bands separated by band gaps. These bands emerge due to the "forbidden" energy states from quantization of electrons as the isolated atoms assemble in crystals. For photonic crystals, the periodic arrangement of dielectric materials causes forbidden modes for E.M. waves (i.e., forbidden frequencies) to exist within the crystal, known as photonic band gaps. The forbidden modes are directional

and depend on the arrangement of the dielectrics, the size scale of periodicity, and the dielectric constant. This imposed restriction on allowable modes results in:[1]

a) Prohibition of propagation of E.M. waves
b) Propagation within only certain frequency regions
c) Localization of E.M. waves to specific areas

Photonic band gaps may be introduced within a structure having a macroscopic arrangement of dielectric materials on a periodicity similar to the wavelength of the EM radiation where the band gap is to be achieved. Photonic wavelengths span several orders of magnitude from nanometers (visible light) to centimeters (radio waves). Therefore size scales for photonic crystals also range from nanometers to centimeters. Photonic crystals may be designed and fabricated using established and evolving nano and micro-fabrication techniques. Potential applications for photonic crystals include:

1. Incorporation into fiber-optic systems for reducing energy losses
2. Increasing transmission speeds in communications as compared to using electronics
3. Decreasing energy losses in optical devices such as lasers, spectrometers, radars, and satellite communications by localization of radiations
4. Opto-electronic equivalents of electronic devices such as filters, transistors and waveguides towards the development of photonic computers

Since periodicity and dielectric response of the material are responsible for establishing the allowable E.M. modes, photonic crystals are appropriately labeled as 1-D, 2-D and 3-D depending on the number of directions in which periodicity occurs.[1] Additionally, when the allowable modes of transmission may be modulated by an

external stimulus, photonic crystals are labeled as tunable photonic crystals. This stimulus may be in the form of an applied external field, change in the periodicity or material properties.[13] In this thesis a novel direct write technique known as robocasting has been used to fabricate 3-D photonic crystals using electro-optically tunable materials.

The literature review of this chapter is divided into three areas. First, descriptions of the theoretical methods for modeling of photonic crystals are provided. Three chief modeling techniques are discussed, namely (i) the plane wave expansion method, (ii) the transfer matrix method, and (iii) the finite difference time domain (FDTD) method. Included are some descriptions about the chief fabrication techniques for both non-tunable and tunable photonic crystals. Next, a brief review of the direct write technique robocasting is provided. The review is concluded by a description of polarization processes in dielectrics and electro-optic properties of barium strontium titanate mixtures.

### *2.1.2. Modeling of Photonic Crystals*

#### 2.1.2.1. Plane wave method

This description is based largely on the technique described in the reference by Joannopoulos.[1] To study the behavior of E.M. waves in photonic band gap materials, Maxwell's equations are applied for media characterized by a spatially varying dielectric function ε(r). The four Maxwell's equations are:

$$\nabla \cdot \mathbf{B} = 0 \tag{2.1}$$

$$\nabla \times \mathbf{E} + \frac{1}{c}\frac{\partial \mathbf{B}}{\partial t} = 0 \tag{2.2}$$

$$\nabla \cdot \mathbf{D} = 4\pi\rho \tag{2.3}$$

$$\nabla \times \mathbf{H} - \frac{1}{c}\frac{\partial \mathbf{D}}{\partial t} = \frac{4\pi}{c}\mathbf{J} \tag{2.4}$$

where : **E** is the electric field vector, **H** is the magnetic field vector, **D** is the dielectric displacement vector, **B** is the magnetic induction vector, ρ is the density of free charges, **J** is the current density vector, *t* is time, and *c* is the speed of light.

The following simplifying assumptions aid in numerical solution for periodic dielectric medium:

a) The various dielectric regions are homogeneous within that region

b) No free charges or currents exist within the material (i.e., ρ= 0, **J**=0)

c) Field strengths are small and within the linear dielectric region

d) The material is macroscopic and isotropic so that **E**(**r**, ω), **D**(**r**, ω) can be related by

$$\mathbf{D}(\mathbf{r},\omega) = \varepsilon(\mathbf{r}) \cdot \mathbf{E}(\mathbf{r},\omega) \tag{2.5}$$

e) Dielectric is lossless and independent of frequency

f) Magnetic permeability is ~1 so **B**=**H**

With these assumptions the Maxwell's equations are:

$$\nabla \cdot \mathbf{H}(\mathbf{r},t) = 0 \tag{2.6}$$

$$\nabla \times \mathbf{E}(\mathbf{r},t) + \frac{1}{c}\frac{\partial \mathbf{H}(\mathbf{r},t)}{\partial t} = 0 \tag{2.7}$$

$$\nabla \cdot \varepsilon(\mathbf{r})\mathbf{E}(\mathbf{r},t) = 0 \tag{2.8}$$

$$\nabla \times \mathbf{H}(\mathbf{r},t) - \frac{1}{c}\varepsilon(\mathbf{r})\frac{\partial \mathbf{E}(\mathbf{r},t)}{\partial t} = 0 \tag{2.9}$$

While **E** and **H** are complicated functions in time and space, they may be simplified since the Maxwell's equations are linear in nature. The time dependence may

be separated out by expanding the fields into a set of Harmonic modes. The Maxwell equations impose a set of restrictions on field pattern that happen to vary sinusoidally with time and these must be satisfied.

Converting the Electric and Magnetic field into harmonic modes one obtains

$$\mathbf{H}(\mathbf{r},t) = \mathbf{H}(\mathbf{r})\, e^{i\omega t} \tag{2.10}$$

$$\mathbf{E}(\mathbf{r},t) = \mathbf{E}(\mathbf{r})\, e^{i\omega t} \tag{2.11}$$

Substituting equations (2.10) and (2.11) in (2.6)-(2.9), one obtains the following set of relations for the divergence terms

$$\nabla \cdot \mathbf{H(r)} = 0 \tag{2.12}$$

$$\nabla \cdot \mathbf{E(r)} = 0 \tag{2.13}$$

and for the curl terms

$$\nabla \times \mathbf{E(r)} + \frac{i\omega}{c}\mathbf{H}(\mathbf{r}) = 0 \tag{2.14}$$

$$\nabla \times \mathbf{H(r)} - \frac{i\omega}{c}\varepsilon(\mathbf{r})\mathbf{E(r)} = 0 \tag{2.15}$$

To decouple the equations, one curls equation (2.15) divided by ε(r) and uses equation 2.14 to eliminate **E(r)**. The final result is a Master Equation entirely in **H**(r)

$$\nabla \times \left( \frac{1}{\varepsilon(\mathbf{r})} \nabla \times \mathbf{H(r)} \right) = (\frac{\omega}{c})^2 \mathbf{H(r)} \tag{2.16}$$

Allowable modes for **H**(**r**) may be solved for in the following sequence:

1. Solve equation (2.16) to find the modes **H**(**r**) for given frequency, subject to the requirement that equations (2.12) and (2.13) are satisfied

2. Use equation (2.15) to recover **E**(**r**)

For a periodically varying system such as a lattice one can use Bloch's theorem to expand the electric and magnetic fields in terms of Bloch waves[1]:

$$\mathbf{H}(\mathbf{r}) = \sum_{\mathbf{K}} \mathbf{H}_{\mathbf{k}} \exp(i\mathbf{K} \cdot \mathbf{r}) \tag{2.17}$$

Where $\mathbf{K} = \mathbf{k} + \mathbf{G}$. $\mathbf{k}$ is a wave vector. A wave vector has magnitude $|\mathbf{k}| = \frac{2\pi}{\lambda}$ and points in the direction of wave propagation. $\mathbf{G}$ is a reciprocal lattice vector

A reciprocal lattice is a lattice in Fourier space defined for an actual crystal lattice. Since the crystal lattice is periodic in nature, translation of a function within a crystal lattice should yield the same function if translation distance is an integer multiple of the lattice constant. Hence, instead of solving (2.16) for all of real lattice space defined by the crystal one needs to only work with points in the reciprocal lattice defined by $\mathbf{G} \cdot \mathbf{R} = n2\pi$ where $\mathbf{G}$ is a reciprocal lattice vector and $\mathbf{R}$ is a real lattice vector.

Wave vectors are conveniently incorporated into the reciprocal lattice and it must be understood that incrementing a wave vector $\mathbf{k}$ by $\mathbf{G}$, a reciprocal lattice vector will result in the same vector $\mathbf{k}$, hence one needs to consider only wave vectors in the region of the reciprocal lattice where one may not obtain the original wave vector by simply incrementing with $\mathbf{G}$. This region is defined as the Brillouin zone and is the region which is closer to a lattice point, e.g. origin, than any other in the reciprocal space. A visual description of the Brillouin zone concept is shown in Figure 2.1.[1] A square lattice with spacing $a$ yields a reciprocal lattice with a spacing $2\pi/a$ and has a Brillouin Zone marked gray in the Figure. Further details of the Brillouin zone and its properties can be found in the book by Joannopoulous.[1]

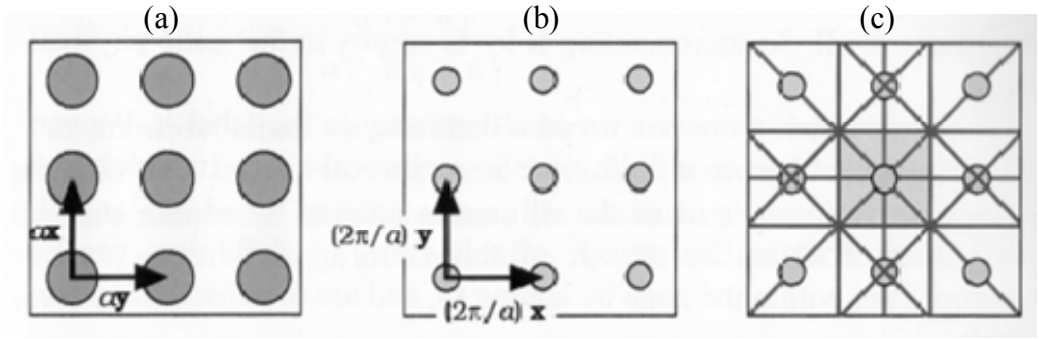


Figure 2.1 The corresponding reciprocal lattice and Brillouin zone for a square lattice.[1]

The solution for magnetic field in equation (2.17) has the form of an eigenvalue problem

$$\sum_{\mathbf{K}} \mathbf{K} \times \varepsilon_{\mathbf{K}\cdot\mathbf{K}'}^{-1} (\mathbf{K} \times \mathbf{H}_{\mathbf{K}'}) = -(\omega/c)^2 \mathbf{H}_{\mathbf{K}} \tag{2.18}$$

Where $\varepsilon_{\mathbf{K}\cdot\mathbf{K}'} = \varepsilon(\mathbf{G} - \mathbf{G}')$ is a Fourier transform of the dielectric function. Equation (2.18) may be solved using matrix methods over several high symmetry points in the Brillouin zone or on a grid in the Brillouin zone to determine photonic density of states. A typical dispersion diagram for silica spheres in a compact face centered cubic arrangement is shown in Figure 2.2.[14] A fundamental difference between electronic energy bands and photonic energy bands is that there is no fundamental length scale for photonic bands and they may be scaled by varying lattice parameters. What this implies is that the bands depend on the length scale of periodicity (i.e. lattice constant) of the structure and computing a band diagram of wave vectors versus energy for a particular geometry serves to establish allowable modes for all feature sizes. In the Figure, the wave number and direction of propagation for wave vectors is plotted on the X axis and energy on the Y axis in convenient units of $a/\lambda$ where $a$ is the lattice parameter (Note: $E=hc/\lambda$).

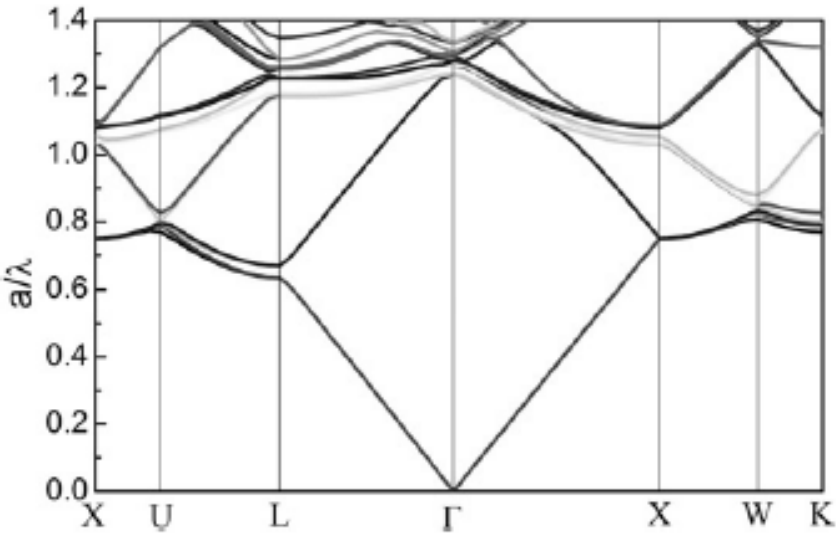


Figure 2.2 A dispersion band diagram showing the associated energies for various wave vectors in the irreducible Brillouin zone for silica spheres in FCC arrangements

The different vertical panels represent the wave vectors joining the origin to midpoints of its nearest neighbors in the reciprocal lattice (i.e., the irreducible Brillouin zone) within the Brillouin zone. Therefore the panel ΓX represents dispersion relations for states with increasing **k**, all pointing in the same direction within the reciprocal lattice (X= [001]) whereas in panels such as XW both modulus and direction vary to sweep from the center X to the corner W of the square faces of the Face center cubic (FCC) Brillouin zone. Among the bands plotted within each panel, some have the familiar form $\omega = (c/n)k$ where n is effective refractive index or in some cases $\omega=(c/n)(k-2\pi/a)$ which results from shifting the vector **k** by one reciprocal lattice vector parallel to the vector involved. In some cases the folding back of vectors not parallel to high symmetry points can cause relations such as $\omega=(c/n)k'=(c/n)[(2\pi/a)^2+k^2]^{1/2}$. Multiple such complicated bands exist for three dimensional structures. Within each panel all energies do not have

an associated **k**. These frequencies within each panel are called gaps and when these gaps extend over all panels (i.e., wave vectors) one obtains a photonic band gap. This is a range of frequencies for which no wave vectors are allowed to exist within the structure as shown in Figure 2.3. Further details can be found on an excellent article on photonic crystals by Lopez.[14]

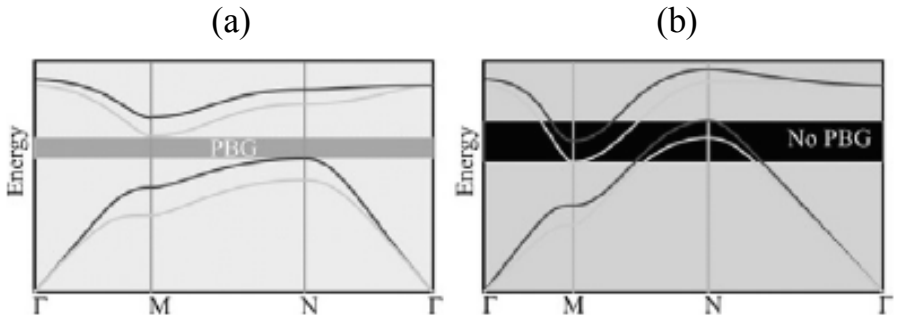


Figure 2.3 Photonic band gaps emerge when wave vectors have no corresponding energies or bands across all wave vectors in the Brillouin zone

2.1.2.1.1. Scaling properties of the Maxwell's equations

The plane wave approach is instructive for understanding scaling of the photonic crystals with regard to the dielectric and lattice constant due to the scaling of the Maxwell's equations.[1] An assumption made here is that an electromagnetic eigenmode **H(r)** of frequency ω exists that satisfies the Master equation (2.16). If the lattice constant is changed so that the periodicity in the dielectric constant is scaled by factor s such that the new dielectric function becomes $\varepsilon'(\mathbf{r})= \varepsilon(\mathbf{r}/s)$ for some scale parameter s then substituting variables in (2.16) using $\mathbf{r'}=s\mathbf{r}$ and $\nabla' = \nabla / s$ yields:

$$s\nabla'\times(\frac{1}{\varepsilon'(\mathbf{r'}/s)} s\nabla'\times\mathbf{H}(\mathbf{r'}/s) = (\frac{\omega}{c})^2 \mathbf{H}(\mathbf{r'}/s) \qquad (2.19)$$

However ε(**r'**/s)= **ε'**(**r'**). Dividing out the s's shows that

$$\nabla'\times(\frac{1}{\varepsilon'(\mathbf{r'})}\nabla'\times H(\mathbf{r'}/s) = (\frac{\omega}{cs})^2\,\mathbf{H}(\mathbf{r'}/s) \tag{2.20}$$

Which is the Master equation again, with a mode profile H'(r') = H(r'/s) and frequency ω'=ω/s. Therefore the new mode profile after changing the length scale by a factor s is the old mode profile and its frequency scaled by a factor s. Similarly substituting the dielectric constant in equation (2.16) by a new one ε'(r) = ε(r)/$s^2$ yields

$$\nabla\times(\frac{1}{\varepsilon'(\mathbf{r})}\nabla\times\mathbf{H}(\mathbf{r}) = (\frac{s\omega}{c})^2\,\mathbf{H}(\mathbf{r}) \tag{2.21}$$

The harmonic modes of the new system are unchanged however frequencies are scaled by a factor s and therefore scaling the dielectric constant by a fourth will tend to double the frequencies of the modes.

There are two major drawbacks to using the plane wave method in the case of photonic crystals:[1] (i) it assumes the dielectric constant ε(**r**) to be real i.e., loss =0. This assumption is not valid in the case of barium titanate type ceramics since these typically have significant loss and (ii) it assumes no frequency dependence of the dielectric constant. Hence, while the plane wave method is instructive for understanding the phenomenology of photonic band gaps, it is unsuitable for modeling photonic crystals such as the ones investigated in this thesis and an alternative method called the transfer matrix method (TMM) is used.

#### 2.1.2.2. Transfer matrix method

While the plane wave expansion method uses wave vectors and calculates the corresponding energies associated with them, the Transfer Matrix Method (TMM) uses

the reverse approach. It uses the energies (frequencies) and calculates the allowable wave vectors using a finite element modeling approach. Primary advantages of the TMM method are that it assumes a complex dielectric constant and allows for a frequency dependent dielectric function. This method has been applied to compute the band structure for 2-D photonic crystals,[15, 16] photonic with complex frequency dependent dielectric functions[17] and metallic photonic crystals[18, 19] with excellent match between measurement and simulation. For an in-depth derivation of the TMM method the reader is referred to references by Pendry *et al.* [20, 21] The governing equations are summarized here.[22] The transfer matrix method uses discretized forms of equations (2.2) and (2.4) and eliminates the z components of the field to develop the following equations:

$$\begin{aligned}\mathbf{E}_{\mathbf{x}}(i,j,k+1) = \mathbf{E}_{\mathbf{x}}(i,j,k) + ic\omega\mu_0\mu(i,j,k)\mathbf{H}_{\mathbf{y}}(i,j,k) + \frac{ic}{a\omega\varepsilon_0\varepsilon(i,j,k)} \times [a^{-1}\{\mathbf{H}_{\mathbf{y}}(i-1,j,k) \\ - \mathbf{H}_{\mathbf{y}}(i,j,k) - b^{-1}\{\mathbf{H}_{\mathbf{x}}(i,j-1,k) - H_x(i,j,k)\}] - \frac{ic}{a\omega\varepsilon_0\varepsilon(i+1,j,k)} \\ \times [a^{-1\epsilon}\{\mathbf{H}_{\mathbf{y}}(i,j,k) - \mathbf{H}_{\mathbf{y}}(i+1,j,k)\} - b^{-1}\{H_x(i+1,j-1,k) - \mathbf{H}_{\mathbf{x}}(i+1,j,k)\}]\end{aligned} \tag{2.22}$$

$$\begin{aligned}\mathbf{E}_{\mathbf{y}}(i,j,k+1) = \mathbf{E}_{\mathbf{y}}(i,j,k) + ic\omega\mu_0\mu(i,j,k)\mathbf{H}_{\mathbf{x}}(i,j,k) + \frac{ic}{b\omega\varepsilon_0\varepsilon(i,j,k)} \\ \times [a^{-1}\{\mathbf{H}_{\mathbf{y}}(i-1,j,k) - \mathbf{H}_{\mathbf{y}}(i,j,k) - b^{-1}\{\mathbf{H}_{\mathbf{x}}(i,j-1,k) - \mathbf{H}_{\mathbf{x}}(i,j,k)\}] \\ - \frac{ic}{b\omega\varepsilon_0\varepsilon(i,j+1,k)} \times [a^{-1}\{\mathbf{H}_{\mathbf{y}}(i-1,j+1,k) - \mathbf{H}_{\mathbf{y}}(i,j+1,k)\} \\ - b^{-1}\{\mathbf{H}_{\mathbf{x}}(i,j,k) - \mathbf{H}_{\mathbf{x}}(i,j+1,k)\}]\end{aligned} \tag{2.23}$$

$$\begin{aligned}\mathbf{H}_{\mathbf{x}}(i,j,k+1) = \mathbf{H}_{\mathbf{x}}(i,j,k) + ic\omega\varepsilon_0\varepsilon(i,j,k+1)\mathbf{E}_{\mathbf{y}}(i,j,k+1) + \frac{ic}{a\omega\mu_0\mu(i-1,j,k+1)} \\ \times [a^{-1}\{\mathbf{E}_{\mathbf{y}}(i,j,k+1) - \mathbf{E}_{\mathbf{y}}(i-1,j,k+1) - b^{-1}\{\mathbf{E}_{\mathbf{x}}(i-1,j+1,k+1) - \mathbf{E}_{\mathbf{x}}(i-1,j,k+1)\}] \\ - \frac{ic}{a\omega\mu_0\mu(i,j,k+1)} \times [a^{-1}\{\mathbf{E}_{\mathbf{y}}(i+1,j,k+1) - \mathbf{E}_{\mathbf{y}}(i,j,k+1)\} - b^{-1}\{\mathbf{E}_{\mathbf{x}}(i,j+1,k+1) - \mathbf{E}_{\mathbf{x}}(i,j,k+1)\}]\end{aligned} \tag{2.24}$$

$$\mathbf{H}_y(i,j,k+1) = \mathbf{H}_y(i,j,k) + ic\omega\varepsilon_0\varepsilon(i,j,k+1)\mathbf{E}_x(i,j,k+1) + \frac{ic}{a\omega\mu_0\mu(i,j-1,k+1)}$$
$$\times[a^{-1}\{\mathbf{E}_y(i+1,j-1,k+1) - \mathbf{E}_y(i,j-1,k+1) - b^{-1}\{\mathbf{E}_x(i,j,k+1)$$
$$- \mathbf{E}_x(i,j-1,k+1)\}] - \frac{ic}{a\omega\mu_0\mu(i,j,k+1)} \times [a^{-1}\{\mathbf{E}_y(i+1,j,k+1)$$
$$- \mathbf{E}_y(i,j,k+1)\} - b^{-1}\{\mathbf{E}_x(i,j+1,k+1) - \mathbf{E}_x(i,j,k+1)\}] \quad (2.25)$$

Where ε(i,j,k) and μ(i,j,k) are the dielectric constant and magnetic permeability at the subcell (i,j,k). Dimensions of subcells along x,y,z directions are a,b,c respectively. Equations (2.22)-(2.25) connect the fields at the k+1 plane with the fields at k plane., where k is a discretized step in the z direction. Hence the magnitudes of the electric and the magnetic field may be solved stepwise moving from one side of the photonic crystal to the other, making computations across each 2-D layer as a set of transfer matrices.

2.1.2.3. Finite difference time domain method

The finite difference time domain method[22-24] is used to model photonic crystals having both steady state and transient behavior. This method utilizes a finite difference approach to numerically solve equations (2.2) and (2.4). These equations are approximated with finite differences and the electric and magnetic field assumed to lie on the sides and face centered points of a Yee cell[25] at times nΔt and (n+1/2)Δt respectively. This results in both a spatial and temporal offset of the two fields when the Maxwell's equations are solved on each face of the cube. The system is described by a spatial grid and solved for time steps less than that required for the E.M. wave to propagate one grid spacing during the time step.

### *2.1.3. Fabrication techniques*

The complexity of fabrication of PBG structures scales with desired frequency of the band gap and level of dimensionality (i.e., 1-D, 2-D or 3-D). Photonic crystals operating at microwave frequencies have resolution on the mm scale and may be fabricated using simple micromachining techniques whereas optical band gaps require control on the micron scale and are considerably more difficult to fabricate. 1-D and 2-D photonic crystals are relatively straightforward to fabricate and involve the stacking of alternate layers of materials with different dielectric constants[26] or selective lithographic etching of underlying silicon substrates using masks to produce 2-D structures respectively[27] . 3-D crystal fabrication, however, has faced the greatest challenges. There is a requirement for large refractive index contrasts between materials constituting the photonic crystal. This implies structures that usually consist of air and a ceramic/metallic/semiconductor material. Also, low filling fractions implies the structures are mostly air making μm scale fabrication of 3-D crystals difficult. The following technologies represent the state of the art in fabrication of 3-D PBG crystals such as the ones realized in this thesis. These are divided into top down fabrication techniques usually involving directed placement, removal or creation of material and self assembly techniques involving self assembly of colloidal entities.

#### 2.1.3.1. Top down fabrication

The first PBG crystal with a gap at mm wavelengths was built by Yablonovitch[28] by drilling tri-angular cylindrical holes in a dielectric block. This fabrication process, however, has found limited popularity because it is difficult to drill uniform holes of

appreciable depth with micron size diameters. Succeeding this effort HO *et al.*[12] demonstrated a full 3-D PBG for a new structure based on stacking of one dimensional alumina rods with a stacking sequence that repeats every 4 layers in a lattice type assembly. This fabrication was macroscopic and involved rods of ~3 mm in diameter stuck with an index matched glue. They achieved a full 3-D PBG at 12-14 GHz. Next, deep x-ray lithography was used by Feiertag and co-workers[29] to generate cylindrical holes in a PMMA structure which were then re-infiltrated with ceramic materials to yield a photonic crystal operating at ~ 2.5 GHz frequency. Lin *et al.* (using $Si/SiO_2$)[3] demonstrated a new method of photonic crystal fabrication where they deposited, patterned and etched fugitive material layers and then deposited silicon, a high refractive index material, finally etching away the fugitive materials to obtain a woodpile structure of rods showing a band gap at 30 THz. Noda *et al.*(using III-V semiconductor material)[30] also fabricated an infrared operating photonic crystal using GaAs using a combination of e-beam lithography coupled with ion beam etching. Holographic lithography[31] is a new technique for crystal fabrication that involves the creation of a template from photo-resist using 4-beam laser interference pattern which then serves as a template for re-infiltration with a higher refractive index contrast material to form a photonic crystal.

2.1.3.2. Colloidal self assembly

Self assembly techniques for fabrication of 3-D photonic crystals provide resolution on the nano or micro scale but lack precision for placement of defects in photonic crystals which could introduce special transmission states. It is also difficult to obtain high porosities required for obtaining a complete photonic band gap or have a high

refractive index contrast[32]. In a typical scheme a large multitude of silica or latex spheres (usually micron diameter in size) are allowed to self organize into a crystalline lattice. Next, the void spaces between spheres are infiltrated with a semiconductor material and the original spheres are etched away leaving behind an arrangement of micron sized spherical voids in a high refractive index material. In fact the infiltration of high refractive index materials into the interstices of the spheres is a limiting factor in this process.[32] This fabrication method called synthetic opal templating has been coupled with various self assembly techniques to yield 3-D crystals:

- **a.** Nanocrystal sintering:[33] re-infiltration by nano-sized particles dissolved in a solvent which is then subsequently evaporated to leave behind an inverse structure after etching
- **b.** Electrodeposition:[34] material is deposited due to a electronic reaction in an electro chemical cell
- **c.** Chemical vapor deposition:[35] deposition of silicon from a precursor disilane gas.
- **d.** Oxide reduction:[36] deposition of Ge from its oxide state by reduction

### *2.1.4. Tunable photonic crystals*

Current endeavors in PBG crystal development are aimed towards fabrication of a tunable photonic band gap (where the PBG may be tuned or modulated by an appropriate change in crystal properties) imparting selectivity to the frequency of radiations being allowed to propagate. Several strategies for imparting tunability to the photonic crystals are being investigated by PBG researchers and each depends on the material of choice for

fabrication. Busch *et al.*[37] used a birefringent nematic liquid crystal infiltrated into the void region of an inverse opal made of silicon. The photonic band gap was then selectively opened or closed using an externally applied electric field which rotated the axis of the nematic molecules relative to the inverse opal backbone. This technique, however, was only capable of absolute selectivity whereby either the radiation was allowed to propagate or prohibited completely. Kim and others[38] fabricated a strain tunable 2-D photonic band gap by toggling the symmetry of a piezoelectric lattice between a regular hexagonal and quasi-hexagonal using an external field. A 2% to 3% strain was used to obtain 73% tunability compared to the original undistorted structures. Li *et al.* [39] also demonstrated the electric field tunability of the PBG exhibited by an inverse opal structure consisting of (Pb, La)(Zr) $TiO_3$ (PLZT). The photonic band gap of the PLZT structure shifted continuously with change in the applied electric field. The band gap was exhibited between 500-700nm of EM radiation. All these works involved tunability using an external electric field. However, it is notable to mention other works in this area namely Saado *et al.*[40] fabricated a 3-D photonic crystal consisting of metal coated disk-shaped magnetic particles floating at the liquid air interface inside a stack of containers. An external magnetic field was modulated to impart tunability. Finally Kubo[41] has demonstrated a tunable photonic crystal using nematic liquid crystals and $SiO_2$ inverse films whereby tunability was controlled by changing the refractive indices of the liquid crystal using photo-induced isothermal phase transition of the liquid crystal.

While the strategies mentioned above for tunability of the PBG have met with some success, they are either impractical to implement in mass production or are inherently slow in the switching capability. An external field tunable PBG is ideal given

the ease of incorporation of such a device into existing computers and electro-optic devices, which utilize electronic components and have readily available resources for utilization by such components. Hence, a field tunable material must be fabricated in the correct geometry for a PBG, implying that the investigator delve into both materials and device fabrication research. Few investigators have taken advantage of direct write techniques to design PBG crystals despite the obvious ease with which geometries may be created. This is largely due to the fact that either the materials palette available for device fabrication and/or the resolution with which devices may be printed have been limiting factors.

Smay *et al.*[8] have successfully demonstrated the potential for the robocasting process to fabricate a photonic crystal displaying a passive band gap in the 80-100 GHz regime using alumina rods stacked at right angles to rods in adjacent layers. This so called woodpile structure may be designed to contain line and point defects by omission of rods in certain layers. Working in this direction it is desirable to prove that this direct write scheme is suitable to fabricate tunable photonic crystals with engineered defects and controlled spatial arrangement of materials.

## 2.2.Direct write using robocasting

### *2.2.1. Direct Writing of Colloidal Inks*

Rapid prototyping has become a staple of most design engineers. However, the current set of rapid prototyping tools are best suited for metals (e.g., CNC machining, laser engineered net shaping) or polymers (e.g., stereolithography, 3-D Printing, fused deposition modeling, and selective laser sintering). More recently, extrusion based

deposition processes have demonstrated an ability to assemble three-dimensional ceramic forms without the need for part-specific tooling or molds. Such Solid Freeform Fabrication (SFF) methods provide a route to manufacture structures that are difficult or impossible to build by other processes. This is especially true when one considers the potential of extrusion based SFF methods to spatially grade composition. Current SFF methods in wide use are stereolithography,[42] selective laser sintering, [43-45] 3-D printing, [46] reactive extrusion free-forming, [42] fused deposition modeling,[47-52] and ink jet printing.[53, 54]

The robocasting process works on the same basic premise as fused deposition: create tool path instructions via a CAD program and then trace the tool path with a pen tip while extruding the "ink". However, robocasting requires only low binder concentration and inks of various composition may be easily formulated.[9, 10, 55-59] The robocasting equipment may be imagined as a CNC milling machine where the cutter has been replaced by a deposition nozzle as illustrated in Figure 2.4.

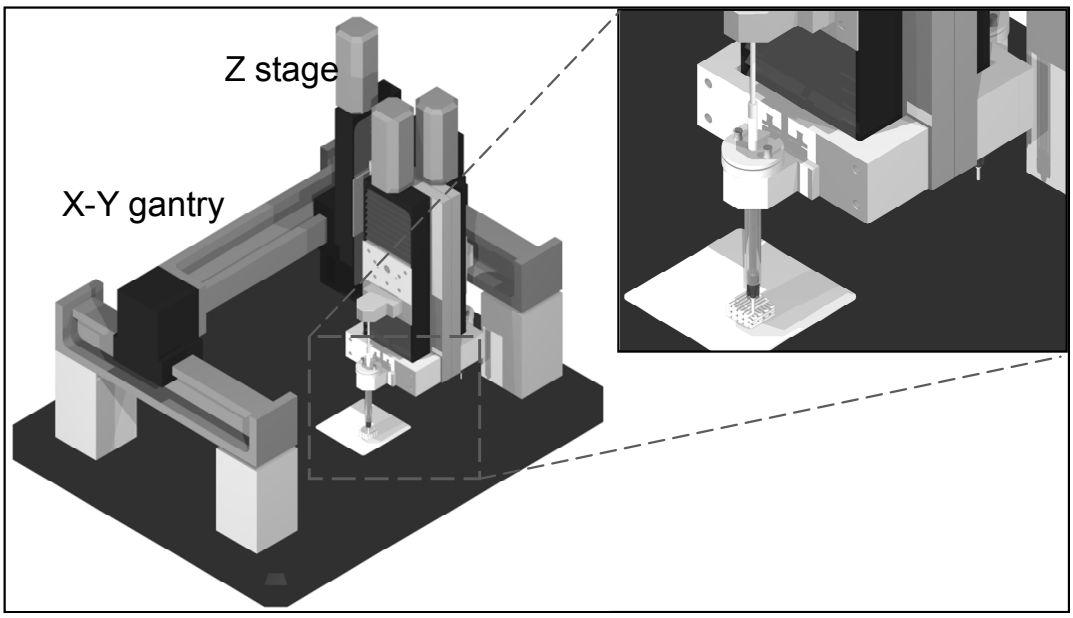


Figure 2.4 Schematic of the robocasting deposition device showing the x-y-z gantry system used to control the spatial position of deposition nozzle (inset).

In this configuration *x-y* planar motion is actuated by the gantry system and vertical position of the deposition nozzle by the *z* stage. Ink flow rate is controlled by use of linear actuators that act as syringe pumps affixed to the *z* stage. The robocasting process can be represented as a three step process as illustrated in Figure 2.5. First, the ink is prepared by dispersing ceramic powder in water with the aid of polymeric dispersants. The desired ink rheology, shear thinning with yield stress, is obtained by flocculating the particles by one or more mechanisms. Second, a CAD model is created and converted to machine code to command the robocasting tool. The ink is loaded into the syringes and printed in the desired pattern, as shown in inset in Figure 2.4. The third step is to dry the printed structure followed by densification in a high temperature

sintering operation. In some cases, finishing operations such as polishing or cutting may be required.

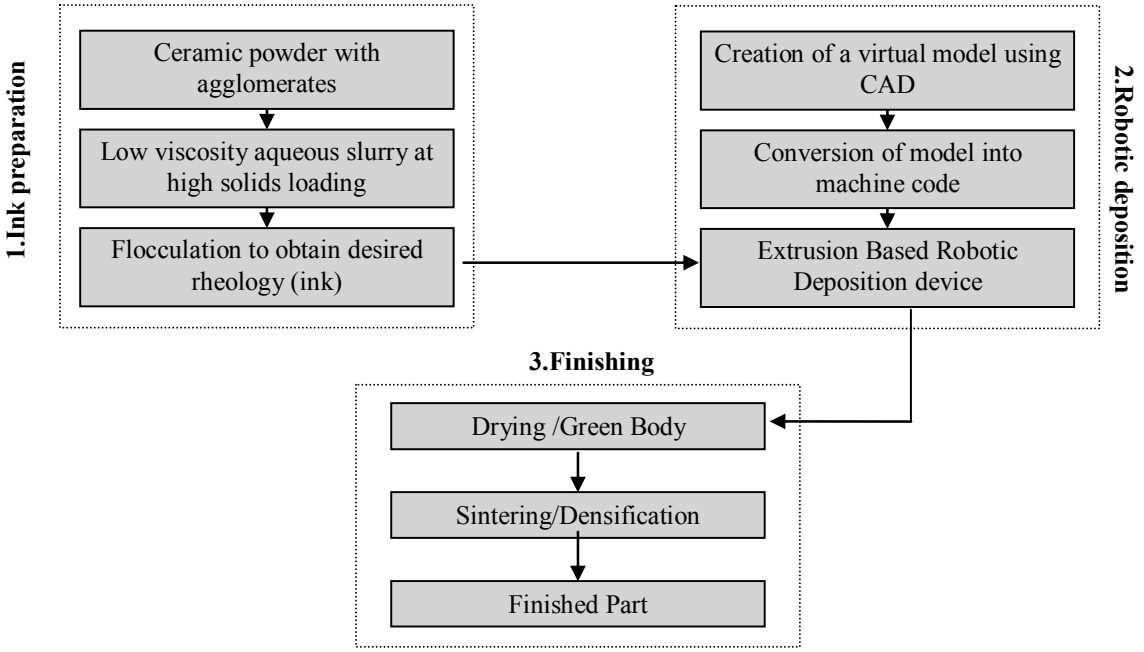


Figure 2.5 A schematic showing the three components of the robocasting process (a) ink development, (b) deposition, (c) finishing operations

Inks used in the robocasting process must satisfy several criteria for successful assembly of complex structures. The inks must be:

a) Homogeneously mixed - The presence of agglomerates may lead to clogging of small diameter nozzles and anisotropy in the green microstructure.

b) Extrudable through 100-500 μm diameter nozzles without filter pressing under application of moderate pressure.

c) Set rapidly after deposition to retain the desired shape under the stress of its own weight, new lines printed on top, and drying of the green structure

The ink behavior is engineered by carefully controlling inter-particle interactions to first generate a highly concentrated, stable dispersion at low viscosity followed by inducing a system change that promotes a fluid-to-gel transition.[9] Gelation imparts rheological properties to the ink such as shear-thinning, yield stress and elasticity, which are crucial to the printing process. Colloidal gels consist of a percolating network of attractive particles capable of transmitting stress above a critical volume fraction ($\phi_{gel}$). In the robocasting process, the colloid volume fraction constant is maintained while controlling elastic properties of the ink through the strength of inter particle attractions according to the relationship given by:[60]

$$y=k\,(\phi/\phi_{gel} - 1)^{x} \qquad (2.26)$$

where y is the property of interest (shear yield stress($\tau_y$) or elastic modulus(G'), k is a system specific constant and x is the scaling exponent(~2.5). The equilibrium mechanical properties of colloidal gels are governed by two parameters: $\phi$, which is proportional to the bond density and $\phi_{gel}$, which scales inversely with the bond strength. In this approach $\phi$ is maintained to be constant, while decreasing $\phi_{gel}$ by altering the inter-particle strength of attraction.

Previously, ceramic robocasting has been used to fabricate three dimensional structures for electro-ceramics,[6, 8, 9, 57, 59, 61-65] structural ceramics,[10, 56, 66-72] biomedical ceramics[73-75] and some other novel applications including diesel particulate filters[76] and catalytic support structures.[55, 77] Feature size has ranged from 60 μm to well into mm

dimensions. Mechanisms for improving the structural strength of the slurry have ranged from drying or salt flocculation to more recently the use of an oppositely charged polyelectrolyte to cause a fluid-to-gel transition.[65]

### *2.2.2. Robocasting of photonic crystals*

Since photonic crystals are periodic in nature, direct write provides a viable alternative to manufacture these for testing materials and designs. Both robocasting and closely related fused deposition modeling have been used previously to make layer-by-layer photonic crystals. In the case of robocasting, Smay *et al.*[8] have demonstrated the fabrication of a layer by layer photonic crystal having face centered tetragonal stacking pattern. Strategically placed line defects, introduced by removal of some rods from the stacking pattern, allowed for some transmission modes to emerge. This structure was made of rods 640 μm (henceforth rod diameter will be referred to as feature size) and a pitch of 2.25 mm. A band gap was observed between 80-100 GHz. Recently some modifications made to the robocasting process, also referred to as direct ink writing, by Gratson *et al.* have enabled the formation of polyelectrolyte structures with a feature size of ~1 μm.[78] This was followed by a sequential silica/silicon chemical vapor deposition process and etching away of the polymer template to yield hollow layer-by-layer type photonic crystals with micron scale resolution.[79] Band gaps were recorded at ~100 THz frequencies. Three dimensional photonic crystals using alumina have been built with feature size on the order of 2 mm and a PBG was observed around 20 GHz using the fused deposition modeling technique.[80]

## 2.3.Electro-optically tunable dielectrics

Under the application of an external static electric field, a dielectric material will undergo charge displacement process to form dipoles and is said to be polarized. Contributing polarization mechanisms can be of 4 different types:[81]

1. Atomic polarization: relative motion of electron cloud with respect to the nucleus
2. Ionic polarization: rearrangement of ionic species within a crystal lattice for e.g. NaCl
3. Dipolar polarization: orientation of permanent dipole moments e.g., in $H_2O$
4. Space charge polarization: Due to limited transport of charge carriers e.g. transport of charged species blocked by a grain boundary in ceramics

A special class of dielectric materials called ferroelectrics display a spontaneous polarization in the absence of an external electric field due to coupling of ionic displacements across large regions called domains. Large 90° or 180° domains exist within the material where electric dipoles are synchronously aligned. Such materials often have a high dielectric constant and display a ferroelectric hysteresis loop as shown in Figure 2.6.

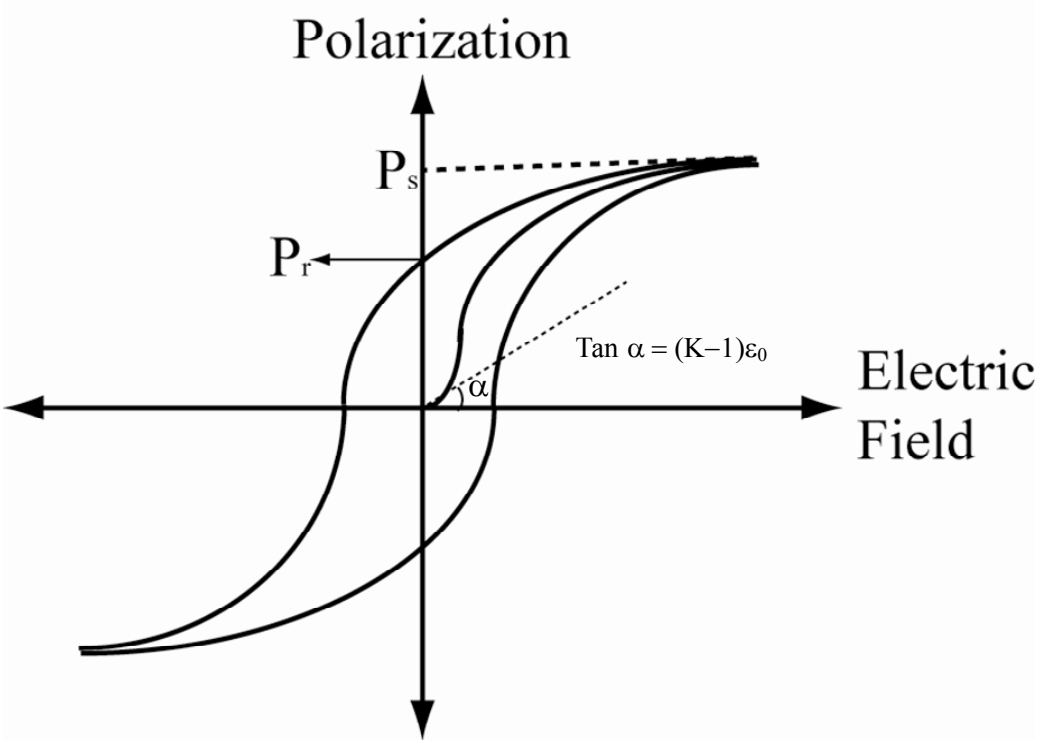


Figure 2.6 A ferroelectric hysteresis loop showing the effect of applied electric field on the polarization.

For low field strengths in an unpolarized material, the polarization is initially reversible and nearly linear with applied field. The slope of the curve at this initial linear region gives the initial dielectric constant for the material. As the magnitude of applied field is increased, a greater number of domains are aligned with the field until a saturation value ($P_s$) is reached. Upon removal of the external field, some domains remain oriented resulting in a remnant polarization, $P_r$. Barium titanate ceramic is a well known ferroelectric material whose perovskite structure is discussed in more detail in Chapter 4.

For the case of sinusoidally applied electric field, as in the case of the propagation of an electromagnetic wave through a dielectric medium or the application of an

alternating current across the terminals of a capacitor which contains a dielectric material, charge displacement processes vary in their ability to respond to the frequency of the switching field as shown in Figure 2.7. Thus while atomic polarization contributes to the dielectric constant at frequencies upto $10^{15}$ Hz, dipolar polarization can only exist upto approximately $10^{10}$ Hz. Hence as the frequency of the applied field increases, the dielectric constant will decrease as available polarization mechanisms decrease.

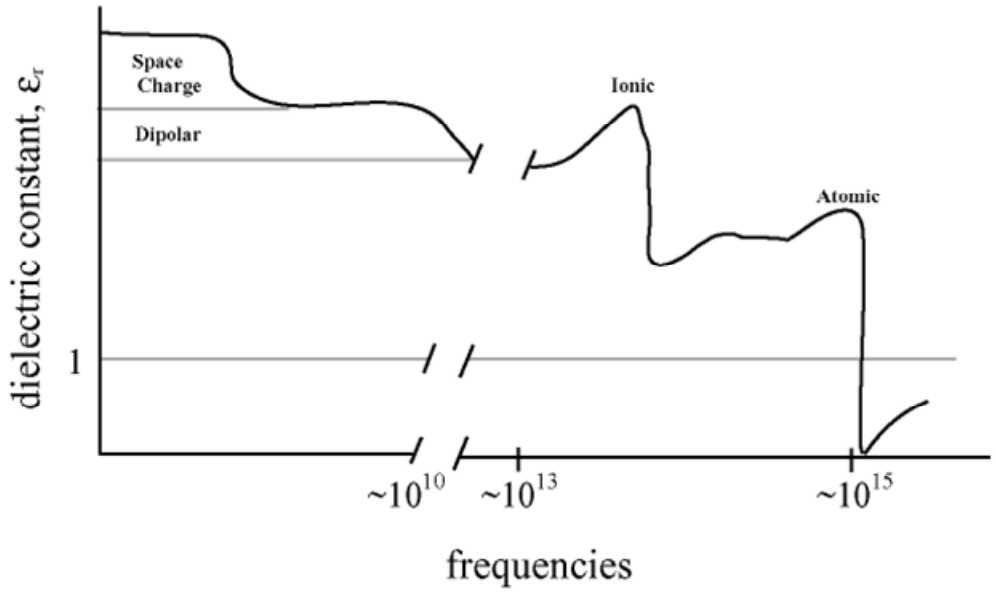


Figure 2.7 Contribution of various polarization mechanisms to the dielectric constant for dielectric materials

Electromagnetic waves consist of orthogonal sinusoidal electric and magnetic fields that can interact with the dielectric medium by polarizing it. When an electromagnetic wave travels through a dielectric material there is a change in velocity and intensity described by the frequency dependent complex coefficient of refraction:

$$n^* = n_1 + in_2 \qquad (2.27)$$

where $n_1$ is the index of refraction of and $n_2$ is the index of absorption. The coefficient of refraction is related to the complex dielectric constant as:

$$n^{*2}=\varepsilon_r+i\varepsilon_i \tag{2.28}$$

where $\varepsilon_r$ is the relative dielectric constant and $\varepsilon_i$ is the relative dielectric loss factor.

Under normal circumstances, the refractive index of a material is considered constant and the oscillations of the polarization mechanisms are small. However, if a sufficient bias field is applied to the dielectric, the refractive index (and dielectric constant) is found to vary in a non-linear way that can be described by a power series such as:

$$n=n^0 + aE_0 +bE_0^2..... \tag{2.29}$$

where $n^0$ is the refractive index under zero biasing field and a, b are material dependent constants and $E_0$ is the applied biasing field. . Hence, if the magnitude of the linear and quadratic terms is sufficient, the dielectric is considered tunable. This is shown schematically in Figure 2.8 below, partly reproduced from Moulson,[81] where polarization is affected by an applied field and effectively changes the refractive index for a E.M. wave passing through the material.

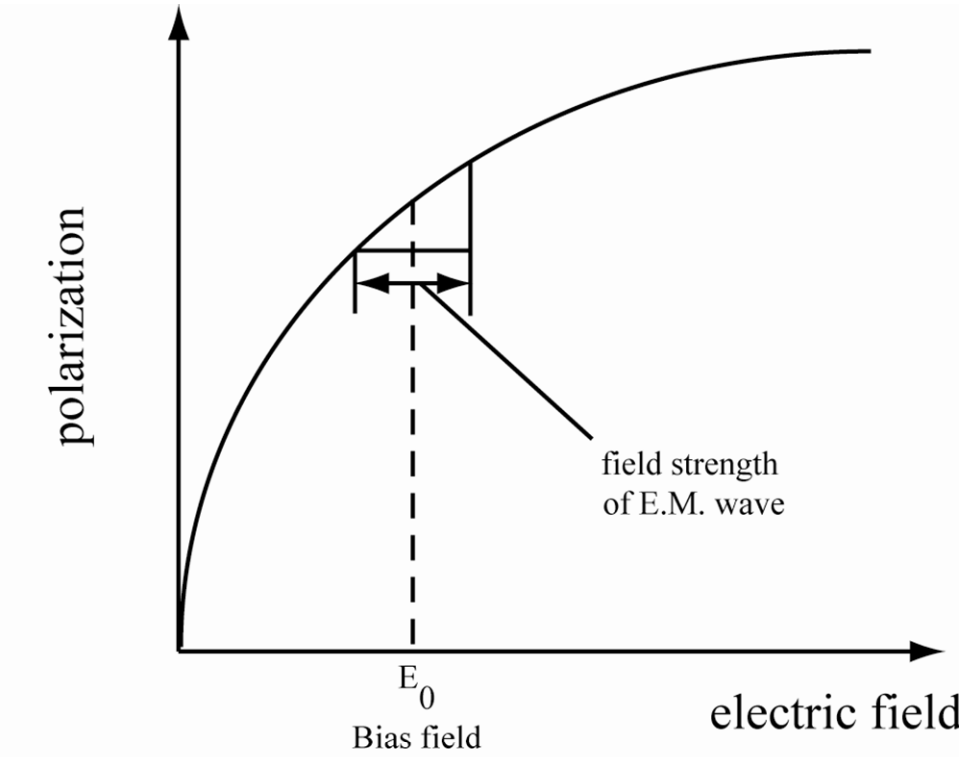


Figure 2.8 Effect of biasing field on the polarization and the modulated refractive index for an E.M. wave passing through the material

The materials system of barium strontium titanate (BST) has been extensively studied for low loss tunable applications.[82-89] Near ferro-electric materials, as found in BST composite, which rearrange domains on application of a DC voltage can provide a method of tunability of the dielectric constant and in turn of the photonic band gap[4] exhibited by a photonic crystal made using this material. One of the motivating hypotheses of this thesis is that since ferroelectric materials such as BST solid solutions display large tunability, the variation in refractive index may allow for a tunable photonic band gap.[4] One drawback to materials that have high tunability, such as BST is a high dielectric constant which tends to decrease mid-gap frequencies of the photonic band gap.

One way of decreasing the dielectric constant is to mix a low dielectric constant material (e.g., barium zirconate) with the BST to decrease the dielectric constant while retaining the perovskite structure and dielectric tunability. State of the art tunable capacitors for tunable electric filters are engineered around these principles. Some examples of such devices are barium titanate mixed with strontium titanate for use in ferroelectric random access memories (FRAMs),[90-98] phase array antennas,[99-103] decoupling capacitors,[104-107] and filter capacitors.[108] Some other dielectric modifiers for barium titanate are barium zirconate,[11, 109-111] magnesium oxide[112] and magnesium titanate[113] which can suitably decrease permittivity while maintaining tunability in the composite.

# 3. COLLOIDAL PROCESSING OF BARIUM TITANATE, STRONTIUM TITANATE AND BARIUM ZIRCONATE FOR DIRECT WRITE

Concentrated, aqueous colloidal gels of barium titanate (BT), strontium titanate (ST) and barium zirconate (BZ) were formulated for use as ink in a direct write, solid freeform fabrication process. ST and BZ ceramic powders could be processed for ink development in a way identical to the BT ceramic powder. Gelation studies were conducted on BT particles alone, to minimize material consumption and time, and results extended to the ST and BZ particle systems. A similar approach to processing for all three particle system also allowed for processing compositional mixtures as described in following chapters.

## SECTION I: COLLOIDAL PROCESSING OF BARIUM TITANATE INKS

### 3.1.Introduction

Direct write technologies provide a robust technique for freeform fabrication of structures that are not easily formed by traditional machining and molding processes. Current direct write technologies differ with respect to resolution, write speed, ability to write 2-D or 3-D structures and multi-material capabilities.[114] Although sub-micron printing has been demonstrated with methods such as dip-pen nanolithography,[115]

focused ion beam lithography,[116] and laser direct write micromachining,[117] these methods are often restricted to making components with sub millimeter overall dimensions. Structures with larger feature size and overall dimensions have been fabricated using techniques such as robocasting,[9, 10, 56, 57, 59, 118] ink jet printing,[119] hot melt printing,[120] and micropen writing,[121] with demonstration of a wide variety of building materials.

Robocasting is unique among these techniques in that it requires the use of only a small volume fraction of organics and is amenable to colloidal processing techniques. In robocasting, ink design and the ensuing ink dynamic response upon printing play crucial roles in affecting both print resolution and the structural integrity of the deposited layers. Precise ink formulation allows the fabrication of space filling solids[59], high aspect ratio walls[57] and spanning (unsupported) elements.[9, 10, 53, 55, 61] The current study was performed to develop aqueous colloidal gels of barium titanate for use as ink in robocasting and to provide insight about the dynamic properties of the ink upon deposition.

Robocasting is an extrusion-based, direct write technique, the relevant processing steps of which include formulation of the colloidal ink, the printing operation, and finishing processes. The colloidal inks are formulated in consideration of several criteria. The ink must: (1) possess rheological behavior that facilitates flow through small diameter nozzles under modest application of pressure, (2) solidify rapidly after exiting the deposition nozzle to maintain the desired shape, and (3) contain a high volume fraction (ca. 0.45-0.50) of colloidal particles to resist drying induced stresses that may lead to warping, cracks and residual stress in the deposited green bodies. Ink formulations consist of first creating a uniform, high concentration – low viscosity

slurry.[9, 10] High solids loading, in addition to increasing the green body density, minimizes drying shrinkage[122] by increasing the compressive yield stress ($P_Y$) of the particle network. Next, a fluid-to-gel change is induced to yield flow properties suitable for the printing operation. The printing operation utilizes a motion and flow rate controlled deposition system similar in concept to a three-axis computer numerical control (CNC) mill with the exception that the cutting tool is replaced by the deposition nozzle. Colloidal inks are housed in syringes affixed to the *z* motion axis and connected to the deposition nozzle. A model of three-dimensional structure to be assembled is virtually sliced into layers and deposition tool paths are calculated using a computer aided design (CAD) program. The layers are deposited (printed) sequentially, starting with the bottom layer. After the printing operation, the structure is dried and sintered to yield a dense ceramic.

The equilibrium elastic properties of the colloidal gel ink have been shown to depend both on particle concentration and inter-particle potentials. Previous development of colloidal gel based inks showed that, at a constant solids loading, the inter-particle attractive potential could be altered to produce the desired rheological behavior. The power law scaling behavior of colloidal gel elastic properties can be described by:[60]

$$y = k\left(\frac{\phi}{\phi_{gel}} - 1\right)^{x} \tag{3.1}$$

where $\phi$ is the solids volume fraction, $\phi_{gel}$ is a minimum solids loading for gelation to occur, $k$ is a system specific pre-factor, $x$ is a scaling exponent (~2.5), and $y$ is the property of interest (e.g., shear yield stress ($\tau_y$), shear modulus ($G'$), and compressive

yield stress ($P_Y$)). As the particles are made more attractive, $\phi_{gel}$ decreases, resulting in a more rigid gel. Likewise, as drying occurs, $\phi$ increases to strengthen the gel.

The aims of this study were twofold: First, the equilibrium gel properties of $BaTiO_3$ gels prepared with inorganic salts or cationic poly(electrolytes) as flocculants were investigated to gain insight about the mechanisms leading to gelation and the resulting gel properties. Second, the dynamic recovery of elastic properties of $BaTiO_3$ gels was probed to better understand the behavior of colloidal gel inks immediately after extrusion from the deposition nozzle. To test the suitability of the inks developed here for the robocasting process, three-dimensional periodic structures were deposited that consisted of linear, circular and radial arrays of ~100 μm diameter filaments.

## 3.2. Experimental section

### *3.2.1. Materials System*

Barium titanate (Ticon HPB, Ferro Electronics Corporation, Penn Yan, NY) with an average particle size of 1.02 μm, surface area 3.2 $m^2/g$ and a density of 5.5 $g/cm^3$ served as the ceramic phase. An aqueous solution of the ammonium salt of poly(acrylic acid) (APA) (Darvan 821A, R.T. Vanderbilt Co., Norwalk, CT) was used as the electro-steric stabilizer. Hydroxypropyl methylcellulose (HPMC) (Methocel F4M, Dow Chemical Co., Midland, MI.) with a molecular weight of 3500 was prepared in a 5 wt% stock solution and used as a viscosifier. Aqueous phase pH adjustments were made using 1N $HNO_3$ (Fisher Scientific, Pittsburg, PA) and 1N $NH_4OH$ (Fisher Scientific, Pittsburg, PA). Sodium chloride (EM Science, Gibbstown, NJ) and barium chloride (Fisher

Scientific, Fair lawn, NJ) were prepared as concentrated aqueous stock solutions of 4M and 1 M respectively. Non linear poly(ethylenimine) (PEI), $M_w$=50,000-100,000 (ICN Biomedical, Aurora, OH) ($PEI_{100K}$), $M_w$ =25,000 (Sigma-Aldrich Co. St. Louis, Mo) ($PEI_{25K}$), and $M_w$ = 2000 (Sigma-Aldrich Co. St. Louis, Mo) ($PEI_{2K}$) were prepared in aqueous stock solutions with 10% by weight polymer and their pH was adjusted to a constant value of 10.8. All samples were prepared in de-ionized water having a nominal conductivity of 5 X $10^{-4}$ $\Omega^{-1}cm^{-1}$.

### *3.2.2. Colloidal gel preparation*

Concentrated barium titanate suspensions (45-50 volume%) were created by adding a predetermined amount (0.5 wt% based on barium titanate weight) of Darvan 821A to de-ionized water in a 250 ml HDPE bottle (Nalge Nunc Intl., Rochester, NY) containing 11, 1/4" YZT grinding media (Nikkato Corporation, Japan). Barium titanate powder was then added to this solution to create a ceramic suspension at high solids concentration ($\phi_{solids}$=0.45-0.50). The slurry was shaken on a paint shaker (Model 5400, Red Devil Equipment Co, Plymouth, MN) for approximately 2 hours to break apart soft agglomerates and obtain a well dispersed suspension. Next, an appropriate amount of HPMC, was added as a viscosifier such that the cellulose concentration in the aqueous phase was 5 mg/ml. This stock suspension was subdivided into 50 ml batches and gelled by addition of inorganic salt or PEI. All gels used in rheological measurements had solids loading $\phi$=0.49 and HPMC concentration [HPMC] = 5mg/ml of the aqueous phase.

### *3.2.3. Zeta Potential Measurements*

The zeta potential of BT in aqueous suspension with and without the ammonium polyacrylate was measured as a function of pH using an acoustic spectrometer (DT 1200, Dispersion Technologies, NY). Two 250 ml samples were prepared at 10 volume% solids concentration. The first consisted of bare barium titanate particles in water and the second consisted of a similar suspension to which 0.5 wt% APA by weight of barium titanate had been added to understand the effects of dispersant on suspension stability. The zeta potential was measured for each across a pH span from 2-12 without added background electrolyte.

### *3.2.4. Rheological Characterization*

#### 3.2.4.1. Viscosity and Modulus measurements on flocculated inks

The rheological behavior of the inks was characterized using a controlled stress-strain rheometer (Model CVOR 200, Bohlin Instruments, East Brunswick, NJ). To prevent wall slip, a cup and bob geometry (C14, cup I.D. =16 mm and bob O.D. = 14 mm) with serrated walls was used. Further, to prevent sample evaporation during the long periods required for measurements, the measuring geometry was fitted with a custom made solvent trap. Each measurement required a sample size of 3.8 ml which was loaded into the cell using a plastic syringe.

For each measurement of elastic modulus, a pre-shear of $1s^{-1}$ was applied for a period of 60 seconds to the loaded sample. Then, the sample was left undisturbed for an hour to attain an equilibrium state. Next, the rheometer applied a logarithmically increasing oscillatory shear to the sample. Each measurement was made over 10

oscillations and a wait time of 30 seconds was allowed between consecutive measurements to minimize the influence of the previous measurement. The shear stress range probed was varied accordingly to ensure collection of data in the linear visco-elastic region (LVER) and the shear yield stress ($\tau_y$) for varying gel strengths.

3.2.4.2. Modulus recovery measurements

The dynamic behavior of the extruded ink after exiting the nozzle plays an important role in the shape evolution of the deposited structure. Modulus recovery measurements were carried out on the gelled inks by applying a pre-shear using two different methods, (1) A continuous pre-shear of $1s^{-1}$ for a period of 60 seconds as in the equilibrium modulus measurements and (2) An oscillatory pre-shear using a strain of 1 at 1 Hz for a duration of 60 seconds. Immediately following the cessation of this pre-shear period, modulus measurements were carried out on the sample at an oscillatory strain of $10^{-4}$. Oscillatory modulus readings were taken over 3 cycles for the period of an hour using zero delay or wait time between measurements. A small strain was applied instead of a small shear stress to avoid exceeding the time varying yield strain of the sample and influencing the active modulus recovery process.

*3.2.5. Fabrication of 3-D structures using ceramic inks*

Diverse three-dimensional periodic structures were fabricated to demonstrate the suitability of these newly formulated inks for use in the robotic deposition process. An extrusion based robotic deposition device (Aerotech Inc., Pittsburg, PA) with custom written control software was used as the direct write tool. Ceramic inks were housed in syringes (1ml or 3ml, BD Inc., NJ) equipped with blunted stainless steel tips of various

I.D. (EFD Inc., East Providence, RI). The deposition process was carried out on a flat substrate submerged in an oil bath to prevent drying of the colloidal ink during deposition. After the deposition step was completed, the oil was drained, the structures dried in ambient air for a minimum of 12 hours and then sintered in an electric furnace (Model LHT 02/17, Nabertherm, Germany) on zirconia setter plates. A sintering schedule of 25 $^{o}$C -1340 $^{o}$C (2.8$^{o}$C/min), 1340$^{o}$C (60 min), and 1340 $^{o}$C -25 $^{o}$C (4.4 $^{o}$C/min) was followed.

## 3.3.Results and discussions

### *3.3.1. Slurry Formation*

For the $BaTiO_3$ inks prepared in this work, APA (an anionic poly(electrolyte)) was adsorbed on the particle surface to promote stabilization. A surface saturation of APA was reached at ~0.625 mg/m$^2$ (or 0.002 $m_{APA}/m_{BaTiO3}$) as determined by minimum sediment height in a settling experiment not described here. Excess APA had little effect on the colloidal stability. Figure 3.1 shows the zeta potential ($\zeta$) behavior of bare and APA coated barium titanate particles in suspension.

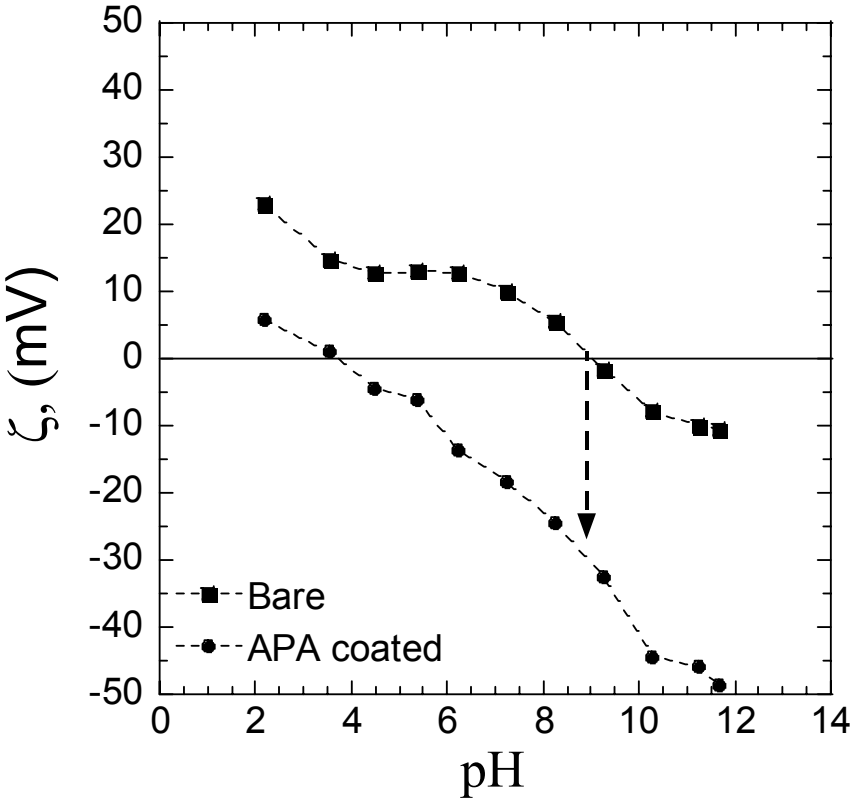


Figure 3.1 pH dependance of zeta potential for as-received and APA coated $BaTiO_3$

The bare particles displayed an iso-electric point around pH=8.5. At lower pH, the bare particles became positively charged with a maximum $\zeta \approx 25$ mV. At lower pH values, barium leaching from the particles is known to be problematic,[123-126] thus a pH range greater than 9 was chosen for processing. The addition of the APA shifted the iso-electric point of the coated particles to pH≈4. In the chosen processing range, the APA was ionized and provided sufficient colloidal stability to formulate suspensions with $\phi \geq 0.5$.

### *3.3.2. Gel formation*

Gelation of colloidal suspensions is achieved when a spanning particle cluster is formed as a result of increasing the attractive potential between particles.[127] The robocasting process requires colloidal gels that satisfy two important criteria:[9] First, the gel must flow through orifices as small as 100 μm (i.e., the deposition nozzle) and then quickly set upon deposition to retain the desired shape. Second, $\phi$ of the gel must be sufficiently high to resist drying stresses. As described in equation 3.1, the strength of a colloidal gel increases with a decrease in $\phi_{gel}$ at a constant $\phi$. $\phi_{gel}$ decreases as the mechanisms causing stabilization are removed or diminished or new mechanisms for particle attraction are added to the system. Since the barium titanate suspension was stabilized by an electro-steric mechanism, three methods, (i) pH change, (ii) salt addition, and (iii) bridging flocculation, were explored to cause flocculation of dispersed suspensions.

#### 3.3.2.1. Gelation using a pH change

Gelation of barium titanate suspensions using a pH change was rejected based on leaching of barium ions from the particle surfaces at pH lower than 9.[123-126] Additionally, while acid titration gelled the suspensions, the reactivity of the $BaTiO_3$ particles led to a time-dependent pH rise and partial re-stabilization of the suspension. It is suspected that the carboxylic acid groups on the adsorbed APA may capture some of the $Ba^{2+}$ ions and drive the equilibrium further towards the alkaline domain. Given the difficulty in controlling the gel properties by pH change, this mechanism was abandoned as a viable alternative.

3.3.2.2. Gelation using electrolyte salts

The elastic shear modulus (G') of $BaTiO_3$ suspensions gelled with NaCl and $BaCl_2$ additions is shown in Figures 3.2 and 3.3, respectively, as a function of shear stress. For both NaCl and $BaCl_2$ additions, the suspensions underwent a fluid to gel transition and the data presented in Figures 3.2 and 3.3 represent salt concentrations well above this minimum gelation concentration. As the stress applied to each gel was increased, a linear visco-elastic region (distinguishable as the low shear stress, $G'_{eq}$ plateau) preceded a rapid decrease in G' at the characteristic shear yield stress, $\tau_y$. For $\tau > \tau_y$ the particle network was ruptured and the suspension became fluid in nature.

For both NaCl and $BaCl_2$ additions, an increase in salt concentration led to an increase in $G'_{eq}$ and $\tau_y$. The $G'_{eq}$ measured for the maximum $BaCl_2$ addition in this study was approximately 1.3 MPa; whereas a similar concentration of NaCl resulted in a $G'_{eq}$ ~0.9 kPa. Likewise, the maximum $\tau_y$ for the NaCl gelled suspensions was only ~9 Pa, but approached 200 Pa for the $BaCl_2$ gelled suspension.

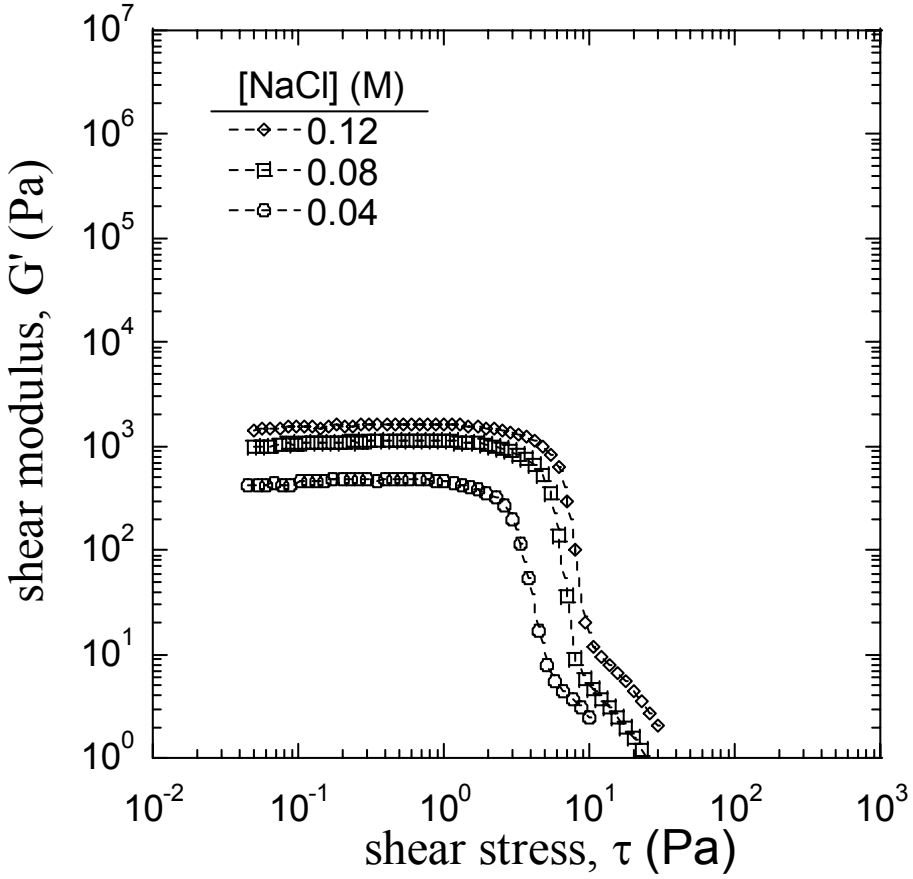


Figure 3.2 Shear stress dependant behavior of G' for Φ=0.49 $BaTiO_3$ gels of varying NaCl concentration

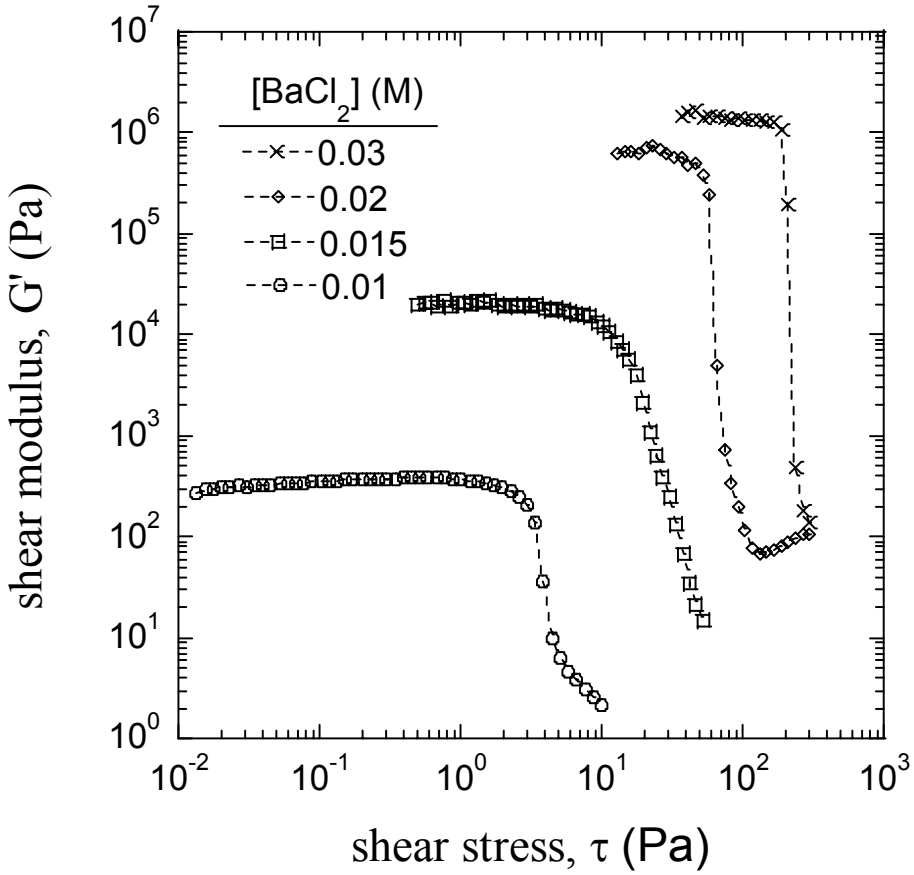


Figure 3.3 Shear stress dependant behavior of G' for Φ=0.49 $BaTiO_3$ gels of varying $BaCl_2$ concentrations

Figure 3.4 shows the scaling of $G'_{eq}$ as a function of salt concentration for the barium titanate suspensions. The rate of increase in $G'_{eq}$ for $BaCl_2$ additions was much greater than that derived from NaCl additions. It is well known, however, that divalent cations are more potent than monovalent cations at screening charged particles, when compared on a molar concentration basis.[128] Thus, to fairly compare the gelling behavior of NaCl and $BaCl_2$, the equilibrium modulus was examined as a function of ionic strength in Figure 3.5. The ionic strength was calculated according to equation (3.2): [129]

$$\text{Ionic strength} = (\tfrac{1}{2})\sum(M_i z_i^2) \qquad (3.2)$$

where $M_i$= molar concentration of the ionic species, and $z_i$=valency of the ion.

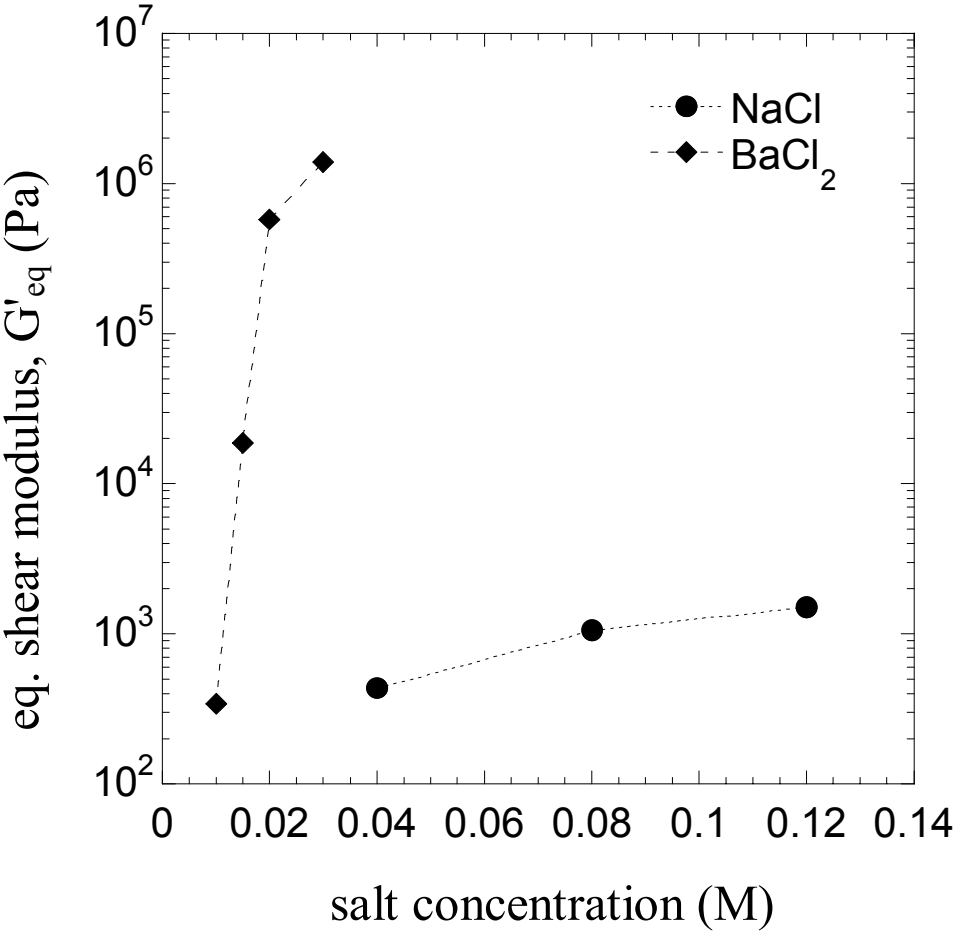


Figure 3.4 Summary of G'eq measured Φ =0.49 BaTiO3 gels as a function of molar concentration

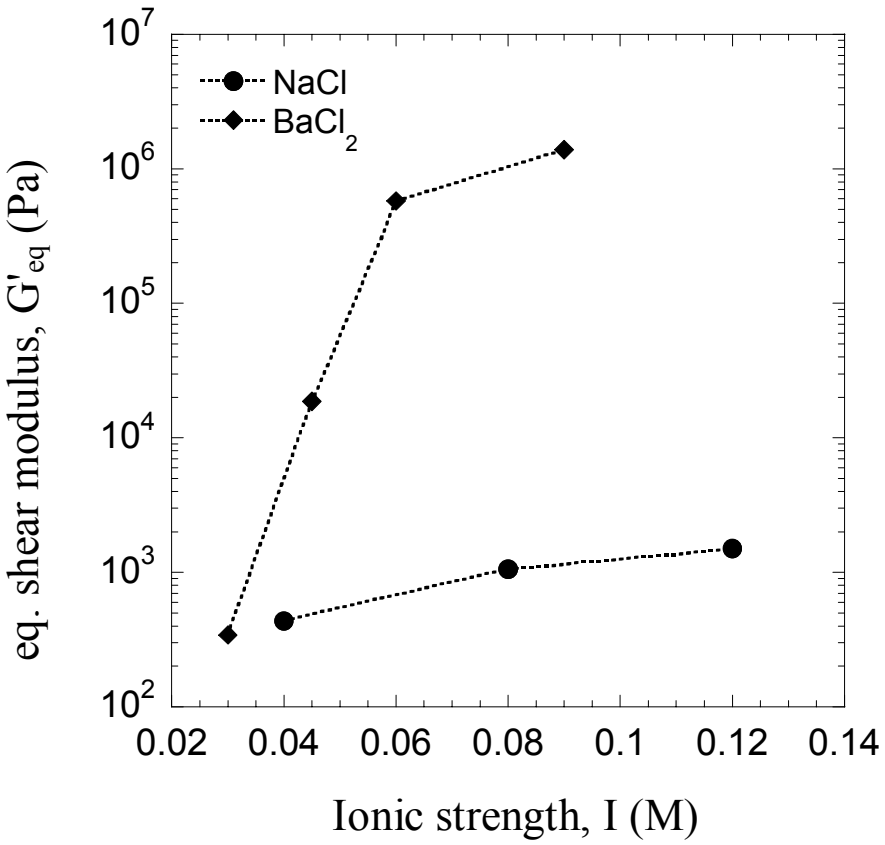


Figure 3.5 Summary of G'eq measured Φ =0.49 BaTiO3 gels as a function of ionic strength

For the monovalent NaCl addition, the only available mechanism for reducing the electro-steric stabilizing force between particles was the screening of charge; both between particles and within the adsorbed APA layer. The effect of this screening was a reduction of the repulsive electrostatic potential between particles and, perhaps, a slight contraction of the adsorbed polymer layer due to conformational changes of the APA.

The effect of both of these mechanisms was weak, likely due to residual steric forces of the contracted APA layer, as were the resulting gels.

Comparatively, the effect of the divalent $BaCl_2$ on gel properties was strong and was attributed to an additional mechanism. The divalent $Ba^{2+}$ cation has the potential to complex with up to two carboxylic acid groups on the APA molecules. In principle, this complex could be self-contained within the APA layer of a single particle, thus causing a contraction of the polymer layer thickness. Alternatively, the complex could bridge polymer chains adsorbed to separate particles, thus acting as a bridging flocculant. This phenomenon has been previously described by Li and co-workers[58] for flocculation of nano-sized BT powders using mono and divalent cations where they attributed a higher degree of flocculation to ion-bridging effects between charged APA chains adsorbed on different nano-particles in suspension. The extent to which the additional mechanism of ion complexation with the adsorbed APA affects gel strength is evident in Figure 3.5 as the difference in $G'_{eq}$ at equivalent ionic strengths for NaCl and $BaCl_2$ additions. Since the $Ba^{2+}$ is much smaller than the APA layer thickness (~9nm maximum), it is likely that most of the complexed $Ba^{2+}$ is engulfed in the dispersant layer of a single particle, and only a small fraction of the divalent cations participate in inter-particle bridging. Quantification of the fraction of $Ba^{2+}$ ions participating in inter-particle bridging was beyond the scope of the current study.

#### 3.3.2.3. Gelation by bridging flocculation with cationic polyelectrolyte

A cationic polyelectrolyte, poly(ethylenimine) (PEI), was used as a flocculant for concentrated, APA stabilized $BaTiO_3$ slurry. PEI is a highly branched aliphatic

polyamine that contains primary, secondary and tertiary amine groups in a ~1:2:1 ratio and possess a spherical morphology.[130] At pH < 11, the primary amine groups can ionize resulting in a net positive charge for the PEI molecule. PEI is a common cationic polymer used in the layer-by-layer assembly methods for building multilayer, nanoscale composites.[131] For the design of the concentrated colloidal gels used in robocasting, the anionic base layer is the APA coating on the $BaTiO_3$. The second polymer layer is PEI; however the PEI concentration is kept below that needed to form a monolayer and, thus, may act as a bridging flocculant.

Figures 3.6-3.8 show oscillatory rheology data gathered for $\phi = 0.49$ $BaTiO_3$ gels flocculated with $PEI_{2K}$, $PEI_{25K}$, and $PEI_{100K}$. For each PEI molecular weight, the molarity was calculated as the number of polyelectrolyte molecules present in 1 liter of the suspension based on the weight- average molar mass of the PEI. The weight % PEI for each suspension was varied from 0.008 to 0.034% (on a basis of suspension weight) in each case. For each of the three PEI molecular weights used, the oscillatory measurement revealed a distinct linear visco-elastic region and yield stress. As expected, an increase in PEI concentration resulted in an increase in both $G'_{eq}$ and $\tau_y$ in all cases. The magnitudes for $G'_{eq}$ and $\tau_y$ were found comparable with those obtained by using $BaCl_2$ additions. For example, a $[PEI_{25K}] = 4.25$ μM gel achieved a $G'_{eq} \approx 1$ MPa and $\tau_y \approx$ 130 Pa.

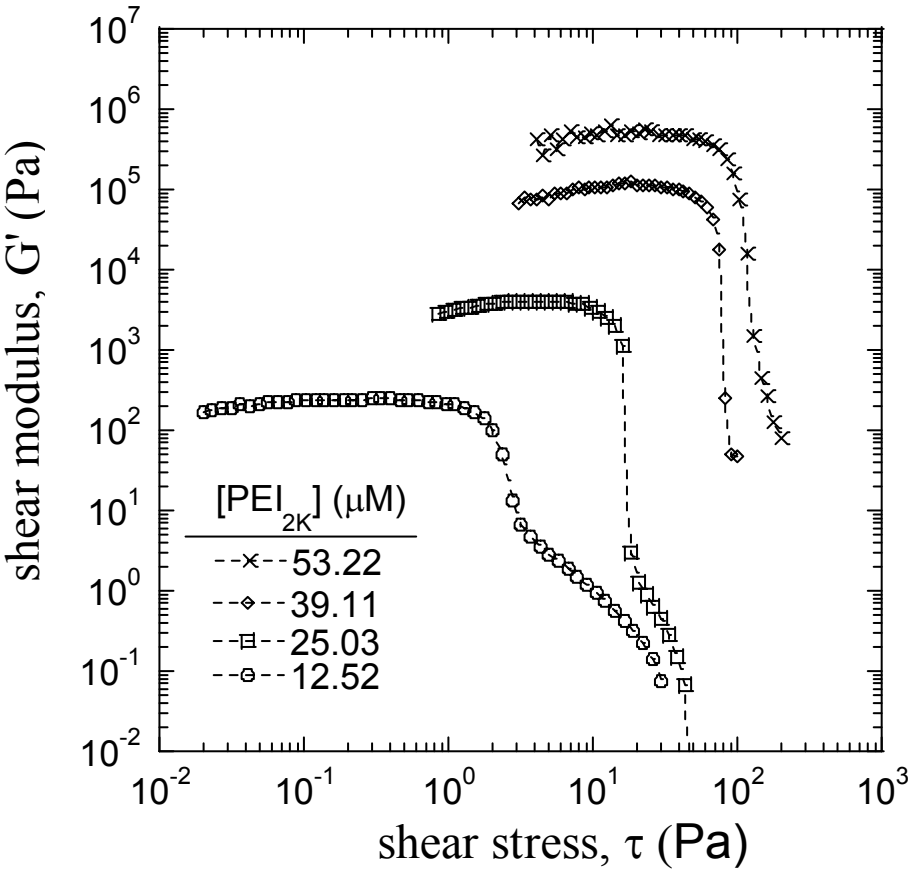


Figure 3.6 Shear stress dependent G' behavior for Φ =0.49 $BaTiO_3$ gels with varying concentrations of PEI of molecular weight 2,000

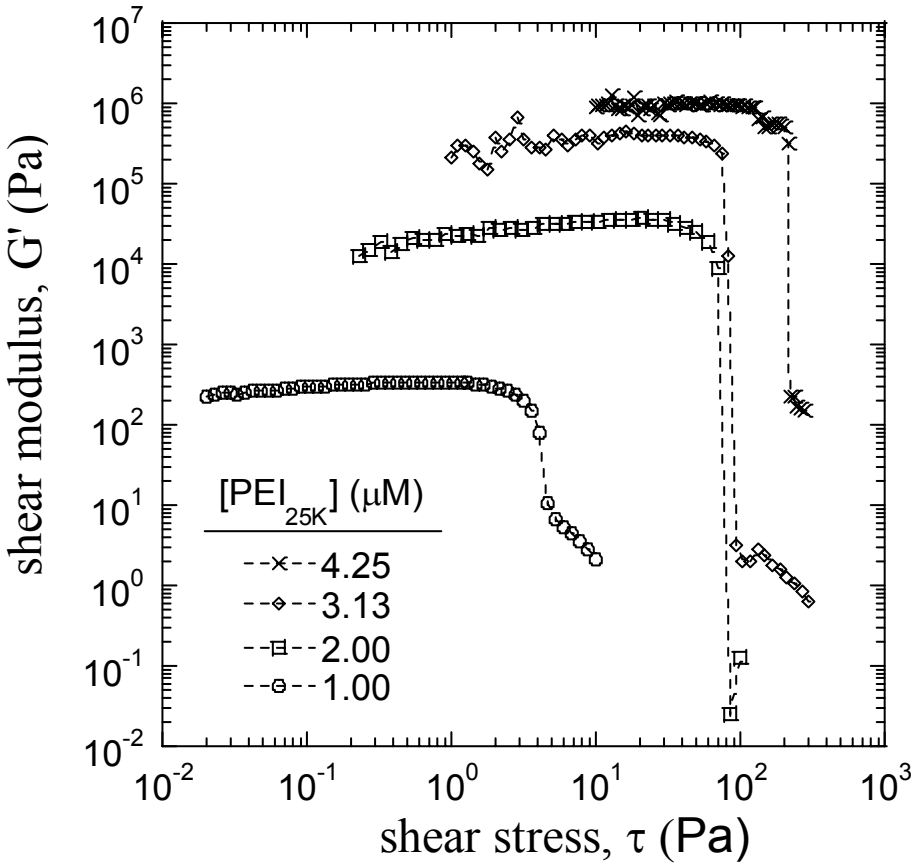


Figure 3.7 Shear stress dependent G' behavior for Φ =0.49 $BaTiO_3$ gels with varying concentrations of PEI of molecular weight 25,000

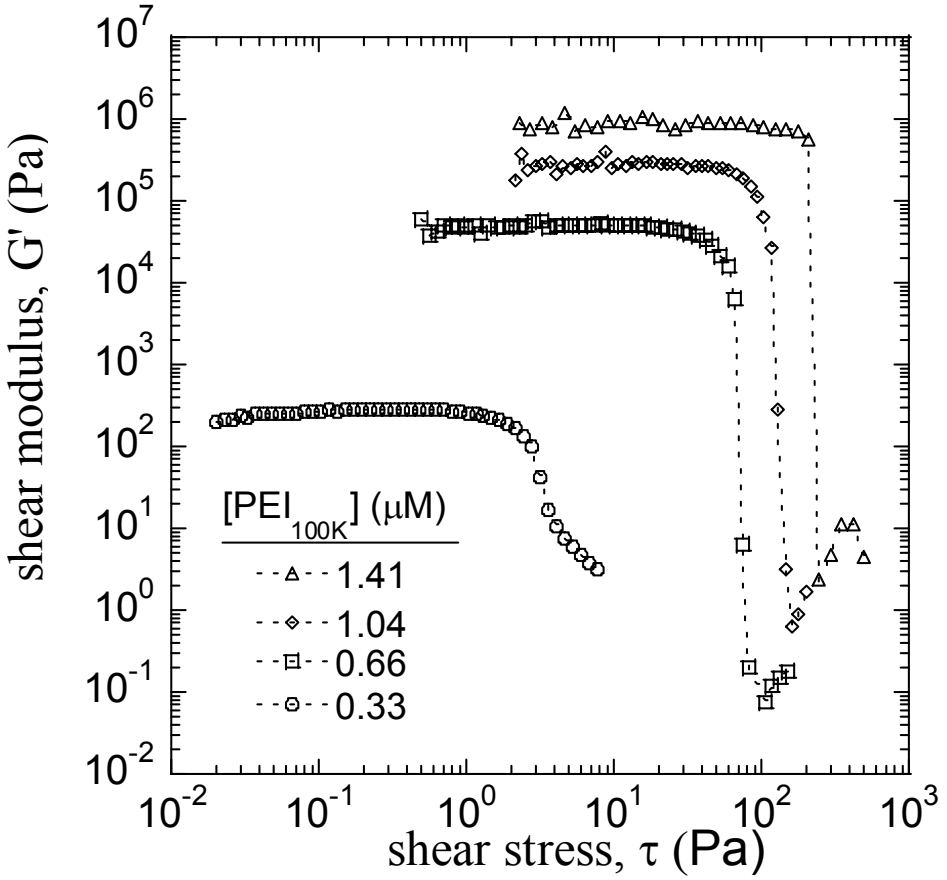


Figure 3.8 Shear stress dependent G' behavior for Φ =0.49 $BaTiO_3$ gels with varying concentrations of PEI of molecular weight 50,000-100,000

Figure 3.9 shows the increase in the $G'_{eq}$ value as a function of the molarity of PEI in the gel and the molecular weight of PEI used. All three molecular weight PEI showed an almost linear increase in the $G'_{eq}$ with increasing logarithm of molar concentrations. It was also observed that to attain a particular $G'_{eq}$ the concentration of PEI required was inversely proportional to its molecular weight; although, the $PEI_{100K}$ and $PEI_{25K}$ showed similar gel strengths as a function of molarity. The $PEI_{2K}$ gel, on the other hand, required

almost 40 times the concentration as the higher molecular weight PEI to show comparable visco-elastic properties. The $PEI_{2K}$ was able to achieve high $G'_{eq}$ values with increased concentration.

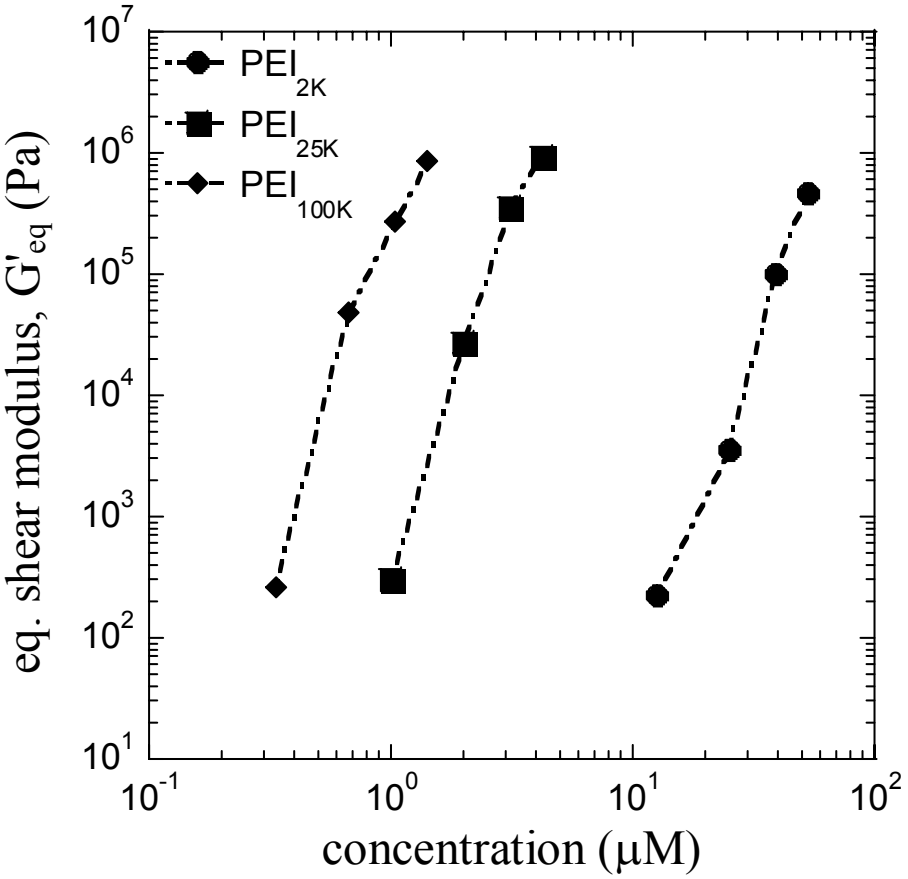


Figure 3.9 Summary of $G'_{eq}$ dependence on PEI concentration for $\Phi$ =0.49 $BaTiO_3$ gels

As described earlier, the $Ba^{2+}$ ion had a statistical probability of bridging two APA stabilized $BaTiO_3$ particles if it formed a complex with APA molecules on adjacent particles. Being of atomic dimensions and +2 valence, a single $Ba^{2+}$ cation

could, at most, join only two APA chain segments. On the other hand, the PEI molecules possess an abundance of positive sites and the potential to complex with numerous APA chain segments. Certainly, steric hindrance will limit the number of APA chains that can complex with a single PEI molecule; however, the probability that a PEI molecule will form inter-chain complexes should increase with the size of the PEI molecule. The sizes of the three different molecular weight PEI were determined according to the Mark-Houwink parameters established by von Harpe *et al.*[132] and verified by infinite dilution capillary rheology experiments (not described here). The $PEI_{100K}$, $PEI_{25K}$, and $PEI_{2K}$ were computed to have a size (based on the hydrodynamic volume) of approximately 12 nm, 7 nm, and 2 nm, respectively. The modest increase in the linear size despite the large increase in the molecular weight can be attributed to the spherical morphology of the highly branched dendritic PEI molecule.

It is hypothesized that, as a PEI molecule of any molecular weight approaches the negatively charged APA polymer on the surface of the particles, complexation reactions allowed for PEI adsorption either (i) as a second layer atop the APA layer, or (ii) by incorporation into the APA layer. The smaller $PEI_{2k}$ molecule could be more efficiently enveloped within the APA polymer brush on the particle surface. Even if incorporated into the APA layer, the 2nm sized $PEI_{2K}$ may protrude sufficiently from the particle surface to enable bridging with adjacent particles. As the size of the PEI molecule increases, the fraction of PEI molecules that may form inter-particle complexes increases. This bridging efficiency will however be limited by the size of the APA polymer brush itself. Even the largest $PEI_{100K}$ at 12 nm is too small to bridge three particles due to stability considerations of packing negative and positive particles. This argument

explains the minimal difference between the gel properties of the $PEI_{25K}$ and $PEI_{100K}$ flocculated suspensions, which is attributed to the incremental increase in two particle bridging probability.

*3.3.3. Time and shear history dependence of elastic properties.*

During extrusion of the colloidal ink, the gel may adopt a three zone velocity profile, consisting of (1) An unyielded core of radius $r_c$ moving at constant velocity surrounded by (2) A yielded shell experiencing laminar flow and (3) A possible particle depleted, slip layer at the nozzle wall.[9] Hence, the gel structure remains nearly unchanged in the core region, but undergoes shear induced rupture in the shell region. Upon deposition, the gel structure is expected to rebuild as inter-particle bonds that were ruptured during flow are reformed. The gel structure recovery is accompanied by a rise of the shear modulus toward the equilibrium modulus of the unperturbed gel.

Figure 3.10 illustrates the time dependant rise in shear modulus after application of a 1 $s^{-1}$ pre-shear for $\phi$=0.49 $BaTiO_3$ gels flocculated with $PEI_{100K}$ at concentrations of (*i*) 0.008wt%, (*ii*) 0.016 wt%, (*iii*) 0.025 wt%. Figure 3.11 illustrates the results of a similar modulus recovery experiment using varying PEI species as flocculants, but at a constant concentration of 0.025 wt%. To capture the recovery of shear modulus immediately after application of a larger pre-shear, an oscillatory preshear[133] was used rather than a constant rate pre-shear due to observed flow of the gel out of the gap in the sample cup with application of a large continuous pre-shear. Figure 3.12 illustrates the rise in shear modulus after application of an oscillating pre-shear (strain amplitude=1,

frequency=1Hz) for $\phi$=0.49 $BaTiO_3$ gels flocculated with $PEI_{100K}$ at concentrations of (*i*) 0.008wt%, (*ii*) 0.016 wt%, (*iii*) 0.025 wt%.

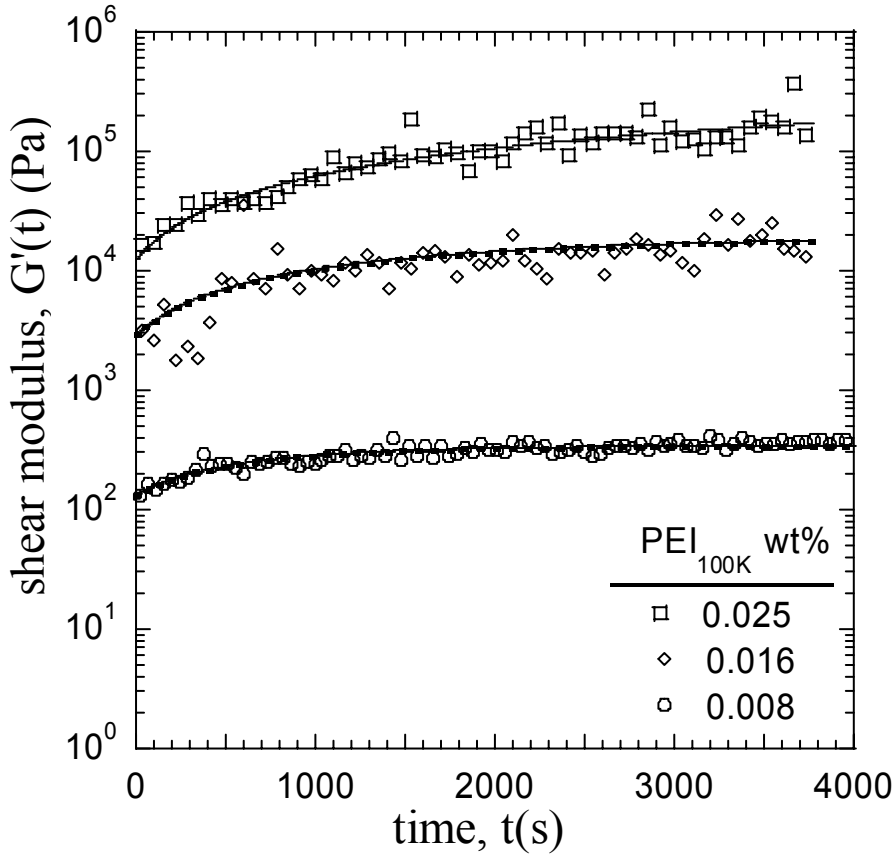


Figure 3.10 Time dependent recovery of G' for $\Phi$ =0.49 $BaTiO_3$ gels flocculated with $PEI_{100K}$ and a constant pre-shear. Solid lines represent the modeling based on an exponential decay fit

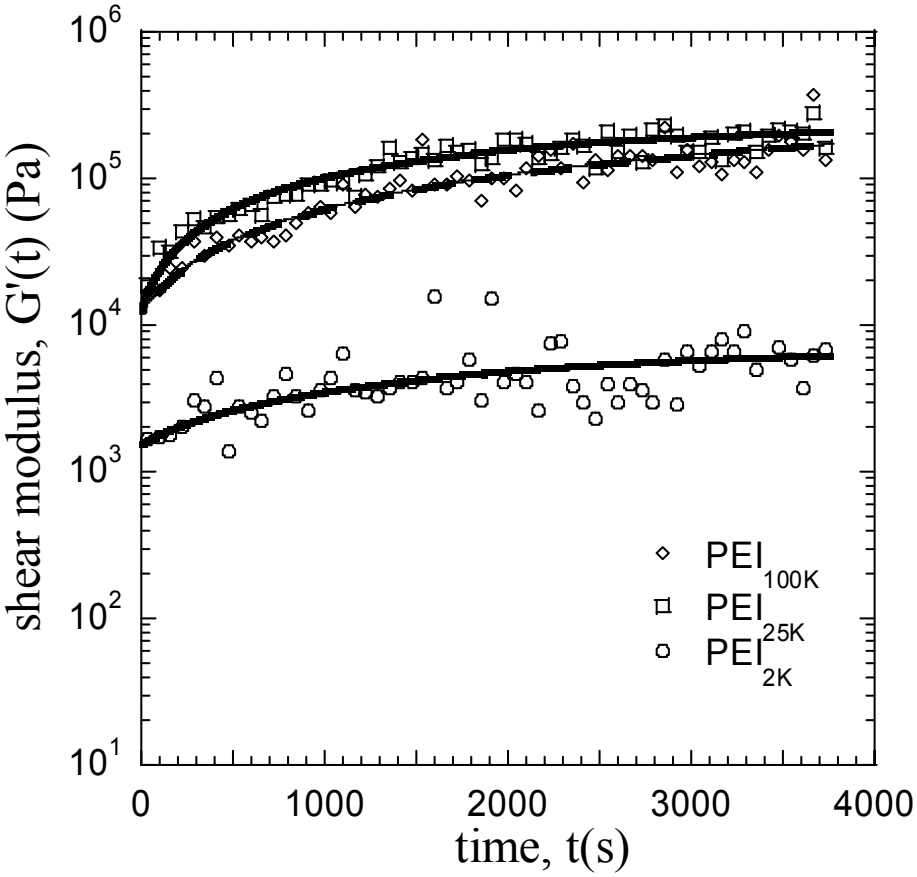


Figure 3.11 Time dependent recovery of G' for Φ =0.49 $BaTiO_3$ gels flocculated with various PEI molecular weights and a constant pre-shear. Solid lines represent the modeling based on an exponential decay fit

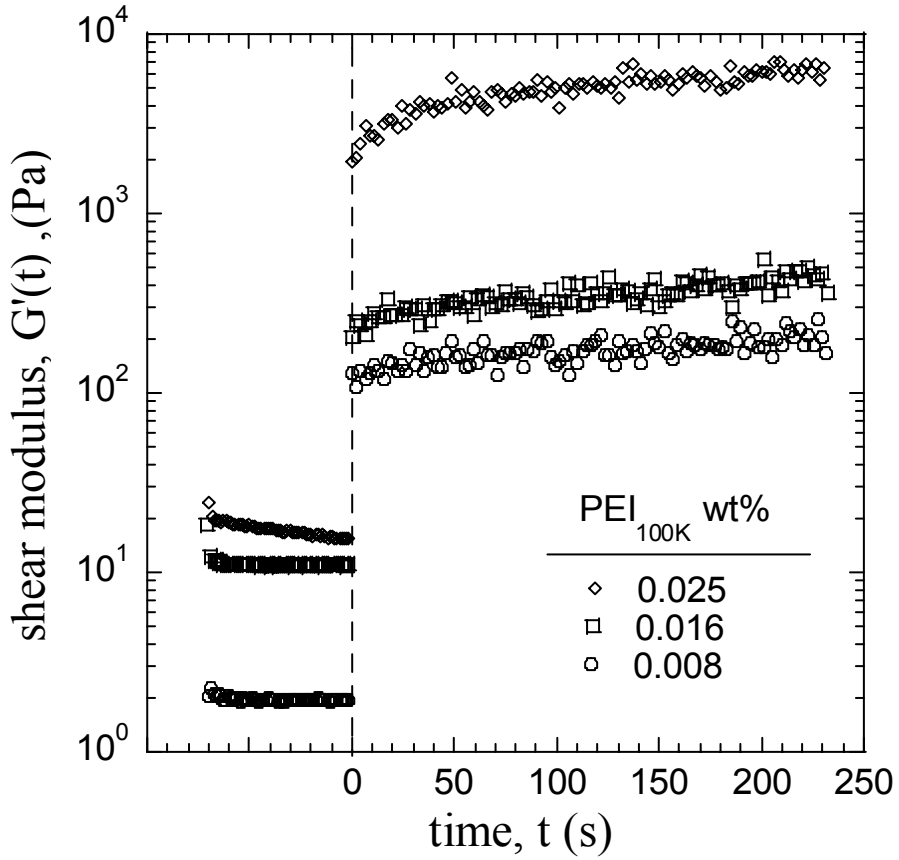


Figure 3.12 Time dependent recovery of G' for Φ =0.49 $BaTiO_3$ gels flocculated with $PEI_{100K}$ using an oscillatory pre-shear

Similar trends in shear modulus recovery were observed for each experiment in Figure 3.10-3.12 namely, a step change in modulus at t ≈ 0s ($G'_0$) followed by a gradual growth of shear modulus toward $G'_\infty$. As expected, the magnitude of $G'_0$ increases proportionally to gel strength as can be observed in Figure 3.10-3.12. Upon comparison of Figure 3.10 and 3.12, it was observed that the magnitude of $G'_0$ for equivalent gels was markedly lower for gels subjected to the large oscillating pre-shear. Such a difference is

not unexpected since the oscillating pre-shear degrades the gel structure more than the rather slow constant pre-shear. This magnitude for $G'_0$ in Figure 3.12 is likely more representative of the gel state close to the extrusion nozzle wall, where shear rates are on of the order $100s^{-1}$. It should be noted that the time between the cessation of the large strain and the time at which the small amplitude measurements were made was approximately 0.5 seconds, which is the shortest measurement time allowed in the rheometer software.

The growth of shear modulus after cessation of the pre-shear approximately follows a modified exponential recovery curve as suggested by Rueb and Zukoski [134]

$$G'(t) = (G'_\infty - G'_0)[1 - \exp(-\alpha t)] + G'_0 \qquad (3.3)$$

where G'(t) is the time varying elastic modulus measured after cessation of the preshear, $G'_0$ is the instantaneous modulus recorded at time t=0, and $\alpha$ is a decay constant. Note that Rueb and Zukoski measured shear moduli on silica particles with adsorbed octadecyl chains that were on the order of $10^2$ Pa, but the gels used here are considerably stronger with moduli approaching $10^6$ Pa in magnitude. Table 3.1 shows the results of a weighted least squares regression analysis used to evaluate the three parameters $G'_0$, $G'_\infty$ and $\alpha$ for the case of the varying concentration of $PEI_{100K}$. These have been shown as solid lines in Figure 3.10. Table 3.2 shows the parameters fitted to the case of varying $M_w$ of the PEI used. These have been shown as solid lines in Figure 3.11. A time weighted regression was used to allow for a better representation of data collected nearer to cessation of pre-shear.

| Wt% PEI→ | 0.008% | 0.016% | 0.025% |
|---|---|---|---|
| G'∞ (kPa) | 0.34 | 19.9 | 433 |
| G'0 (kPa) | 0.13 | 2.9 | 12.4 |
| G'0/G'∞ | 0.38 | 0.14 | 0.03 |
| $\alpha$ ($s^{-1}$) $\times 10^3$ | 1.28 | 0.58 | 0.13 |

Table 3.1 Model parameters for $\Phi$ =0.49 $BaTiO_3$ gels flocculated using $PEI_{100K}$

| PEI $M_w$→ | $PEI_{2K}$ | $PEI_{25K}$ | $PEI_{100K}$ |
|---|---|---|---|
| $G'_\infty$ (kPa) | 7.7 | 250 | 433 |
| $G'_0$ (kPa) | 1.6 | 13.4 | 12.4 |
| $G'_0/G'_\infty$ | 0.20 | 0.05 | 0.03 |
| $\alpha$ ($s^{-1}$) $\times 10^3$ | 0.39 | 0.48 | 0.13 |

Table 3.2 Model parameters for $\phi$=0.49 $BaTiO_3$ gels flocculated using 0.025wt% of $PEI_{100K}$, $PEI_{25K}$ and $PEI_{2K}$

As the concentration of $PEI_{100K}$ was increased in the barium titanate suspension, an exponential increase in the parameters $G'_0$ and $G'_\infty$ was observed. For comparison of the three gels measured in this experiment, the ratio of $G'_o$ to $G'_\infty$ for each was calculated. The clear trend is that while the magnitude of $G'_0$ increased with $PEI_{100K}$ concentration (i.e., gel strength), the fraction of the equilibrium modulus observed after cessation of the pre-shear period decreases for increasing $PEI_{100K}$ concentration. The $G'_0/G'_\infty$ ratio varied from ~40% for the weakest gel, to ~14% for the intermediate gel and 3% for the strongest

gel. This trend reflects the state of the gel structure during and immediately after pre-shear. For strong gels, the yield strain is of the order $10^{-4}$ and can be considered more "brittle" than the weaker gels that yield at strains of the order $10^{-3}$. Thus, while each gel experienced the same shear history, the weaker gels were closer to their equilibrium structure at t=0s. Similar observations could be made for gels of constant PEI concentration but different molecular weight. The $G'_0/G'_\infty$ decreased with increasing rigidity of the gels i.e. approximately 20% for the $PEI_{2K}$ flocculated gel as compared to 3%-5% for the more rigid $PEI_{25K}$ and $PEI_{100K}$ flocculated gels.

The decay constants tabulated in Table 3.1 showed a decrease from a value of $10^{-3}$ $s^{-1}$ to $10^{-4}$ $s^{-1}$ from the weakest to the strongest gel. The decay constant is characteristic of the rate at which the disrupted gel structure returns to the unperturbed or equilibrium state as inter-particle bonds that were ruptured during the pre-shear period are re-formed. For weak gels, modulus recovery occurs more rapidly than for strong gels due to the relatively more compliant gel structure and the potential for more rapid structural rearrangement.

There are two general conclusions to be drawn from the observed modulus recovery experiments: (1) the magnitudes of $G'_\infty$ and $G'_0$ are larger for stronger gels and (2) both $G'_0/G'_\infty$ and $\alpha$ decrease with increasing gel strength ($G'_\infty$). These behaviors indicate that stronger gels undergo an instantaneous rearrangement of structure on cessation of pre-shear and then slowly regain their final shear modulus as the structure rearranges at a slower pace. The instantaneous recovery is high in magnitude but a smaller portion of the final equilibrium modulus when compared to weaker gels, which showed a greater instantaneous fractional recovery in modulus and a more rapid return to

quiescent equilibrium properties after the initial step change in modulus. Despite the more rapid gel strength recovery of weak gels, it is the higher magnitude initial modulus of strong gels that supports the spanning structures assembled in the robocasting process.

### *3.3.4. Robocasting of barium titanate inks*

To demonstrate the suitability of the barium titanate gels in the robocasting process, several spanning lattices were assembled from gels flocculated with $PEI_{100K}$ using deposition nozzles ranging from 100 microns to 500 microns. Figure 3.13(a) shows a three dimensional periodic structure consisting of alternate layers of radial and circular rods deposited using a 200 micron deposition nozzle. Figure 3.13(b) shows a simple tetragonal lattice consisting of alternating layers of parallel rods offset by $90^{o}$ from each other. Figure 3.13(c) demonstrates the capability of the process to repeatedly deposit thin rods and this deposition was carried out using a 100 micron deposition nozzle. Depositions down to 100 microns were carried out with ease using the micron sized barium titanate inks but below 100 microns, deposition led to clogging due to the high ratio of the particles size to the nozzle diameter (~1:100). Figure 3.13(d) demonstrates the overlap joint between layers of rods in the lattice structures. It was observed that grain growth occurred between rods on consecutive layers.

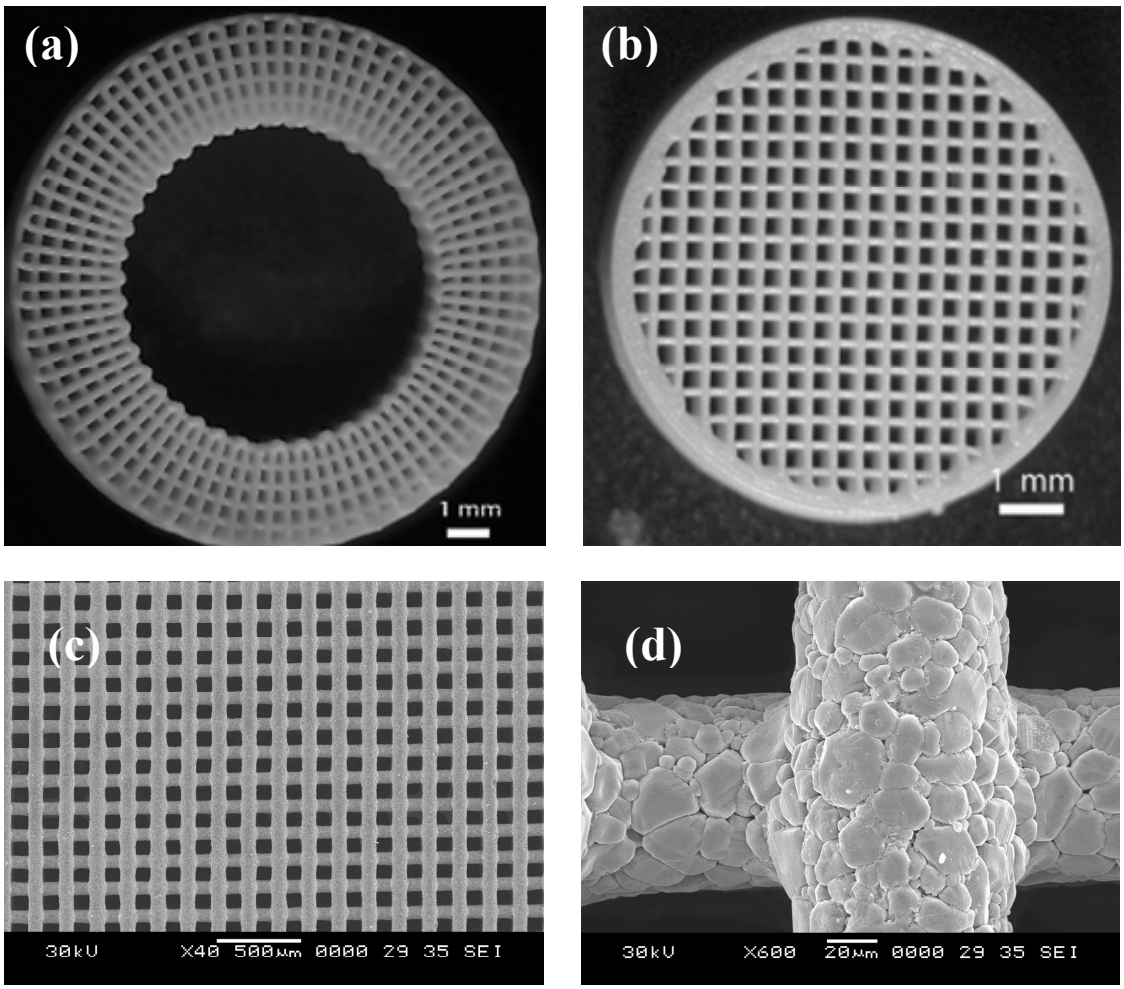


Figure 3.13 Sintered $BaTiO_3$ structures - optical images of (a) radial lattice and (b) linear lattice, SEM images of (c) fine scale, linear lattice and (d) an intersection of two lattice rods.

In all cases the deposited filaments had to span underlying gaps. Stresses arising from the weight of the deposited filaments would tend to create sag in the deposited lines[9]. Due to the high magnitude of the elastic modulus and the yield stress, the rods maintained their circular cross section and spanned underlying gaps with minimum deflection.

### 3.4.Conclusions

Micron sized barium titanate particles were used in an extrusion based robotic deposition process to fabricate 3-D periodic structures. Concentrated colloidal inks were created via flocculation of dispersed slurries using two different mechanism which altered the inter-particle potential of the particles. In the case of flocculation by cations, it was observed that along with screening there was also a bridging effect in the case of divalent cations aiding in the flocculation and increasing elasticity of the gels. In the case of polyelectrolyte flocculation it was observed that the molecular weight of the flocculating agent played an important role in formulating inks with desirable visco-elastic properties. Both the cationic and polyelectrolyte flocculation were comparable and yielded gels suitable for the robocasting process. Dynamic observation of gel properties revealed a variation in gel recovery kinetics that were slower for stronger gels indicating that structural rearrangement is inhibited by a more rigid gel structure. Despite the slower recovery kinetics, stronger gels possess a higher magnitude initial modulus after cessation of pre-shear and were found to recover fast enough to enable the assembly of 3-D periodic $BaTiO_3$ structures.

SECTION II: COLLOIDAL PROCESSING OF BARIUM TITANATE, STRONTIUM TITANATE AND BARIUM ZIRCONATE INK MIXTURES FOR DIRECT WRITE

## 3.5.Introduction

Ceramic ink mixtures consisting of aqueous dispersions of barium titanate, strontium titanate and barium zirconate mixed in various molar ratios were formulated for the robocasting process. Mixtures of the three ceramic powders were found to have similar dispersion-flocculation characteristics as the barium titanate inks and this aided in co-dispersion and co-flocculation for fabrication. Ceramic powder mixtures were dispersed in aqueous media using ammonium polyacrylate as a dispersing agent. Gellation was induced using $PEI_{100K}$ based on the results from Section I. Gels thus obtained were cast into various 3-D patterns to prove the efficacy of the ink design.

## 3.6.Experimental section

### *3.6.1. Materials System*

Ceramic powders of barium titanate (Ticon HPB, Ferro Electronics Corporation, Penn Yan, NY) strontium titanate (Ticon 55, Ferro Electronics Corporation, Penn Yan, NY) and barium zirconate (Barium zirconate 119, Ferro Electronics Corporation, Penn Yan, NY) all with an average particle size ~ 1 μm and density of 6.02, 4.5 and 5.5 $g/cm^3$ served as the ceramic phases respectively.

### *3.6.2. Colloidal gel preparation*

Concentrated ceramic suspensions (45-50 volume%) were created by adding a pre-determined amount (0.6 wt% based on total particle weight) of ammonium salt of poly(acrylic acid) (APA) (Darvan 821A, R.T. Vanderbilt Co., Norwalk, CT) to de-ionized water in a 100 ml HDPE bottle (Nalge Nunc Intl., Rochester, NY). Ceramic powders in the appropriate molar ratios were then added to the water and vigorously mixed using a table top mixer. This generated a low viscosity ceramic slurry to which 5% aqueous solution of HPMC powder (Hydroxypropyl methylcellulose (HPMC) (Methocel F4M, Dow Chemical Co., Midland, MI.) with a molecular weight of 3500 was added (as an aid to prevent stress induced particle migration) to obtain a viscosifier concentration of 5 mg/ml of the fluid phase. A few drops of non-linear poly (ethylenimine) (PEI), $M_w$=50,000-100,000 (ICN Biomedical, Aurora, OH) ($PEI_{100K}$) was added to this slurry to generate aqueous gels with controlled elasticity and yield stress.

### *3.6.3. Rheological Characterization*

The rheological behavior of the inks was characterized using a controlled stress-strain rheometer (Model CVOR 200, Bohlin Instruments, East Brunswick, NJ). To prevent wall slip a cup and bob geometry (C14, cup I.D. =16 mm and bob O.D. = 14 mm) with serrated walls was used. Further, to prevent sample evaporation during the long periods required for measurements, the measuring geometry was fitted with a custom made solvent trap. Each measurement required a sample size of 3.8 ml which was loaded into the cell using a plastic syringe.

For each measurement of elastic modulus, a pre-shear of $1s^{-1}$ was applied for a period of 60 seconds to the loaded sample. Then, the sample was left undisturbed for an hour to attain an equilibrium state. Next, the rheometer applied a logarithmically increasing oscillatory shear to the sample. Each measurement was made over 10 oscillations and a wait time of 30 seconds was allowed between consecutive measurements to minimize the influence of the previous measurement. The shear stress range probed was varied accordingly to ensure collection of data in the linear visco-elastic region (LVER) and the shear yield stress ($\tau_y$) for varying gel strengths.

### *3.6.4. Fabrication of 3-D structures using ceramic inks*

Diverse three-dimensional periodic structures were fabricated to demonstrate the suitability of these newly formulated inks for use in the robotic deposition process. An extrusion based robotic deposition device (Aerotech Inc., Pittsburg, PA) with custom written control software was used as the direct write tool. Ceramic inks were housed in syringes (1ml or 3ml, BD Inc., NJ) equipped with blunted stainless steel tips of various ID (EFD Inc., East Providence, RI). The deposition process was carried out on a flat substrate submerged in an oil bath to prevent drying of the colloidal ink during deposition. After the deposition step was completed the oil was drained and the structures were dried in ambient air for a minimum of 12 hours and then sintered in an electric furnace (Model LHT 02/17, Nabertherm, Germany) on zirconia setter plates. A sintering schedule of 25$^{o}$C -1450$^{o}$C (2.8$^{o}$C/min), 1450$^{o}$C (60 min), and 1450$^{o}$C -25 $^{o}$C (4.4 $^{o}$C/min) was followed.

## 3.7.Results and discussions

### *3.7.1. Gel rheology of formulated inks*

Gels for the robocasting process must satisfy two important criteria[9, 10]

- Gels must flow through fine nozzles as small as 100 microns in diameter
- Gels must immediately recover structure on deposition and maintain shape to allow for overlying layers to be deposited over them

To evaluate the effect of having a three different particle systems (BT, ST, BZ) instead of BT alone in the ink, the rheology of 4 unique gels of barium titanate, strontium titanate, barium zirconate and a 1:1:1 molar ratio of the three ceramics was measured using both steady state and dynamic measurements and has been discussed in detail in Section 4.3.1. In the case of the steady state measurements all gels displayed similar shear thinning rheology that followed a Herschel Bulkley model (shear thinning with yield stress). The shear thinning behavior allowed for the gels to have amenable flow properties making it possible to extrude through fine nozzles under modest pressure drops without filter pressing. Shear modulus measurements revealed that all gels had a high elastic modulus ($>10^5$) and also a corresponding high yield stress (>100Pa). The high shear modulus made the fabrication of spanning structures with minimum deflection possible and the high yield stress allows for important shape retention behavior by the gels. Hence, the tailored rheological behavior of the gels permitted fabrication of complex and simple 3-D patterns such as space filled solids, spanning elements and high aspect ratio walls.

### *3.7.2. Gelation by bridging flocculation with cationic polyelectrolyte*

Akin to the gelation mechanism discussed in detail in section I, gels containing a mixture of BT, ST, and BZ were found to be suitable for robocasting based on both rheological measurements and actual fabrication. It is expected that when the mixture of ceramic powders were added to a solution containing the APA, the ionized APA molecules were adsorbed at positive sites on the particle surfaces to promote stabilization. Addition of the $PEI_{100K}$ resulted in a complexation mechanism whereby the positive amine sites on the $PEI_{100K}$ molecule could act as bridging agents between APA molecules on the same particle or across different particles promoting bridging flocculation and an increase in the gel strength. Inks thus formed could be cast into 3-D structures as described in the next section.

### *3.7.3. Robocasting of ceramic mixtures inks*

To demonstrate the suitability of the multi-ceramic mixture gels in the robocasting process, several spanning structures were assembled from gels flocculated with $PEI_{100K}$ using deposition nozzles ranging from 100 microns to 500 microns. Figure 3.14 shows several examples structures made using inks composed of barium titanate, strontium titanate and barium zirconate in three unique molar ratios. In other experiments varying molar ratios were tried and gels were found to be amenable for casting independent of the molar ratios used.

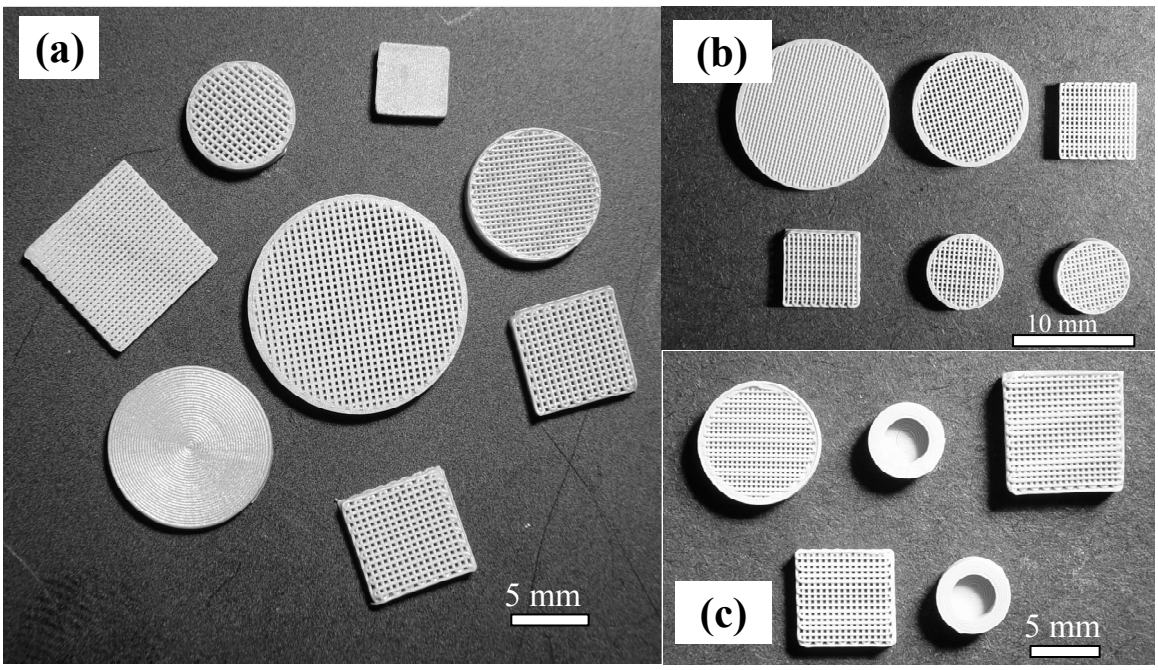


Figure 3.14 Various three–dimensional patterns printed using inks with varying barium titanate: strontium titanate: barium zirconate molar ratio; (a) 2:1:1, (b) 1:2:1, (c) 1:1:2

### 3.8.Conclusions

Inks for the robocasting process containing mixtures of barium titanate, strontium titanate and barium zirconate ceramic powders mixed in varying molar ratios were developed. The ability to fabricate 3-D periodic structures showed that the dispersion-flocculation mechanism of using APA-$PEI_{100K}$ was suitable to develop robust inks which could print 3-D structures utilizing a range of nozzle diameters.

# 4. DIELECTRIC PROPERTIES OF BARIUM TITANATE: STRONTIUM TITANATE: BARIUM ZIRCONATE MIXTURES

## 4.1.Introduction

Barium strontium titanate ($Ba_xSr_{1-x}TiO_3$) or BST is a promising ceramic for applications such as ferroelectric random access memories (FRAMs),[90-98, 135-137] phase array antennas,[99-103] decoupling capacitors,[104-107] filter capacitors,[108] and opto-electronics due to a high dielectric constant, low dielectric loss and high electro-optic tunability. Within the perovskite lattice, $Sr^{2+}$ substitutes for $Ba^{2+}$ and results in a decrease in the Curie temperature and increased electro-optic tunability. While high tunability is desirable in many applications, the increased dielectric constant and an accompanying increase in loss tangent is often tempered by mixing with a low permittivity material such as MgO or $MgTiO_3$.[112, 113] The low permittivity ceramic $BaZrO_3$ (K=30) may also be used to lower the dielectric constant;[138] however, substitution of $Zr^{4+}$ on the $Ti^{4+}$ sites in the $BaTiO_3$ lattice may yield unexpected results due to shifts in the Curie temperature of the solid solution. For pure barium titanate, the Curie temperature is ~130$^oC$, but as the concentrations of $Sr^{2+}$ or $Zr^{4+}$ increases, the Curie temperature may approach or plunge below ambient temperatures.

Here, the dielectric properties of ternary mixtures of $BaTiO_3$ (BT), $SrTiO_3$ (ST), and $BaZrO_3$ (BZ) were explored as a function of composition, temperature, and applied

electric field bias. Using commercially available BT, ST, BZ powders, colloidal inks were prepared for use in robocasting.[9, 10, 65] The ability for a solid state reaction to occur during co-sintering of these BT, ST and BZ particles is well-known,[138] but there is an absence of detailed characterization of the ternary mixtures of the BT, ST and BZ perovskite mixtures. Here, we highlight the utility of direct write processing to fabricate flat plate samples with varying composition across the ternary phase space. For complete details about robocasting, the reader is referred to Chapter 3. Developing the processing route and determining the electrical characteristics of these compositions provides for a rapid prototyping approach to casting these samples into useful 3-D functional patterns (e.g., fabrication of photonic crystals as discussed in chapter 5). In this chapter however, the focus was mainly to develop a properties map of the dielectric behavior for these compositions to estimate properties suitable for fabrication of photonic crystals with or without tunability.

## 4.2.Experimental methods

### *4.2.1. Materials System*

Barium titanate (Ticon HPB, Ferro Electronics Corporation, Penn Yan, NY), strontium titanate (Ticon 55, Ferro Electronics Corporation, Penn Yan, NY) and barium zirconate (Barium zirconate 119, Ferro Electronics Corporation, Penn Yan, NY), all with an average particle size ~ 1 μm and density of 6.02, 4.5 and 5.5 g/cm$^3$ respectively, served as the ceramic phases. An ammonium salt of poly(acrylic acid) (APA) (Darvan 821A, R.T. Vanderbilt Co., Norwalk, CT) was used as an aqueous dispersant. Hydroxypropyl methylcellulose (HPMC) (Methocel F4M, Dow Chemical Co., Midland,

MI.) with a molecular weight of 3500 was used as a viscosifier. Non-linear poly(ethylenimine) (PEI), $M_w$=50,000-100,000 (ICN Biomedical, Aurora, OH) ($PEI_{100K}$) was used as a flocculant.

### *4.2.2. Colloidal gel preparation*

Concentrated ceramic suspensions (45-50 volume%) were created by adding a predetermined amount (0.6 wt% based on total particle weight) of APA to de-ionized water in a 100 ml HDPE bottle (Nalge Nunc Intl., Rochester, NY). Ceramic powders in the appropriate molar ratios were then added to the water and vigorously mixed using a table top mixer (AR 250, THINKY corp., Tokyo, Japan). A 5% aqueous stock solution of HPMC powder was added to the slurry to obtain a viscosifier concentration of 7 mg/ml within the solvent phase. PEI was added to gel the slurry and control elastic modulus and yield stress. Detailed descriptions of colloidal gel preparation and their rheological characteristics are provided in a previous publication.[65]

### *4.2.3. Direct writing of flat plates for testing using robocasting*

A 4X4 array of flat plates, each measuring 10mm×10mm×1.2mm, was assembled by direct write processing for each composition tested. The gantry robot (Aerotech Inc., Pittsburg, PA), as displayed in Figure 4.1, was programmed with custom control software. Ceramic inks were housed in syringes (1ml or 3ml, BD Inc., NJ) equipped with blunted stainless steel tips of 0.33 mm inside diameter (EFD Inc., East Providence, RI).

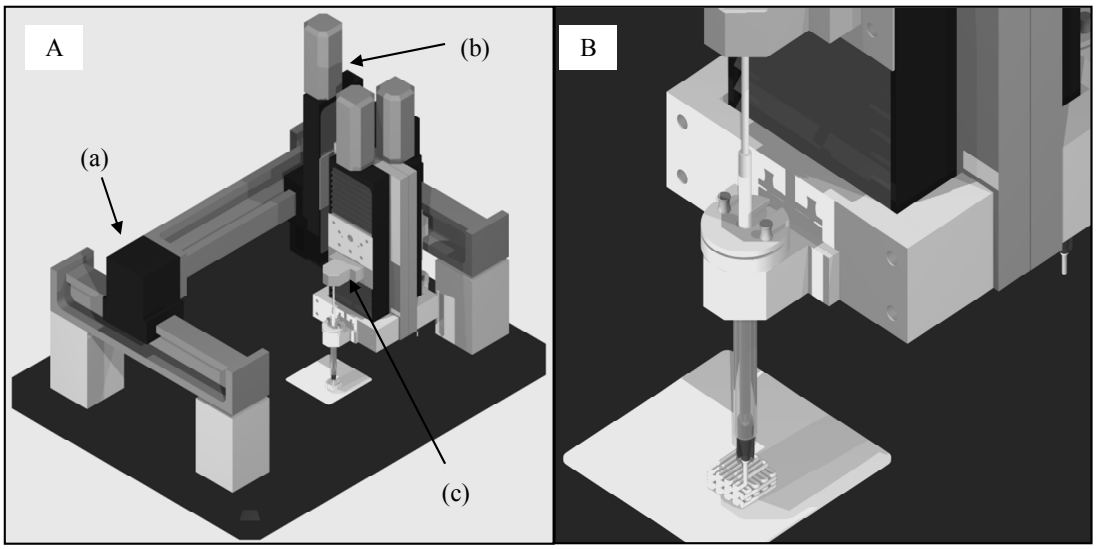


Figure 4.1 A schematic of the robocasting tool showing A: An overview with (a) the x-y gantry system, (b) the z stage, (c) the syringe pump, and B: Close-up of the actual deposition process showing a pattern build in progress

The deposition process was carried out on a flat alumina substrate submerged in an oil bath to prevent drying of the colloidal ink during deposition. After the deposition step was completed, the oil was drained and the structures were dried in ambient air for a minimum of 12 hours, detached from the substrate, and then sintered in an electric furnace (Model LHT 02/17, Nabertherm, Germany) on zirconia setter plates. All sintering schedules included a ramp rate of 2.8$^{o}$C/min, a hold at the soak temperature for 1 hour and a ramp down rate at 4.5$^{o}$C/min. The sintering temperature was adjusted according to composition. For composites consisting of only BT and ST, a soak temperature of 1340$^{o}$C was used. When the composite included BZ a soak temperature of 1500$^{o}$C was used to account for the refractory nature of the BZ.

### *4.2.4. Rheological Characterization*

Ink design is crucial to the robocasting process. A formulated ink possessing a low yield stress and low elasticity will not have the shape retention properties important for fabricating 3-D patterns. On the other hand, ink that possesses extremely a high yield stress will experience a large pressure drop during extrusion which may leads to filter pressing due to phase separation.[65] The rheological behavior of the inks was characterized using a controlled stress-strain rheometer (Model CVOR 200, Bohlin Instruments, East Brunswick, NJ). To prevent wall slip, a cup and bob geometry (C14, cup I.D. =16 mm and bob O.D. = 14mm) with serrated walls was used. Further, to prevent sample evaporation during the long periods required for measurements, the measuring geometry was fitted with a custom made solvent trap. Each measurement required a sample size of 3.8 ml which was loaded into the cell using a plastic syringe.

For each measurement of elastic modulus, a continuous pre-shear of $1s^{-1}$ was applied for a period of 60 seconds to the loaded sample. Then, the sample was left undisturbed for an hour to attain an equilibrium state. Next, the rheometer applied a logarithmically increasing oscillatory shear stress to the sample. Each measurement was made over 10 oscillations and a wait time of 30 seconds was allowed between consecutive measurements to minimize the influence of the previous measurement. The shear stress range probed was varied accordingly to ensure collection of data in the linear visco-elastic region (LVER) and the shear yield stress ($\tau_y$) for varying gel strengths. For measurement of the viscosity of the gels, a similar pre-treatment was applied. After attaining equilibrium the gels were subjected to steps of increasing shear rates. For each

shear rate an equilibrium time of 1 minute was used before measuring the shear stress required to maintain the shear rate.

### *4.2.5. X-ray diffraction measurement*

X ray diffraction patterns were recorded on a Bruker AXF D-8 advanced x-ray powder diffractometer using Cu K-α radiation. Multiple small samples (approximately 50 each), having a cylindrical geometry of diameter d=1 mm and height of h= 1mm, were printed, and sintered similar to the samples fabricated for dielectric measurements. These were then packed into the sample holder and scans were conducted for $20^{\circ}<2\theta<70^{\circ}$ for a period of 12 hours each. Patterns were compared against those from the International Center for Diffraction Database (ICDD).

### *4.2.6. Dielectric characterization*

Radio frequency (RF) sputtering was used to deposit Cr (~10nm, 1:45 min)/Au (~100nm, 3:00 min) electrodes on both surfaces of each sample to be measured. The sides of the sample were then polished with a 600 grit sandpaper to remove the coating and prevent shorting. Temperature dependent impedance (capacitance measurements) with no bias, were conducted on all samples. An impedance analyzer (HP4284A, Agilent Technologies, Palo Alto, CA) was used in connection with a chiller and a furnace. An approximate temperature range of $-50^{o}$C to $150^{o}$C was probed.

Tunability measurements were taken at room temperature by applying a D.C. bias using a high voltage power supply (PS310, 1250V max, Stanford Research Systems, Sunnyvale, CA) with an in-house built protection circuit between the PS310 and HP 4284A. This allowed for the application of high voltage necessary to tune the bulk samples without

damaging the HP 4284A. A 0.05 V AC ripple bias and a frequency of 1 KHz were used for the tunability measurements. This was done to prevent drift in the capacitances which was observed when the bias was initially applied. A wait time of ~2min was used before recording the change in capacitance.

## 4.3.Results

### *4.3.1. Gel rheology of formulated inks*

Gels for the robocasting process must satisfy two important criteria. They must be able to flow through nozzles as fine as 100 μm in diameter without filter pressing but should also rapidly recover structure on deposition and maintain shape to allow for overlying layers to be deposited. The formulation of barium titanate inks for robocasting has been described in detail in a previous publication[65] and Chapter 3. It was hypothesized that a mono-layer coverage of negatively charged poly(acrylic) acid chains ($PAA^-$) on the ceramic particle surface acted as a dispersant allowing for the formulation of a high solids loading slurry. Next, the low viscosity slurry was flocculated by adding a small amount of a cationic polyelectrolyte-$PEI_{100K}$. The positively charged PEI molecules had a dual effect-(a) screening of charge on the dispersant molecules, and (b) an inter-particle bridging effect leading to gelation and a subsequent increase in yield stresses and shear moduli.

It was found that BT, ST, BZ, and mixtures of these three particle systems could be dispersed and flocculated in a similar way using the dual polyelectrolyte approach. This could be attributed to the presence of positively charged sites on the particle surfaces of ST and BZ which helped to adsorb a monolayer coverage of anionic $PAA^-$ chains

similar to the BT surface. When a dispersant is added to a mixture of ceramic particles (as in the case of a mixture of BT, ST, and BZ) it is expected that distribution of dispersant occurs based on the charge distribution across various particle surfaces. It was observed that approximately similar concentrations of APA were sufficient to disperse individual suspensions for the other two systems, ST and BZ. Further, addition of $PEI_{100K}$ also flocculated the single component inks yielding gels suitable for the robocasting process. A mixture of the ceramic particles in various molar ratios could also be dispersed-flocculated with the dual polyelectrolyte scheme and yielded castable gels as described below.

The rheology of 4 unique inks of barium titanate, strontium titanate, barium zirconate and a 1:1:1 molar ratio (as a representative for ceramic mixture inks) of the three ceramics was measured using both dynamic (Figure 4.2) and steady state measurements (Figure 4.3). Shear modulus measurements revealed that the inks had a high elastic modulus ($>10^5$) and also a corresponding high yield stress (>100Pa). Among the inks, the BT ink showed the greatest degree of gelation with $G'_{eq}$~900 KPa and a yield stress = 280 Pa. The ST and BZ inks showed lower modulus and yield stress values at approximately 200 KPa and 120 Pa respectively. The mixture ink, composed of premixed particles of BT, ST, and BZ blended in a 1:1:1 molar ratio, showed an intermediate modulus very close to the ST and BZ gels. The high shear modulus makes the fabrication of spanning structures with minimum deflection possible[9] and the high yield stress allows for important shape retention behavior by the gels. In the case of the steady state measurements all gels displayed characteristic Herschel-Bulkley behavior, characterized as having a yield stress accompanied by a shear thinning flow. The shear thinning

behavior allowed for the gels to have appropriate flow properties making it possible to flow through fine nozzles without filter pressing. Subsequently, the controlled rheological behavior of the gels allowed for fabrication of bulk films for electric evaluation and additionally provided robust formulations for making more complicated 3-D patterns.

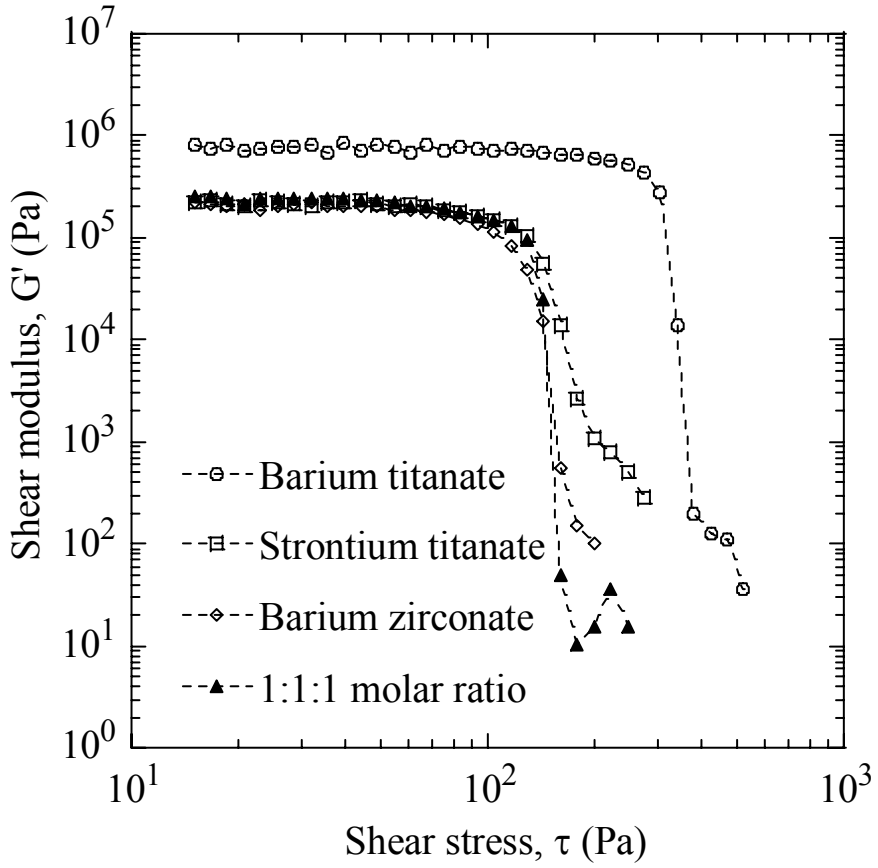


Figure 4.2 Rheology of single component gels as compared to a ternary mixture of the BT, ST, BZ in a molar ratio of 1:1:1 describing the shear modulus as a function of shear stress

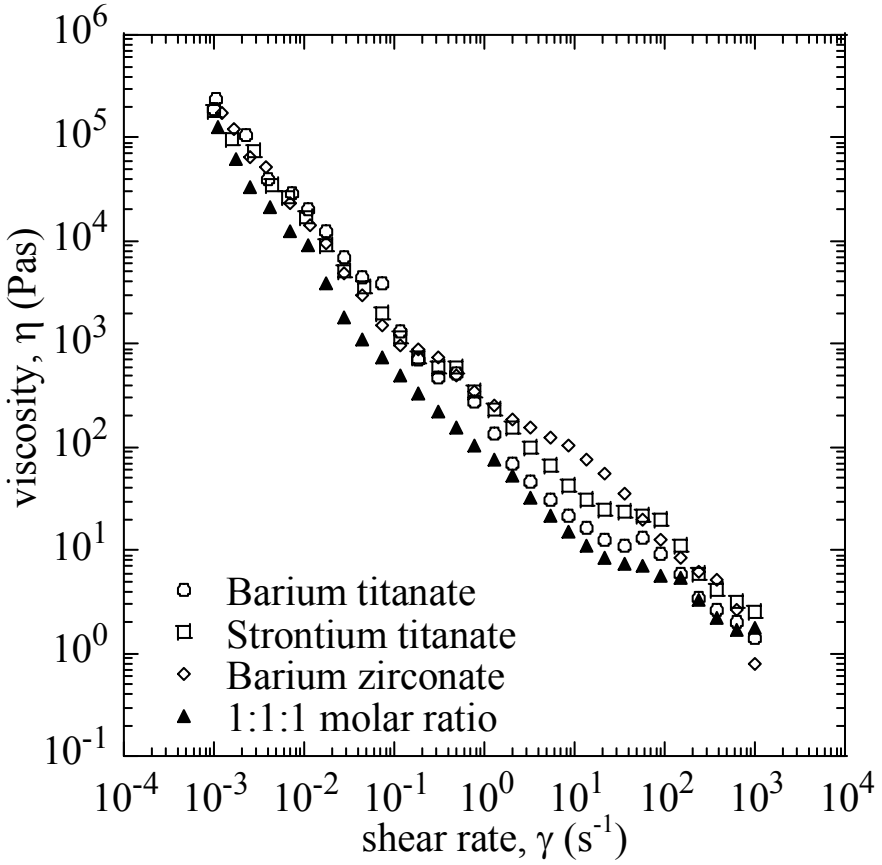


Figure 4.3 Rheology of single component gels as compared to a ternary mixture of the BT, ST, BZ in a molar ratio of 1:1:1 describing the viscosity as a function of shear rate

### *4.3.2. Dielectric characterization of compositional mixtures*

#### 4.3.2.1. X-Ray diffraction on ternary mixtures

X-ray diffraction was used to characterize the crystal structure of sintered BT-ST-BZ composites. Figure 4.4 shows the XRD patterns for three representative ternary compositions having BT: ST: BZ in molar ratio of 2:1:1, 1:2:1, and 1:1:2 respectively. The solubility of strontium titanate and barium zirconate with $BaTiO_3$ to the extent of

100% is well-known and was confirmed here.[138] Each diffraction pattern is characteristic of a single perovskite crystal structure and indicates that the three phases formed a solid solution at a sintering temperature of 1500°C. Compositions richer in $SrTiO_3$ displayed a shift of the (110) peaks to higher 2θ indicating a reduced unit cell size, while compositions rich in $BaZrO_3$showed a decreased 2θ shift of the (110) peaks compared to pure $BaTiO_3$.

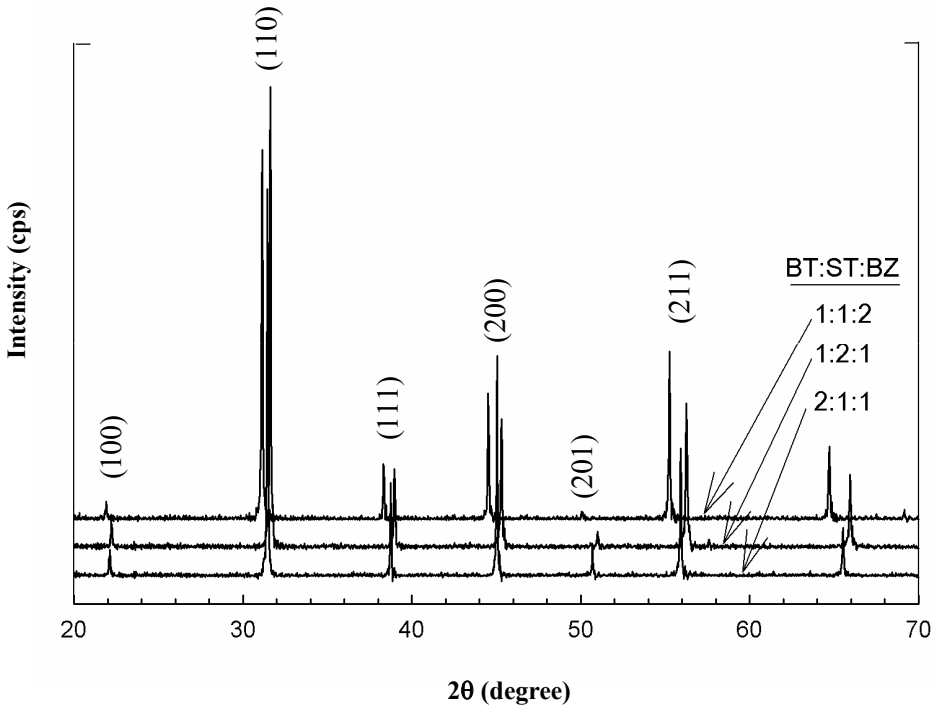


Figure 4.4 X-ray diffraction patterns for ceramic mixtures of BT:ST:BZ in the ratio 1:1:2, 1:2:1, and 2:1:1

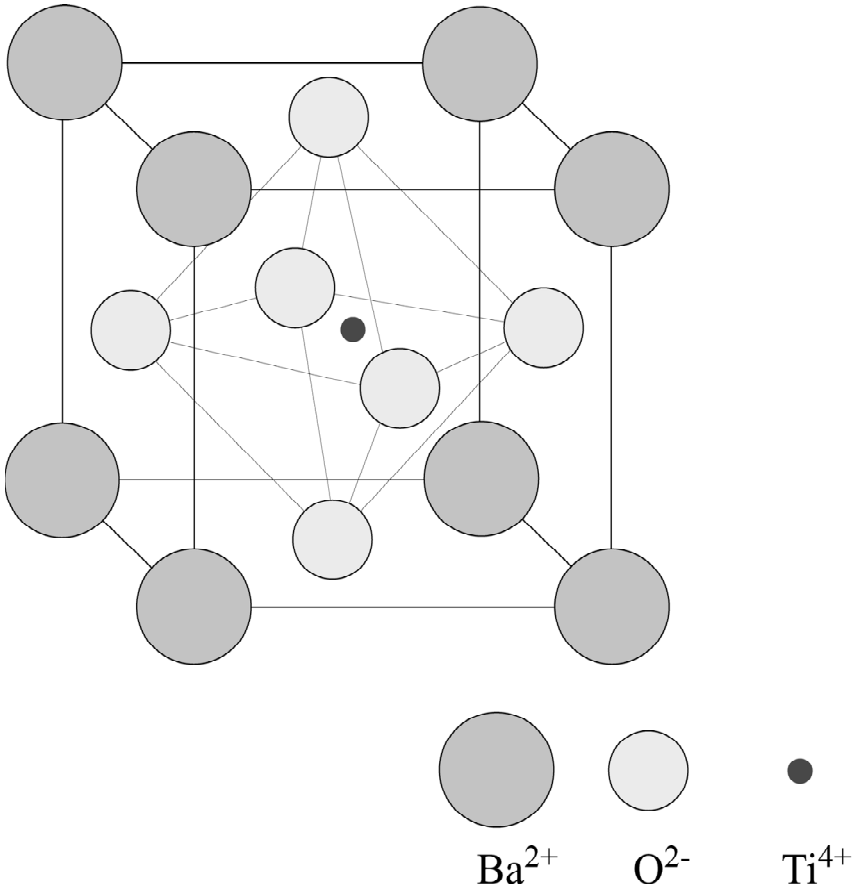


Figure 4.5 Perovskite crystal structure of barium titanate showing relative positions of the Ba, Ti and O ions in the cubic cell.

Within the barium titanate lattice (usually represented as $ABO_3$), Figure 4.5, A and B-position substitutions may take place with the formation of solid solutions of barium titanate with compounds having iso-valent cations of comparable sizes.[138] Thus $Sr^{2+}$ may be substituted for the $Ba^{2+}$ and the $Zr^{4+}$ may be substituted for the $Ti^{4+}$ cation in the barium titanate lattice. This substitution results in a change in the lattice parameters due to the relative size difference between the original and the substituted ions. $Sr^{2+}$ substitutions are accompanied by a slight decrease in the unit cell volume, as revealed by

x-ray diffraction data, on account of the smaller size of the $Sr^{2+}$ cation when compared to the $Ba^{2+}$ cation[109, 139-141]($Sr^{2+}$= 118 pm , $Ba^{2+}$=135 pm). On the other hand $Zr^{4+}$ substitutions are accompanied by an increase in the unit cell volume, owing to the larger size of the $Zr^{4+}$ ion as compared to $Ti^{4+}$. The decrease or increase in unit cell dimensions is accompanied by a change in the transition temperature and a general decrease in the dielectric constants as described below.

4.3.2.2. Barium titanate-strontium titanate binary mixtures

The dielectric constant decreased monotonically for binary and ternary mixtures of BT, ST and BZ as the molar ratio of BT: ST or BT: BZ or BT: ST+BZ decreased. Figure 4.6 illustrates the shift in Curie Point as the ST: BT molar ratio is increased. For example, pure barium titanate exhibited a Curie Point at $T_C \approx 130^oC$ with a maximum dielectric constant of K≈8200, whereas a 1:1 molar ratio mixture showed a Curie Point at $T_C$=-25$^o$C with a maximum dielectric constant of K≈5700. Barium titanate rich compositions showed Curie Points within the temperature range of measurement and extremely high permittivities whereas strontium titanate rich mixtures did not display Curie Points within the temperature range measured. All mixtures displayed low losses within 1% except around the Curie Point.

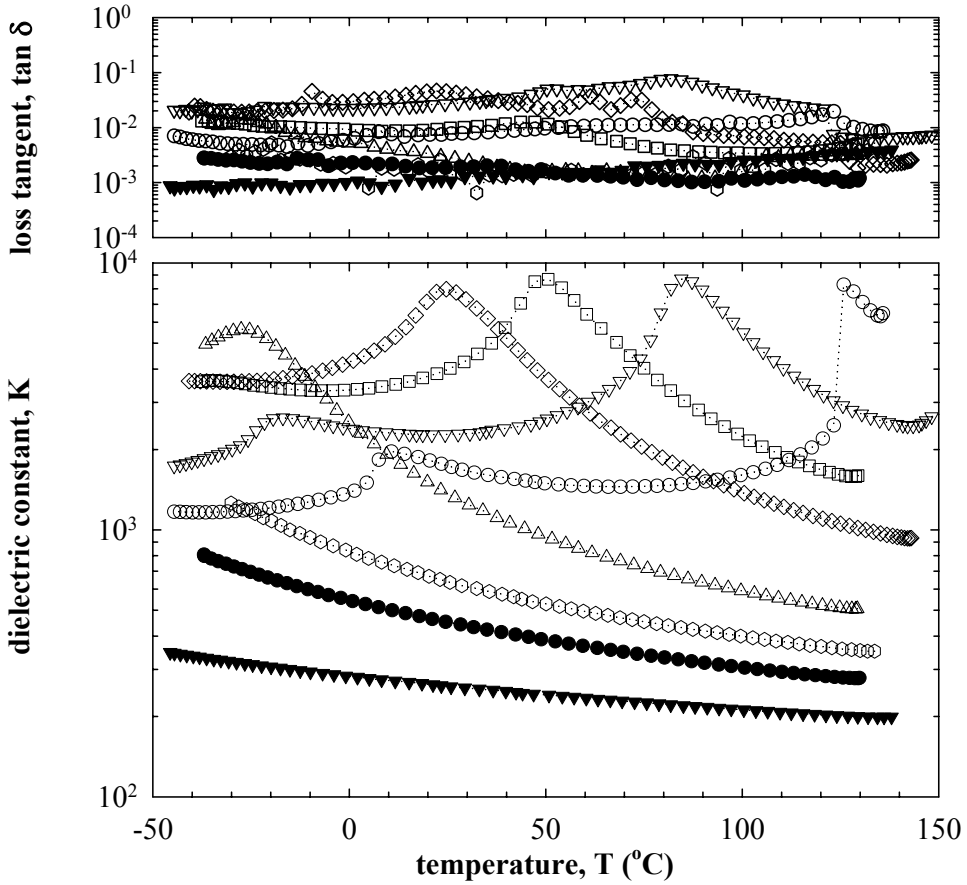


Figure 4.6 Dielectric constant and loss for a mixture consisting of BT: ST in proportion of 1:0 (○), 7:1 (▽), 3:1 (□), 2:1 (◇), 1:1 (△), 1:2 (⬭), 1:3 (●), and 0:1 (▼)

4.3.2.3. Barium titanate-barium zirconate binary mixtures

Figure 4.7 shows the dielectric characterization for BT:BZ mixtures as a function of measurement temperature and sample composition. The Curie Point displayed a shift from positive to negative temperature with a decrease in the BT: BZ molar ratio. A BT: BZ 7:1 mixture showed a dielectric constant peak of K≈26,000 at a temperature of 80°C accompanied by tan δ ≈0.30. Similarly the BT: BZ 3:1 composition showed a peak

dielectric constant of K≈22,000 at -15°C. With increased Zr concentration, the K peak became less sharp, indicating a switch from a type 1 to type 2 phase transformation.[11, 142-144] Other compositions did not display a K maxima in the temperature range measured. The greater stability of $Zr^{4+}$ acting as a B site substituent [11, 110, 111, 142, 143, 145] accounts for the decrease in the transition temperature. The $Ti^{4+}$ ion has a radius of 60.5 pm whereas the $Zr^{4+}$ has a 72 pm radius, which causes a decrease in the dipole moment of the unit cell and limits the range of movement of the B-site cation within the cell.[110, 146] Indeed, at high BZ concentrations the BT: BZ mixture should transition from ferroelectric to anti-ferroelectric behavior at room temperature.

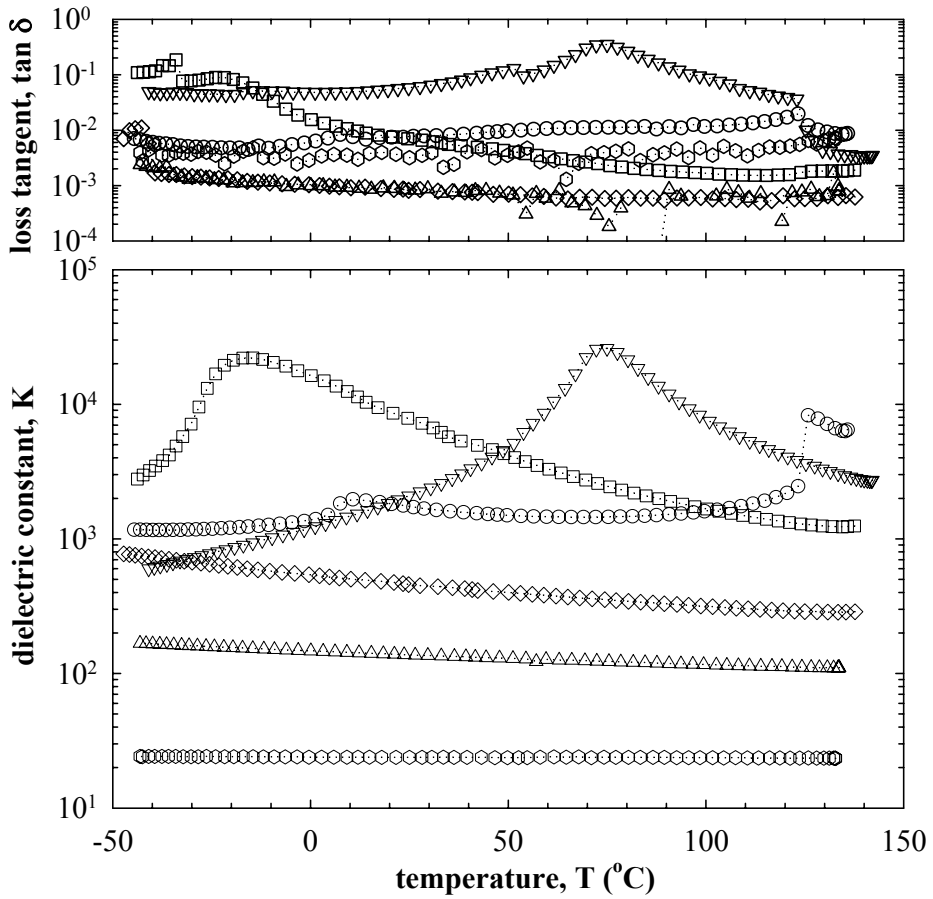


Figure 4.7 Dielectric constant and loss for a mixture consisting of BT: BZ in proportion of 1:0 (○), 7:1 (▽), 3:1 (□), 1:1 (◇), 1:3 (△), and 0:1 (⬡)

4.3.2.4. Strontium titanate-barium zirconate binary mixtures

Relatively flat dielectric profiles with decreasing temperatures were observed for the ST-BZ mixtures as shown in Figure 4.8. Due to the sintering of the ST: BZ mixtures at 1500°C, ST: BZ 3:1 and ST: BZ 1:1 mixtures showed higher dielectric constants than the pure ST phase. This is because pure ST ceramic was sintered at 1340°C whereas the ST: BZ mixtures were sintered at 1500°C to account for the refractory nature of barium

zirconate. A ST: BZ 3:1 showed a dielectric constant of 450 at 25°C with a low loss tangent of 0.002.

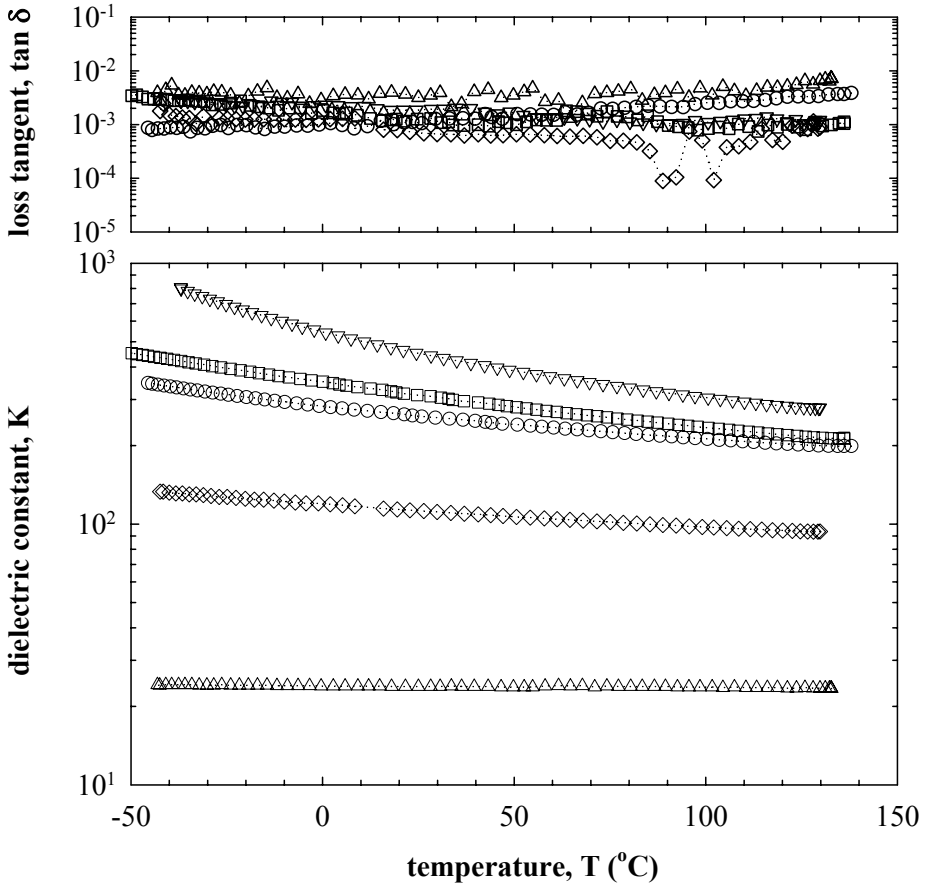


Figure 4.8 Dielectric constant and loss for a mixture consisting of ST: BZ in proportion of 1:0 (○), 3:1 (▽), 1:1 (□), 1:3 (◇), 0:1 (△)

4.3.2.5. Barium titanate-strontium titanate-barium zirconate ternary mixtures

For the ternary mixtures, BT, ST, and BZ were mixed in varying molar ratios and their dielectric properties were characterized and have been represented in Figure 4.9. The BT: ST: BZ 6:1:1 composition showed a phase transition at ~50$^{o}$C with a max dielectric constant of K≈29,000 with tan d = 0.12. The other compositions at BT: ST: BZ of 2:1:1, 1:2:1 and 1:1:1 showed decreasing dielectric constants as the $Ba^{2+}$ and $Ti^{4+}$ concentration in the mixture was decreased.

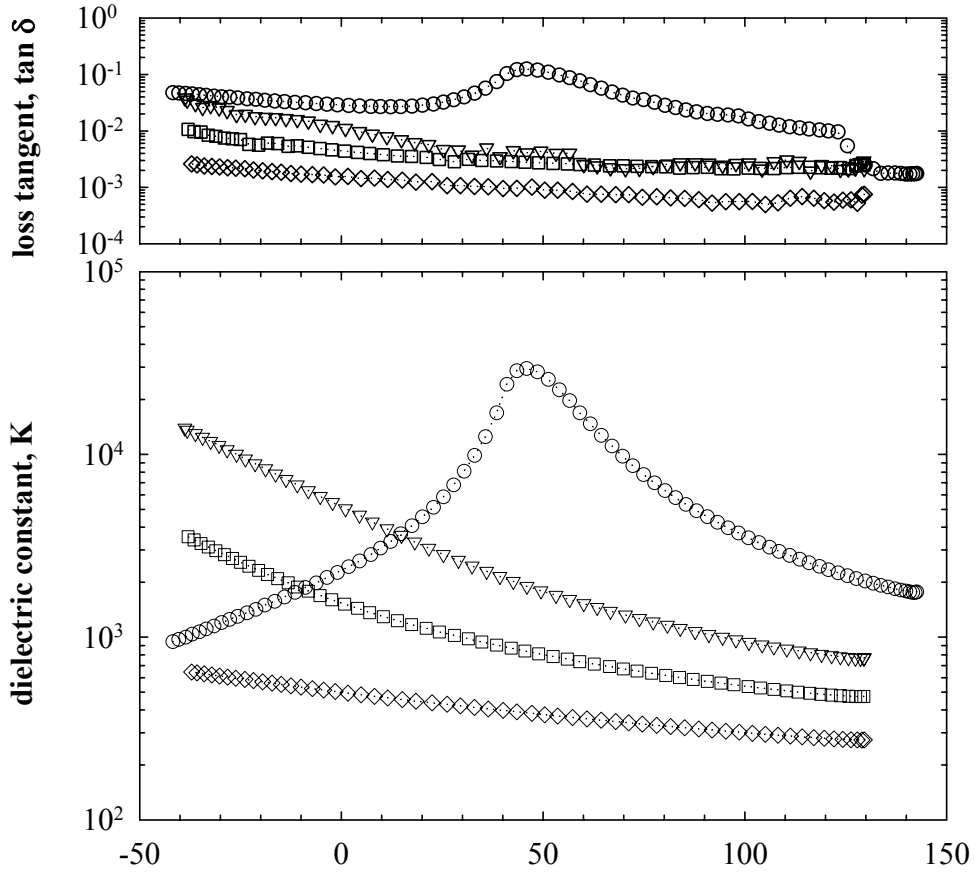


Figure 4.9 Dielectric constant and loss for a ternary mixture consisting of BT:ST:BZ in proportion of 6:1:1 (○), 2:1:1 (▽), 1:2:1 (□), 1:1:2 (◇)

#### 4.3.2.6. Ternary maps of dielectric properties

##### 4.3.2.6.1. Dielectric constant and loss

Figure 4.10 and 4.11 shows the dielectric constant and loss, respectively, plotted at room temperature (25°C) across the composition space of the ternary mixtures. For each ternary plot, the apexes represent 100% molar composition of BT, ST or BZ alone and these decrease with a subsequent increase in the molar ratio of the composition towards the next apex. Within the plot, some regions are ternary i.e. have some % moles of each dielectric component (BT, ST or BZ). The highest magnitudes of the dielectric constant seemed to be concentrated around the barium titanate apex and were found to decrease as the molar ratio of Sr: Ba and Zr: Ti was increased in the solid solution. Solid solutions of barium titanate containing less than 25% molar additions of strontium titanate and barium zirconate in any ratio showed higher permittivity than barium titanate alone. This could be attributed to measuring the dielectric function at a temperature where the permittivity was increasing rapidly as the Curie Point shifted towards lower temperatures.

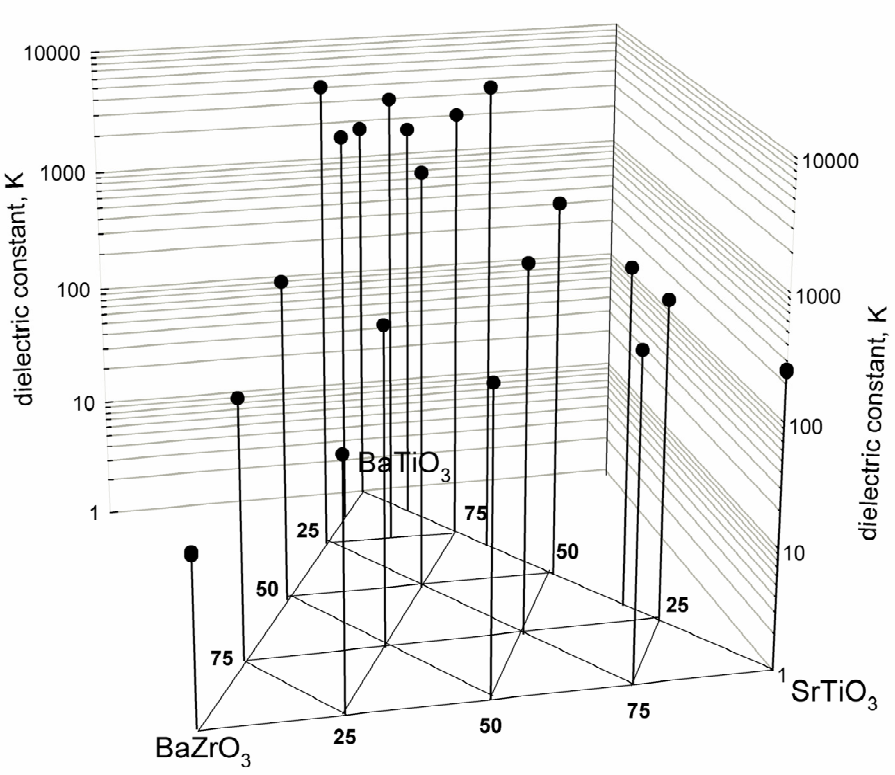


Figure 4.10 Properties of binary-ternary mixtures of BT, ST and BZ as a function of composition at 25°C: dielectric constant (100 KHz)

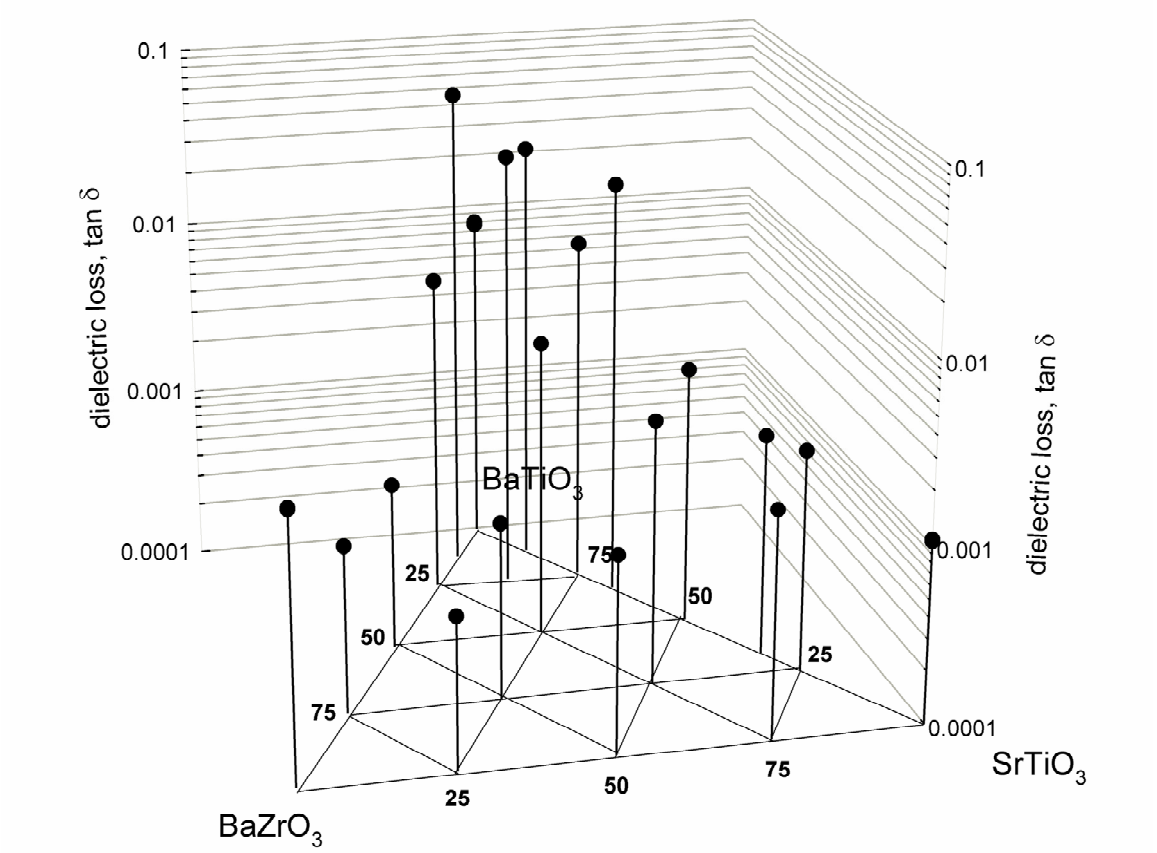


Figure 4.11 Properties of binary-ternary mixtures of BT, ST and BZ as a function of composition at 25°C: dielectric loss tangent (100 KHz)

Some models for the prediction of the dielectric constant based on a volumetric mixing model have been proposed for dielectric mixtures.[81] One such model is the logarithmic mixing rule give by:

$$\ln \varepsilon_m = \sum_i V_{fi} \varepsilon_i \qquad (4.1)$$

Where $\varepsilon_m$ is the relative permittivity of the mixture and $V_{fi}$ and $\varepsilon_i$ are the volume fraction and relative permittivity of component i. This model was found to be inadequate in

estimating the permittivity of dielectric mixtures in this case, due to the shifting of the Curie Point towards lower temperatures with varying composition. For e.g. at 25°C, based on the permittivity values of BT and BZ a BT:BZ 3:1 mixture would be predicted to have a K= 487 however the actual K= 7,742 almost 1600 times larger than prediction; hence necessitating the use of experiment to determine the dielectric properties.

4.3.2.6.2. Tunabilities and figure of merit

The tunability for the BT: ST: BZ mixtures was measured and plotted on a ternary plot, Figure 4.12. While measurements for the dielectric constant have been reported at a frequency of 100 KHz, tunability measurements were conducted at 1 KHz, at room temperature under a field of 1 KV/mm. The tunability is defined as percentage change in the dielectric constant on application of an external static electric field.

$$\text{Tunability} = \left( \frac{\Delta K}{K_0} \times 100 \right)_{(1KV/mm)} \tag{4.2}$$

Where $K_0$ is the zero field dielectric constant and $\Delta K$ represents the change in the dielectric constant on application of the external field. The tunability was found to be greater near the barium titanate apex and for compositions within the neighborhood of the Curie point at 25$^{o}$C. One composition, BT: BZ 3:1 was found to have ~67% tunability while some compositions specifically along the ST-BZ side displayed no tunability at all.

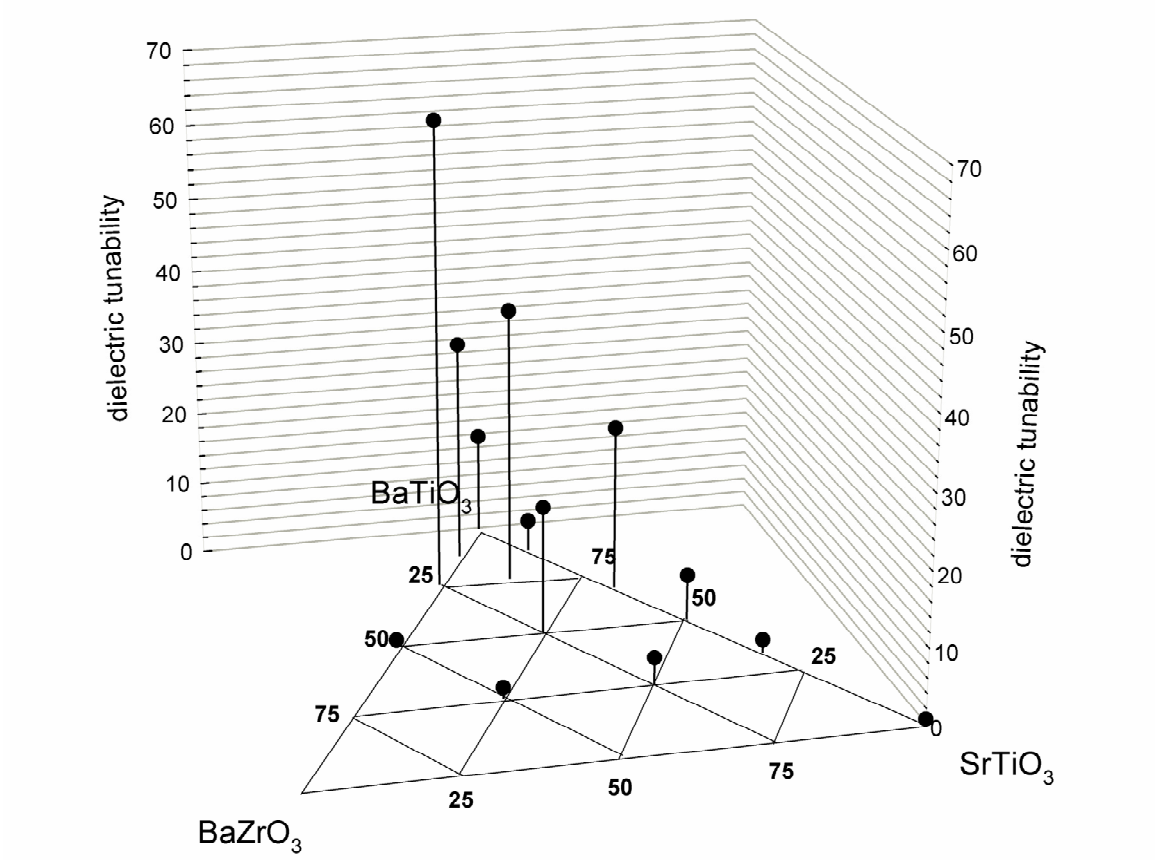


Figure 4.12 Properties of binary-ternary mixtures of BT, ST and BZ as a function of composition at 25°C: dielectric tunability (under an applied bias of 1 KV/mm at 1KHz)

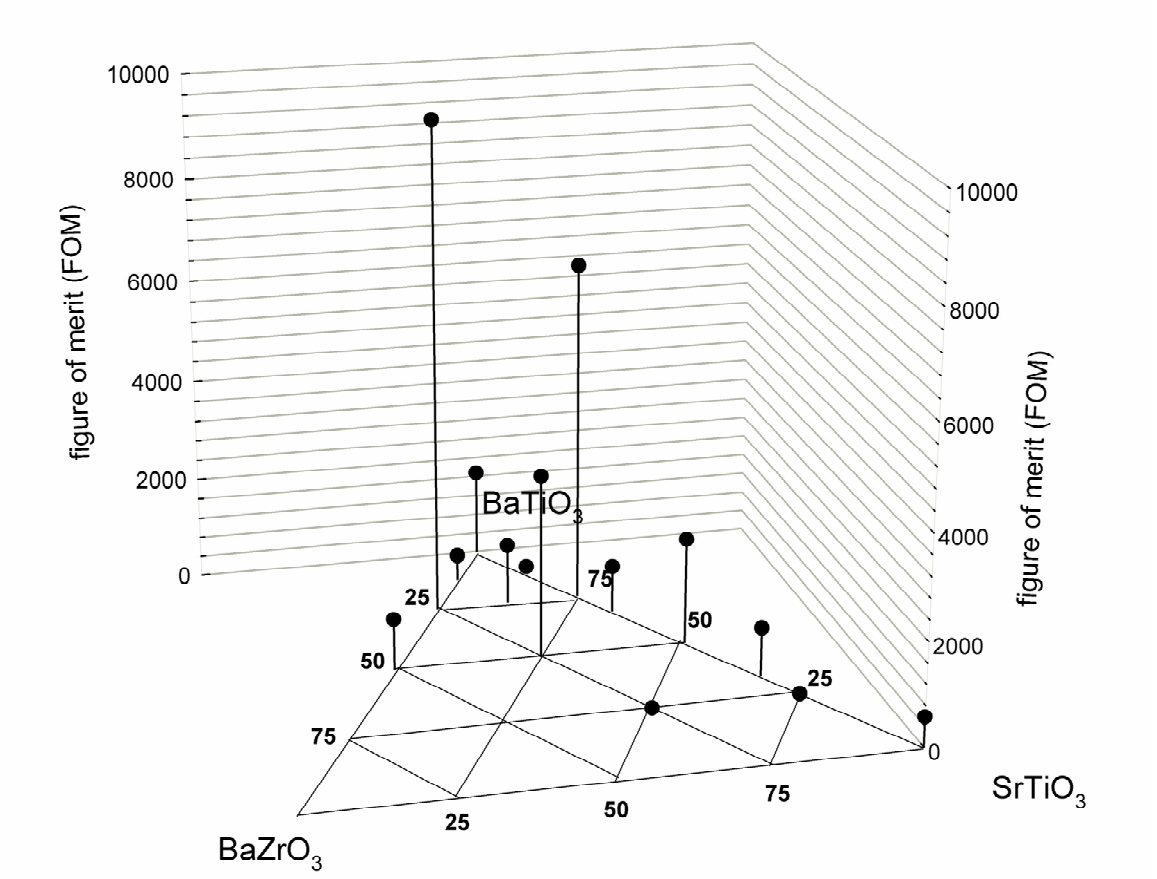


Figure 4.13 Properties of binary-ternary mixtures of BT, ST and BZ as a function of composition at 25°C: Figure of Merit

As a measure of the suitability of these compositions for fabrication of tunable photonic crystals, a quantity named Figure of Merit (FOM)[110] defined as:

FOM= tunability/Tan δ (4.3)

was plotted as shown in Figure 4.13. It was found that the higher magnitudes for the Figure of Merit were closer to the BT apex. The highest value of the FOM was found to be ~9600 for a composition of BT: BZ in the ratio of 3:1. Some other notable

compositions based on the FOM were BT: ST: BZ:: 2:1:1 with FOM=1185 and BT:ST::1:1 with FOM= 1186. Compositions near to the BZ apex having no tunabilities were found to have a FOM=0 as indicated in Figure 4.13.

4.3.2.6.3. Curie Temperatures

The Curie-Weiss law was used to calculate the Curie Temperature ($\theta_c$) for the BT-ST-BZ compositions. Ferroelectrics possess very high permittivity values which vary considerably with frequency of measurement, applied field strength and temperature as shown in this chapter.[81] The permittivity reaches a maximum value at the Curie point ($T_c$) and falls off at higher temperatures in accordance with the Curie-Weiss law

$$K = \frac{A}{T - \theta_c} \tag{4.4}$$

where A is a material specific constant and $\theta_c$ is the Curie temperature in the vicinity of but not identical to the Curie point, $T_c$. To determine the Curie temperatures, the linear portion of the reciprocal of the dielectric constant beyond the Curie point was plotted as a function of temperature and the x-axis intercept determined as the computed Curie Temperature. While this analysis was performed for all compositions, an example of two compositions, BT: ST 3:1 and BT: BZ 3:1 is presented in Figure 4.14. For the BT: ST 3:1 data the 1/K versus T plot was linear close to the curie point and was used in the fit, however for the BT: BZ 3:1 data, non linear portions of the 1/K versus T extended considerably further from the Curie Point and these were ignored as is typically done.[81]

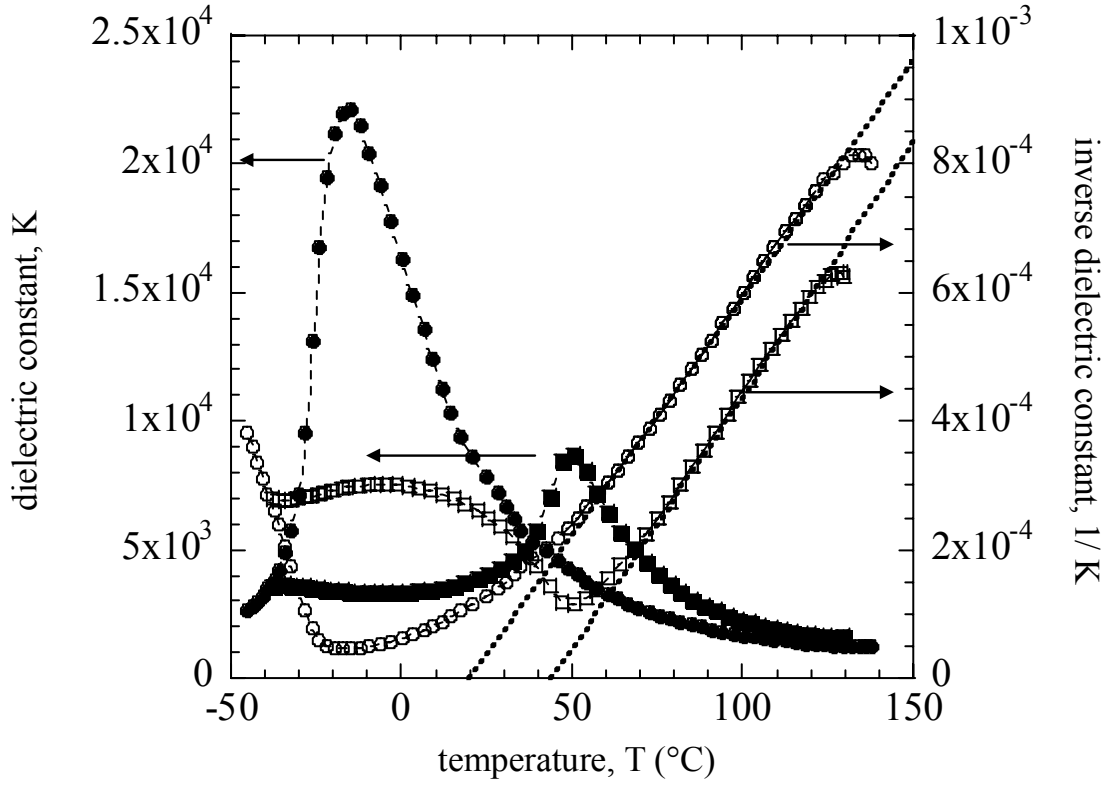


Figure 4.14 An example of the determination of curie temperatures for two compositions of BT: ST 3:1 (K=■, 1/K=□) and BT: BZ 3:1 (K=●, 1/K=○)

The Curie-Weiss law was used to predict the curie temperatures for all composition and has been shown in Figure 4.15. Since the Curie Weiss law is only valid for ferroelectric compositions, it fails to predict the Curie temperature for non ferroelectric compositions such as $BaZrO_3$. Hence compositions for which the Curie point was computed to lie below 0 K were recorded as 0 K. The Curie point was found to decrease steadily as the $Sr^{2+}$ was substituted for $Ba^{2+}$ and $Zr^{4+}$ was substituted for $Ti^{4+}$ in the barium titanate lattice. The decrease in the Curie temperature was linear and could be empirically modeled as:

$\theta_c$ (°C) = 120.5- 318.12x $Ba_{1-x}Sr_xTiO_3$ for 1<x< 0.67 (4.5)

$\theta_c$ (°C) = 126.16- 418.96y $BaZr_yTi_{1-y}O_3$ for 1<x< 0.50 (4.6)

for the binary compositions along the barium titanate-strontium titanate and the barium titanate-barium zirconate axis and was found to be similar to the relationship predicted by Alexandru *et al*. who determined the relationship between the Curie point ($T_c$) and composition as:[141]

$T_c$ (°C) = 120- 360x $Ba_{1-x}Sr_xTiO_3$ for x= 0.25, 0.5, and 0.75 (4.7)

Interestingly, intermediate strontium titanate-barium zirconate compositions exhibited curie points greater than 0 K which may be attributed to the presence of barium zirconate unit cells where the $Zr^{4+}$ had been partially replaced by the $Ti^{4+}$ or alternatively the substitution of $Ba^{2+}$ for $Sr^{2+}$ in the strontium titanate cells.

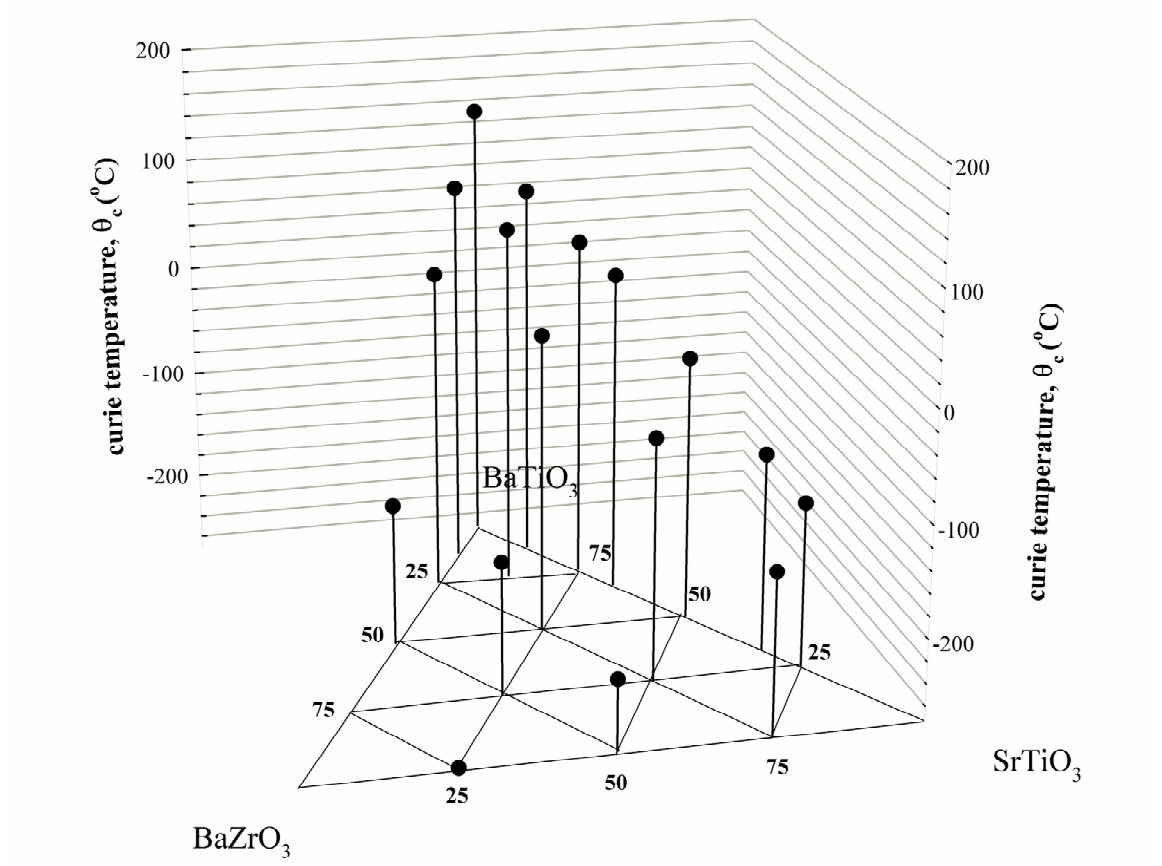


Figure 4.15 Properties of binary-ternary mixtures of BT: ST: BZ as a function of composition at 25°C: Curie Point

## 4.4.Conclusions

A direct write method- robocasting, was used to print bulk film samples of ternary and binary mixtures of barium titanate, strontium titanate and barium zirconate. Dielectric characterization involving measurement of dielectric constant (K), loss tangent (Tan δ) and tunability were conducted. It was evident that increasing the $[Sr^{2+}]$ and the $[Zr^{4+}]$ in the solid solution led to a decrease in the transition temperature, dielectric

constant and tunabilities. A useful Figure of Merit was developed and the highest magnitudes for all three were found to exist near the BT apex. The Curie-Weiss law was used to develop a relationship between composition and Curie Temperature ($\theta_c$) for the barium titanate-strontium titanate and barium titanate-barium zirconate binary mixtures. Evaluation of the dielectric properties of these materials in the context of feedstocks for photonic crystals is important because the composite material should possess a low dielectric constant, high tunability and low dielectric loss as discussed in the next chapter.

# 5. FABRICATION, MODELING AND CHARACTERIZATION OF PHOTONIC CRYSTALS USING DIRECT WRITE

## 5.1.Introduction

Natural or artificial structures with a periodic arrangement of dielectric materials may serve as optical filters to electromagnetic (E.M.) transmissions when certain requirements in the periodicity and dielectric contrast between the constitutive materials are met.[1] The periodic potential imposed on the dielectric function due to the spatial arrangement of matter imposes restrictions on the allowable electromagnetic (E.M.) modes or frequencies within the medium. Hence, E.M. waves of certain frequencies and directions cannot exist within the device. These prohibited frequency regions are labeled as photonic band gaps (PBG) and corresponding devices are appropriately labeled photonic crystals (PC's). The periodic dielectric materials may be engineered to fabricate novel optical devices where properties are based on geometry of assembled structures rather than intrinsic material properties. The photonic band gap is analogous to the electronic band gap in semiconductors in that crystal structure and electron wavelength dictate the band structure. Photonic crystals can be used to control photonic transmissions that range from a millimeters to nanometers in terms of wavelengths. Some intended applications of photonic crystals are in devices such as dielectric mirrors, waveguides, and resonant cavities.[1, 2, 4, 5, 147]

The band gap features (edges and mid-gap frequencies) of a photonic crystal are found to scale inversely with feature size.[1, 4] Hence, to produce optical wavelength photonic crystals, the requisite feature size is on the order of a few micrometers and fabrication using lithographic, holographic or self-assembly techniques are appropriate. However, structures assembled at larger length scales using less expensive techniques may be used to test materials and structures and the results scaled appropriately to evaluate properties at the desired higher frequencies. Photonic band gaps emerge when there is a high refractive index contrast between materials while having a low volume averaged refractive index for the structure as a whole.[14] This implies that the structures should have (a) air as the low refractive index material and (b) high porosity (i.e., 70-90% air). Fabrication of such porous structures requires stringent control of fabrication process variables. Fabrication techniques for photonic crystal fabrication must also be flexible in implementing design changes and have a broad materials palette while being able to impose structural defects in the periodicity to ensure a broad scope of performance.

To create a functional PC, periodicity should be present in the direction of propagation of the E.M. waves. Depending on the number of directions in which the PBG exists, PC's are appropriately labeled as 1-D, 2-D and 3-D photonic crystals. While 1-D and 2-D crystals may be fabricated by relatively simple techniques such as stacking of dielectric layers or constructing a micro-columnar lattice,[1] 3-D photonic crystals provide the greatest challenge requiring precise periodicity in three dimensions while being extremely porous. 3-D photonic crystals are the only ones that can show a complete band gap i.e. a forbidden band irrespective of the incident angle and polarization of E.M

waves. 3-D photonic crystals have been fabricated using both self-assembly and top-down assembly techniques. Principal among the self-assembly methods are nano-crystal sintering,[33] electro-deposition,[34] chemical vapor deposition,[35] and oxide reduction[36] following template assisted self organization of colloidal entities to form periodic structures. The most common top-down assembly methods in use are MEMs,[3] deep x-ray lithography,[29] ion beam lithography,[54] and holographic lithography[31] which rely on the discrete placement, removal or synthesis of materials at precise locations to fabricate the photonic crystal.

While self-assembly techniques are inexpensive and may be conducted in a bench-top environment, they lack the ability to strategically position defects (to introduce specific transmission states) within the structure. However, some recent work by Braun and co-workers indicates that it may be possible to laser direct write defects into a self-assembled photonic crystal using two photon polymerization.[148] In this hybrid method, a self assembled crystal is infiltrated with a polymerizable resin and a localized excitation volume is laser scanned throughout the material to expose desired regions, defining high resolution 3-D embedded features.[149] As compared to self-assembly techniques, top-down assembly techniques which allow the placement of defects are prohibitively expensive and require clean room environments, requiring investments on the order of millions of dollars, while having a limited materials palette.

In this chapter modeling, fabrication, and characterization of 3-D photonic crystals, composed of ternary blends of dielectric materials, fabricated using the robocasting technique are discussed. Using robocasting provides a relatively inexpensive and fast technique to test materials, methods and designs for photonic band gap

structures. Solid solutions of barium titanate (BT), strontium titanate (ST), and barium zirconate (BZ) in varying molar ratios were used as the high dielectric constant material in the photonic crystals. Blending three materials having a range of permittivity allows for an easy route to tune the dielectric properties (constant and loss) and hence affect the band gap properties (see Section 5.3). Fabricated structures were based on the layer-by-layer woodpile structure model developed at Iowa State University, which has previously been shown to have a full 3-D photonic band gap.[3, 7, 8, 12, 150]

Ceramic inks were deposited in the so-called woodpile structure and sintered to obtain finished lattices. Modeling of the photonic crystals was done using the Transfer Matrix Method[20, 21] (TMM) accounting for dielectric loss in the materials. Photonic band gap characterization was conducted in transmission mode using Terahertz-Time Domain Spectroscopy (THz-TDS) and attenuation of E.M. waves as a function of frequency was measured for multiple compositions.

## 5.2.Experimental

### *5.2.1. Printing of flat plates for measurement of refractive index and absorption co-efficient*

Flat bulk films were deposited on an alumina substrate to measure the refractive index and absorption coefficient. The ink preparation and printing operation has been described in chapters 3 and 4 of this thesis. Colloidal inks were loaded into a syringe and extruded through a 150 μm nozzle to assemble arrays of flat samples in the form of bulk films at a write speed of 5 mm/s, taking approximately 1 minute to print each sample.

Each sample in the array was a rectangular (5mm×4 mm) single layer raster filled pattern. This pattern was deposited while maintaining the deposition height at approximately 120 μm over the alumina substrate immersed in oil. After printing, the samples were dried in air for minimum of 12 hours. They were then detached from the substrate and sintered in a manner similar to the photonic crystals of the same composition. Before measuring the refractive index, the thickness of each film was measured using a digital micrometer at 7 different locations across the film and averaged. Thickness varied by less than 5% across each film.

### *5.2.2. Printing of photonic crystal structures*

Photonic crystals were assembled by successive printing of layers that consisted of arrays of parallel lines. Each layer had a common normal vector in the z direction, but was rotated by π/2 radians with respect to adjacent layers. A schematic of this arrangement is given in Figure 5.1. A (100) planar cut of the crystal reveals an apparent face centered tetragonal arrangement of dielectric rods. Such woodpile structures with dimensions of 5mm X 8mm and having 8 layers each were printed using a 150 μm nozzle at a write speed of 5 mm/s over a flat alumina substrate immersed in oil. Within each lattice, a layer of parallel rods were deposited as the base layer with a pitch = d μm, next the deposition nozzle was incremented by a distance =c/4 mm and another parallel layer of rods was deposited but rotated at an angle π/2 to the previous layer, for deposition of the next layer, the rods were deposited parallel to the first layer but offset by a distance d/2 and the fourth layer was parallel to the second layer and offset by a distance again of d/2. Each lattice took approximately 7 minutes to build. This pattern was repeated once to

obtain 8 layers of rods in a face centered tetragonal symmetry or two unit cells. In order to provide easier handling of the lattice, two bounding perimeter lines were included in each layer which served as walls to hold the lattice.

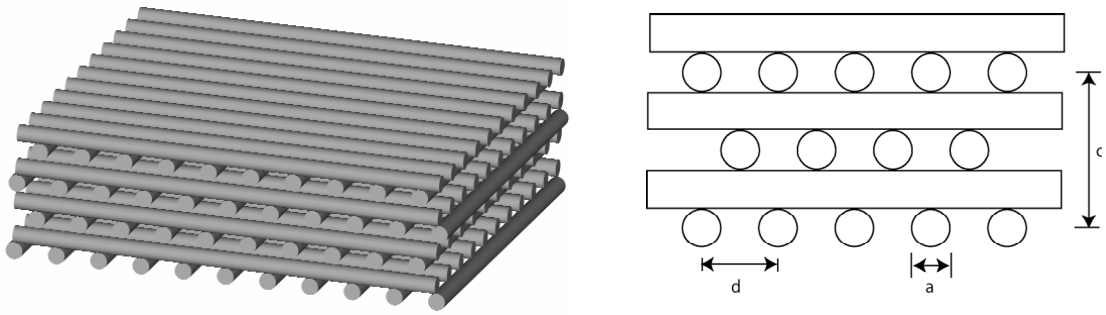


Figure 5.1 Layer by layer model for photonic crystal fabricated using direct write

Printed lattices were carefully removed from oil and were allowed to dry in ambient air for a minimum of 12 hours. After drying, lattices were detached from the substrate and sintered. During sintering, lattices were ramped to their final soak temperature at a rate of approximately 3°C/min. They were held at the soak temperature (sintering temperature) for 1 hour and cooled at approximately 4.5°C/min. Lattices composed of BT or ST alone were sintered at 1340°C. The BZ lattices were sintered at 1500°C. The BT: ST: BZ 1:2:3 and 2:1:1 lattice were sintered at 1280°C and 1500°C respectively. Densification during sintering led to a change in lattice parameters and these were measured and have been reported in their respective sections.

### *5.2.3. TMM modeling of the photonic crystals*

The Transfer Matrix Method (TMM)[20-22, 24] is a finite element analysis method. Within this the space occupied by a photonic crystal is divided into sub-cells with

coupling between neighboring cells. The following curl relations of the electric and magnetic fields in the Maxwell's equations are discretized and z components are eliminated:

$$\nabla \times \mathbf{E} = i(\omega / c)\mathbf{H} \tag{5.1}$$

$$\nabla \times \mathbf{H} = -i(\omega / c)\mathbf{D} \tag{5.2}$$

Where:

**E** is the electric field, **H** is the magnetic field, ω is the angular frequency, c is the speed of light, and **D** is the dielectric displacement vector.

The volume occupied by the PC is split into sub-cells and electric and magnetic fields are calculated for each sub-cell. The transfer matrix is defined by relating the incident fields on one side of the PC to the fields on the other side. The electric and magnetic field are thus calculated in a stepwise fashion to yield the band structure. This method has been used previously to calculate the band structure of 2-D crystals,[15, 16] photonic crystals with complex and frequency dependent dielectric functions,[17] and metallic photonic band gap materials.[18, 19] Further details about the TMM modeling are included in Section 2.1.2.2.

### *5.2.4. THz-TDS measurement of transmission spectrum*

In order to measure the transmission spectrum of the E.M. waves through the PC, terahertz-time domain spectroscopy measurement[151, 152] was used and has been schematically displayed in Figure 5.2 (image courtesy of Dr. Weili Zhang, Oklahoma State University). A close-up top view of the transmitter and receiver chips are displayed above while the general set-up is displayed below in the schematic. The transmitter chip

consists of two 10 μm wide metal lines photolithographically printed on a semi-insulating GaAs substrate with a separation distance of 80 μm. The transmission lines are 600 nm thick (100nm Ti + 500nm Al) and partially embedded in the substrate. The receiver chip consists of two 5 μm wide metal lines separated by a distance of 10 μm except in the middle where separation distance is 5 μm. The receiver chip is fabricated on an ion-implanted silicon on sapphire (SOS) substrate. A bias of 70 V is applied between the transmission lines on the transmitter chip.

A mode-locked Ti: Sapphire laser capable of generating 88 MHz, 26 femtosecond pulses having a nominal wavelength of 810 nm was used for generating and detecting THz radiations. The laser pulses were focused on the inner edge of the positively biased line on the transmitter chip. Each pulse generated electron-hole pairs which were subject to acceleration due to the effect of the bias field. The accelerating charges produced a burst of terahertz radiation which was emitted into the silicon lens attached to the back of the transmitter. The THz radiation was then collimated using an arrangement of parabolic mirrors (M1-M4) onto the silicon lens receiver chip.

The antenna on the receiver chip was photo-conductively switched by another femtosecond optical pulse from the same Ti: Sapphire laser. The receiver was connected to a lock-in amplifier through a low noise current amplifier. When gated the receiver generated a direct current (D.C.) which was proportional to the instantaneous electric field of the received THz electromagnetic wave. This current was the measured value. By changing the relative time delay between the optical gating pulse and the detecting THz pulse the entire shape of the THz radiation, which included both amplitude and phase information, could be mapped out as a function of the relative time delay. The THz

pulses were recorded with and without the sample in the transmission path to obtain sample and reference signal. The frequency dependent parameters of the sample were obtained by comparing the Fourier transformed spectra of the corresponding time domain pulses.

For the photonic crystal measurement the transmission of the THz pulses was measured in the stacking or <001> direction, normal to the layers containing parallel rods. At the sample position, the beam had a waist diameter of 3.5 mm. The time domain data collected was converted to the frequency domain by numerical Fourier transform yielding amplitude as a function of frequency. The photonic crystal spectrum was divided by the reference (air) spectrum to remove the system response of the experiment. This ratio yielded the change in amplitude in transmitted signal as a function of frequency.

For measuring the refractive index a bulk film sample was placed in the path of transmission of the THz waves and its spectra compared to that of transmission through air as reference. The shift in phase yielded the refractive index caused due to a slowing of the THz waves while traveling through the sample. Fourier transforms were done on both the film sample and air spectra to obtain amplitude as a function of frequency. The bulk film spectrum divided by the reference (air) spectrum yielded the change in amplitude which could be used to estimate absorption through the sample.

At least 3 runs were conducted for each sample (photonic crystals and bulk film) and averaged. The measurement showed high reproducibility within the measurement range.

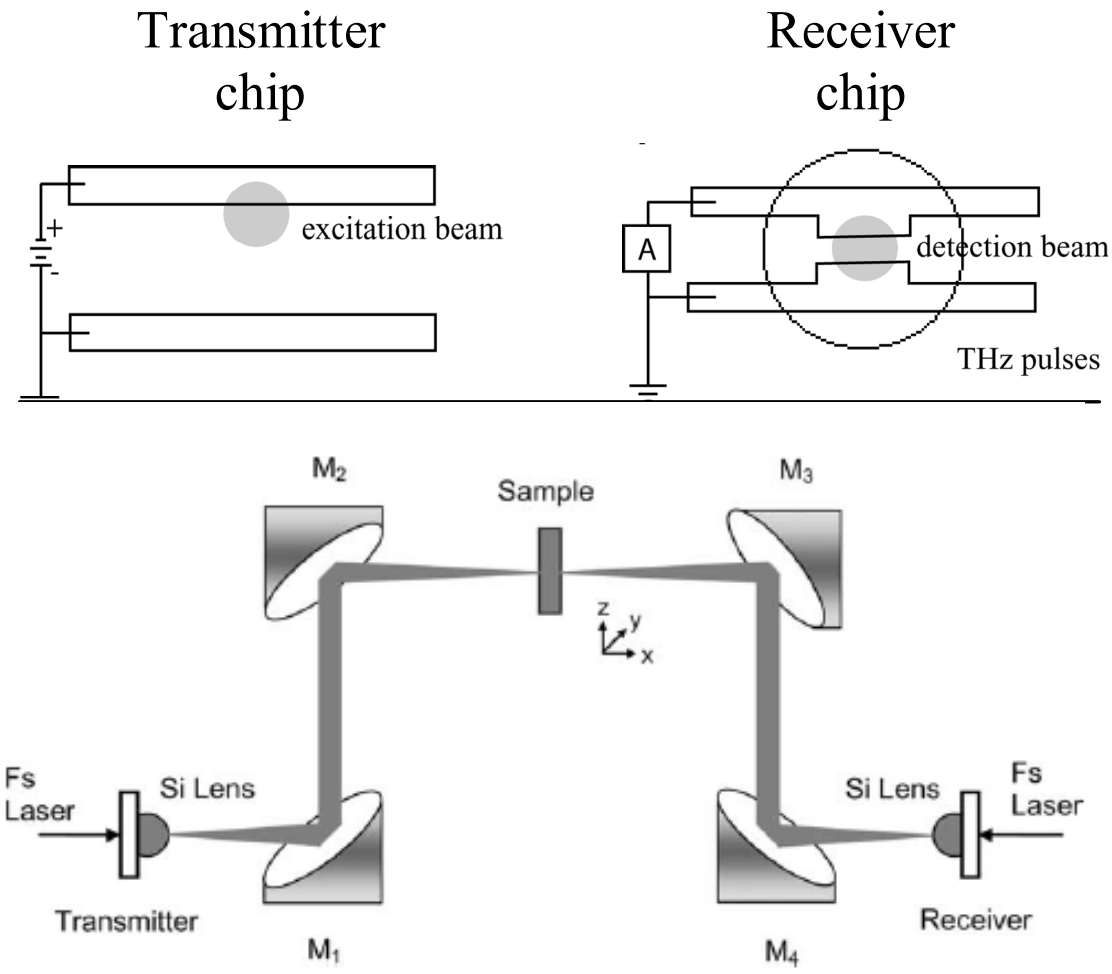


Figure 5.2 The THz-TDS setup used to measure dielectric properties on bulk films and transmission across a photonic crystal along the stacking direction

## 5.3. Results

### *5.3.1. Assembled photonic band gap structures*

Figure 5.3 shows a representative photonic lattice assembled using the direct write technique. Figure 5.3(a) is an optical image showing a printed lattice composed of BT: ST: BZ 1:2:3 partially sintered to 1280°C. The lattice approximately measured 12mmX12mmX1mm and contained 25 parallel rods within each layer. The lattice was printed with perimeter walls for ease of handling and so that the lattice could be mounted onto a holder for measuring transmission. Figure 5.3(b) is a top view SEM image of the lattice showing parallel rods within each layer and underlying layers. Measurements on the image confirm that the lattice spacing is (488.006) +/- 14.64 μm and the rod diameter is (158.27) +/- 4.75 (within 3% in each case). The filling fraction within each layer is ~32%. Inset (c) shows a top-view SEM image of a single rod and inset (d) shows the cross-sectional side view of the lattice showing the face centered tetragonal placement of the cylindrical rods.

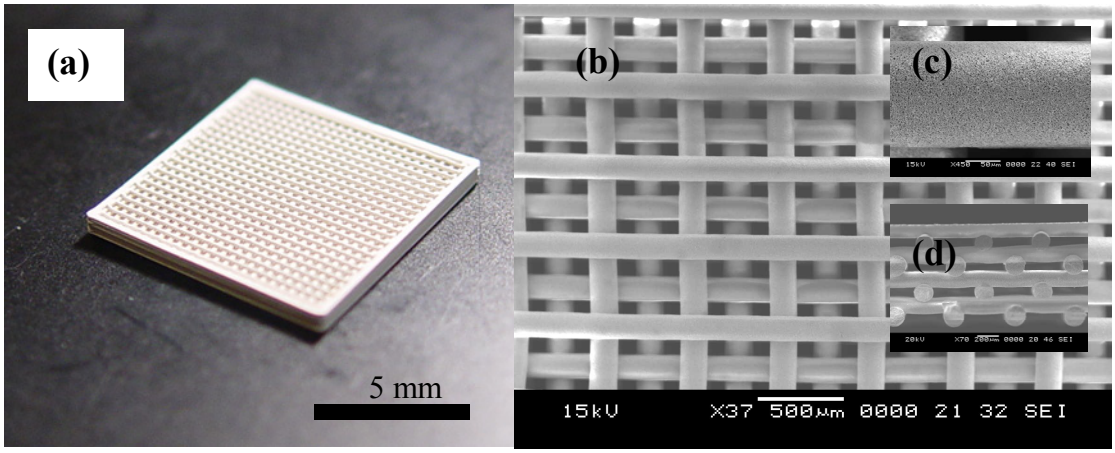


Figure 5.3 A representative photonic lattice printed using robocasting showing: (a) optical image of a large 12mm X 12 mm lattice, (b) SEM image showing the parallel FCT arrangement of rods (c) SEM image of a single rod, and (d) a side view of the lattice showing the FCT arrangement of rods

Measurement using image analysis software confirms that the unit cell thickness c is 434 +/- 13.02µm. Measurements on individual lattices made of different compositions have been reported in their respective sections. Figure 5.4 is a comparison of the lattices printed using different compositions showing that composition and sintering temperature affected optical color and lattice spacing for each lattice.

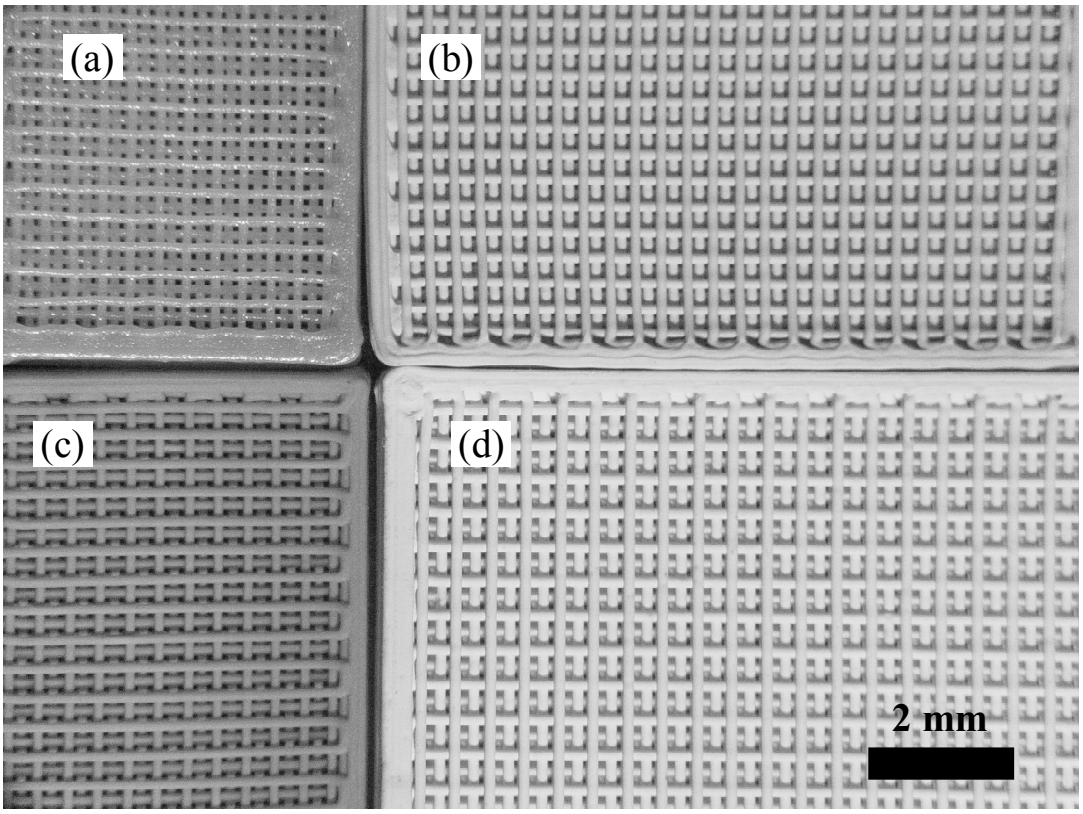


Figure 5.4 Photonic lattices printed using the direct write technique with composition (a) barium titanate, (b) strontium titanate, (c) barium zirconate, and (d) a mixed ternary composition of barium titanate: strontium titanate: barium zirconate 1:2:3. The color and lattice parameters varied with sintering temperature and composition

5.3.1.1. Pure $BaZrO_3$ (low permittivity) lattices

For measurement of the dielectric constant and loss, a THz transmission measurement was performed on relatively flat (within 5%) bulk film sample measuring 100-120 μm in thickness for each composition. The transmitted intensity of THz pulses through both air (as reference) and the sample were measured. Reflections from the film surfaces, if any, were cleanly separated from the main signal allowing for analysis of the

main pulse alone. Fourier transform of the sample and reference pulses yielded the corresponding complex amplitude spectra. Ratio between sample and reference spectra gave the effective absorption by the sample and the effective phase shift in the main signal (induced due to transmission through the sample) yielded the refractive index. The frequency dependent absorption coefficient ($\alpha$) and refractive index ($n_1$) were converted using the following equations to yield the dielectric loss and dielectric constant values:

$$\alpha = -\frac{1}{film\ thickness} \times \left( \frac{Intensity_{sample}}{Intensity_{reference}} \right) \tag{5.3}$$

$$n_2 = \alpha.\lambda_0/4\pi \tag{5.4}$$

$$\varepsilon = n^2 = (\varepsilon_r + i\varepsilon_i)^2 \tag{5.5}$$

$$\varepsilon_r = n_1^2 - n_2^2 \tag{5.6}$$

$$\varepsilon_i = 2n_1n_2 \tag{5.7}$$

Where $\lambda_0$ is the wavelength of incident radiation, n is the complex refractive index, $n_1$ is the index of refraction, and $n_2$ is index of absorption, $\varepsilon$ is the complex dielectric function, $\varepsilon_r$ is the relative permittivity or dielectric constant (also K in Chapter 4) and $\varepsilon_i$ is the dielectric loss, all of which are frequency dependent. The loss tangent discussed in Chapter 4 is defined as:

$$\tan\delta = \varepsilon_i/\varepsilon_r \tag{5.8}$$

For pure barium zirconate film, as the frequency of incident microwaves was increased from 100 to 2000 GHz the dielectric permittivity was found to increase from approximately 20 to 24 and the loss was found to increase from 0.8 to approximately 2

indicating substantially higher loss than conventional PC materials such as GaAs, silicon and alumina.[81]

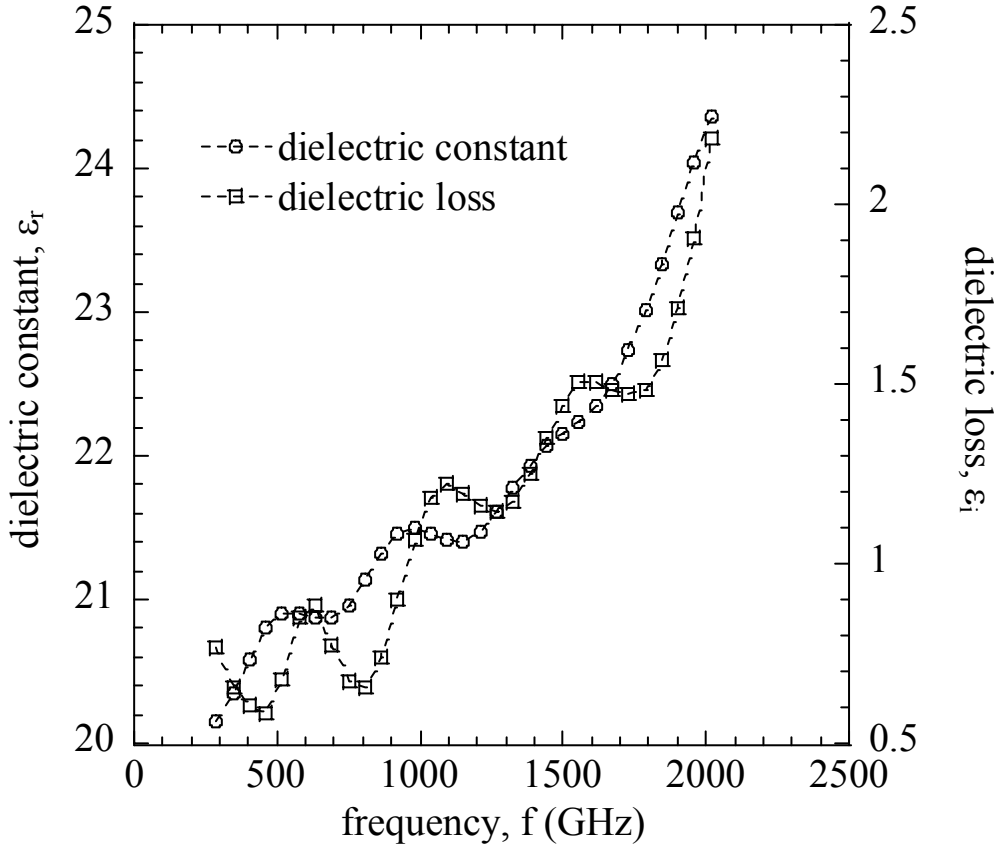


Figure 5.5 Permittivity and dielectric loss for barium zirconate in the 100 GHz-1000 GHz range

The transmission spectra for representative lattices of barium zirconate that were sintered to 1500 °C have been shown in Figure 5.6 and Figure 5.7. Table 5.1 lists details of the average rod diameter (a), pitch (d) and unit cell (4 layer) thickness (c) for the two lattices, Lattice A and Lattice B. The transfer matrix method, using an averaged value for the permittivity and loss (from Figure 5.5), predicted a primary band edge at 200 GHz

and 238 GHz and a mid-band frequency at c.a. 265 GHz and 279 GHz for Lattice A and Lattice B respectively.

| Lattice | Diameter (um) | Pitch (um) | Unit cell thickness (um) | Composition |
|---|---|---|---|---|
| A | 120 | 413 | 455 | $BaZrO_3$ (1500°C) |
| B | 135 | 367 | 455 | $BaZrO_3$ (1500°C) |

Table 5.1 Parameters for the two photonic woodpile lattices made with barium zirconate

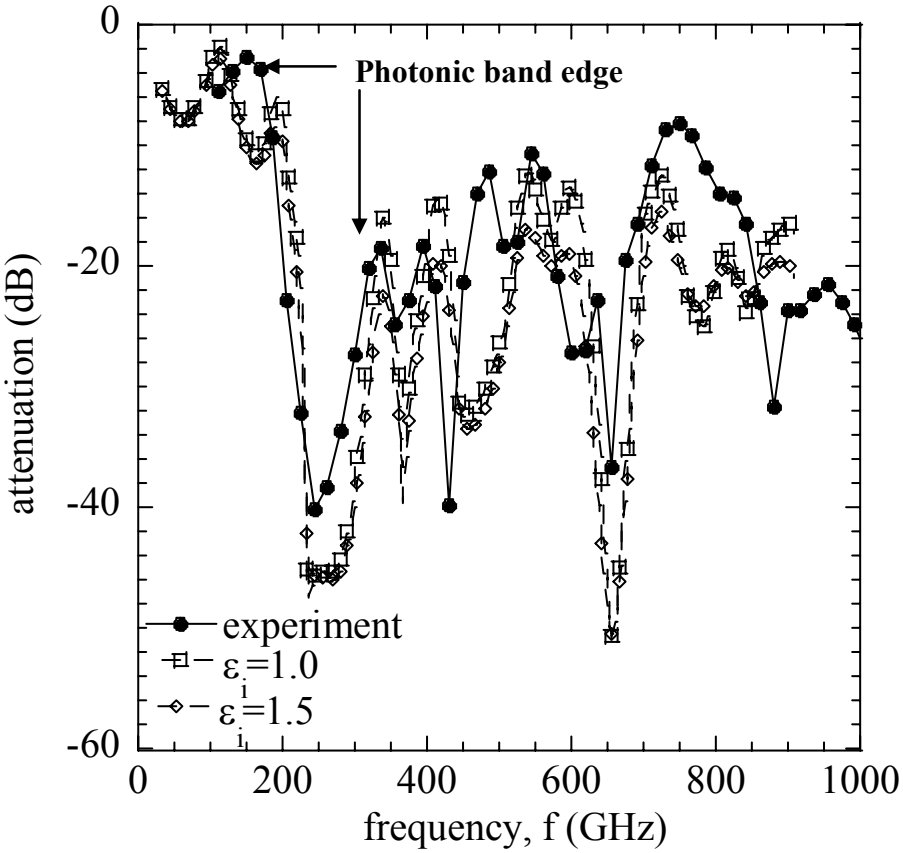


Figure 5.6 Attenuation spectra for a barium zirconate lattice with a=120 μm, d=413 μm and c=455 μm. A primary band gap was observed between 180 and 330 GHz and was a close match to simulation done using TMM for the same structure

The transmission spectrum, for Lattice A, for propagation of THz waves along the stacking direction has been plotted in terms of attenuation as a function of frequency in Figure 5.6. Several dips in transmission were observed at various frequencies for the structure however the primary dip in transmission is referred to as the primary band gap and is characterized by band edges, $f_{low}$, $f_{high}$, and a mid-gap frequency, $f_{mid}$. At 180-330 GHz a strong attenuation in transmitted signal was seen indicating the existence of a photonic band gap in the 3-D structure. Therefore, the band edges and the mid gap frequency of the primary band gap for this crystal were: $f_{low}$=180 GHz, $f_{high}$=330 GHz and $f_{mid}$=255 GHz. The gap extended over a spectral range of $\Delta f$= 150 GHz and within the gap attenuation was on the order of -40 dB. Transmission dropped to 1% of incident radiation. A large gap: mid-gap ratio ($\Delta f/ f_{mid}$) of 58% was observed indicating an attenuation of 20 dB per unit cell (the lattice had two unit cells or layers in the stacking direction). Higher order band gaps were formed at higher frequencies due to higher order diffractions.[1] Most notable of these are the secondary band gaps occurring at a mid-gap frequency of ~ 420 GHz and ~650 GHz where the attenuation reached -40 dB and -38 dB respectively. Recovery in transmittance was only 10% in regions beyond the primary band gap and could be attributed to power dissipation within the material.[81]

Simulations for this structure were conducted using the TMM method and using the lattice parameters described for Lattice A in Table 5.1. The dielectric constant was assumed to be $\varepsilon_r$= 24 and two values for loss at $\varepsilon_i$ =1.5 and $\varepsilon_i$=1 were assumed. An excellent match between theory and experiment in the case of the primary band gap was observed, as shown in Figure 5.6. Band edges, for the primary band gap, were predicted at 200 GHz and 330 GHz and matched experiment, while attenuation within the band gap

matched within reasonable expectation (a difference of 4 dB was observed at the mid-gap frequency). In the case of higher order band gaps, it was observed that predicted mid-gap frequencies were generally higher than those determined from experiment.

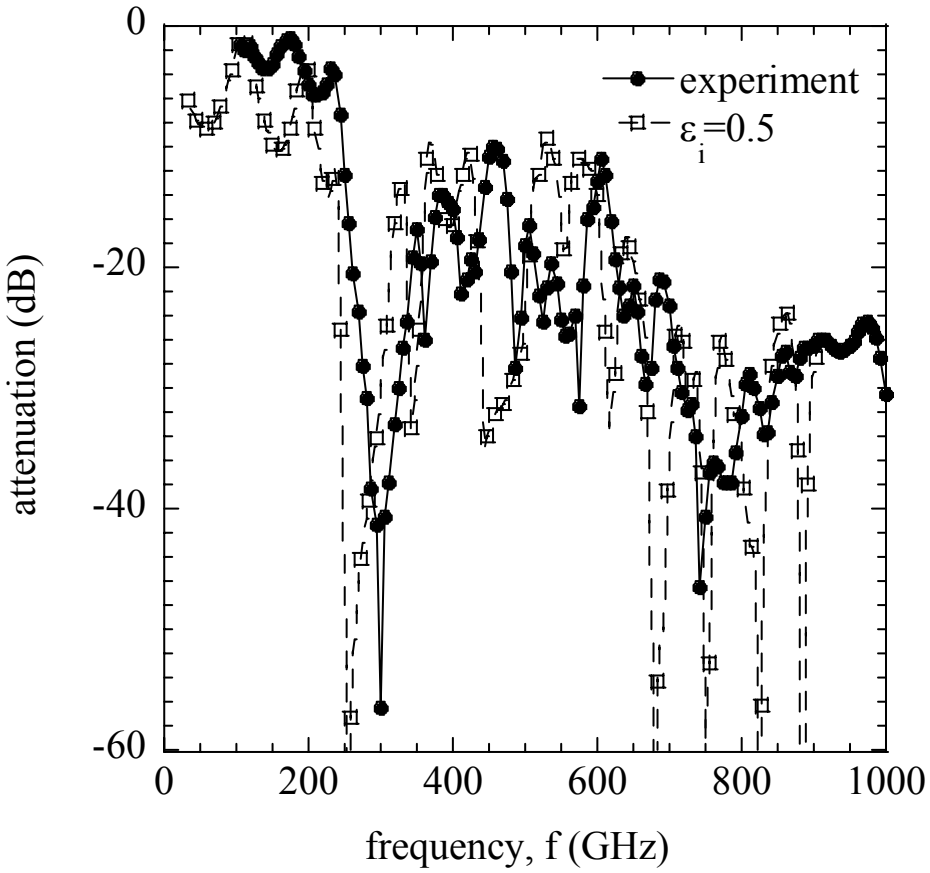


Figure 5.7 Attenuation spectra for a barium zirconate lattice with a=135 μm, d=367 μm and c=455 μm. A primary band gap was observed between 236 and 344 GHz.

Another woodpile like structure of barium zirconate was fabricated with parameters: rod diameter=135 μm, d=367 μm and c=455 μm and attenuation spectrum recorded for propagation of THz waves along the stacking direction. The transmission

spectrum for this lattice has been shown in Figure 5.7. For this structure it was intended to determine the effect of decreasing the pitch on the location of the primary band gap. The primary band gap was observed to exist between $f_{low}$=236 GHz and $f_{high}$=344 GHz with $f_{mid}$= 290 GHz and again provided a close match to simulation where predicted $f_{low}$= 238 GHz and $f_{high}$= 320 GHz. The difference in mid-gap frequency between experiment and model was ~4% which is identical to the difference for lossless photonic crystals made using lithography.[3] Attenuation was higher on the order of 29 dB/unit cell as compared to the previous structure and a gap/midgap ratio of ~ 20% was determined. A decrease in pitch from 413 to 367 μm resulted in an increase in the mid-gap frequency (as discussed in section 2.1.2.1.1) for the primary band gap to 290 GHz from 255 GHz with a spectral width of Δf=108 GHz. The compared simulation used an estimate of $\varepsilon_r$=21 and $\varepsilon_i$=0.5, while assuming lattice parameters as described, for Lattice B, in Table 5.1. It was noted however that while modeling predicted the greatest attenuation to lie at 258 GHz, experimentally it was determined to lie at ~299 GHz.

5.3.1.2. Ternary BT: ST: BZ (low permittivity) lattice

A ternary composition composed of BT: ST: BZ in the molar ratio of 1:2:3 was used to fabricate both bulk films and lattices to test for band structure. After deposition and drying, the structures were partially sintered at a soak temperature of 1280°C for 1 hour. The porous ceramic had a lower effective dielectric constant owing to the mixing effect for air with ceramic. After partial sintering, the lattice geometry was measured to determine parameters. The rod diameter, pitch and unit cell thickness were found to be 150 μm, 500 μm and 450 μm respectively.

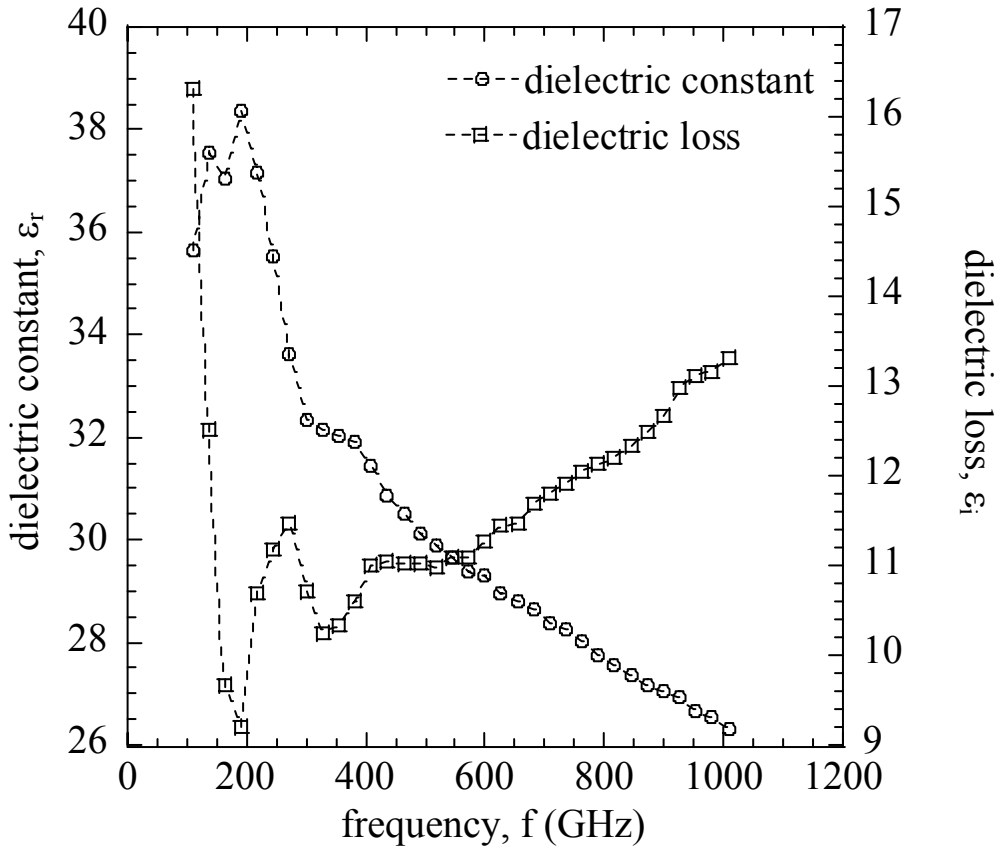


Figure 5.8 Dielectric constant and loss as a function of frequency of THz radiation for a bulk film composed of a ternary mixture of $BaTiO_3$, $SrTiO_3$, and $BaZrO_3$ and partially sintered at 1100°C for 1 hour

The bulk film measurement yielded the refractive index and absorption which were converted to dielectric constant and loss values. As the frequency of the incident waves was increased there was a decrease in the magnitude of $\varepsilon_r$ from ~35 GHz at 100 GHz to ~25 at 1000 GHz as shown in Figure 5.8. The magnitude of $\varepsilon_i$ also varied from ~9 to 16 in the same frequency range. Beyond 1000 GHz, transmitted signal was noisy

and this data was ignored. The transmission spectra for the BT: ST: BZ 1:2:3 lattice measured along the stacking direction has been depicted in Figure 5.9 and characterizes its band structure.

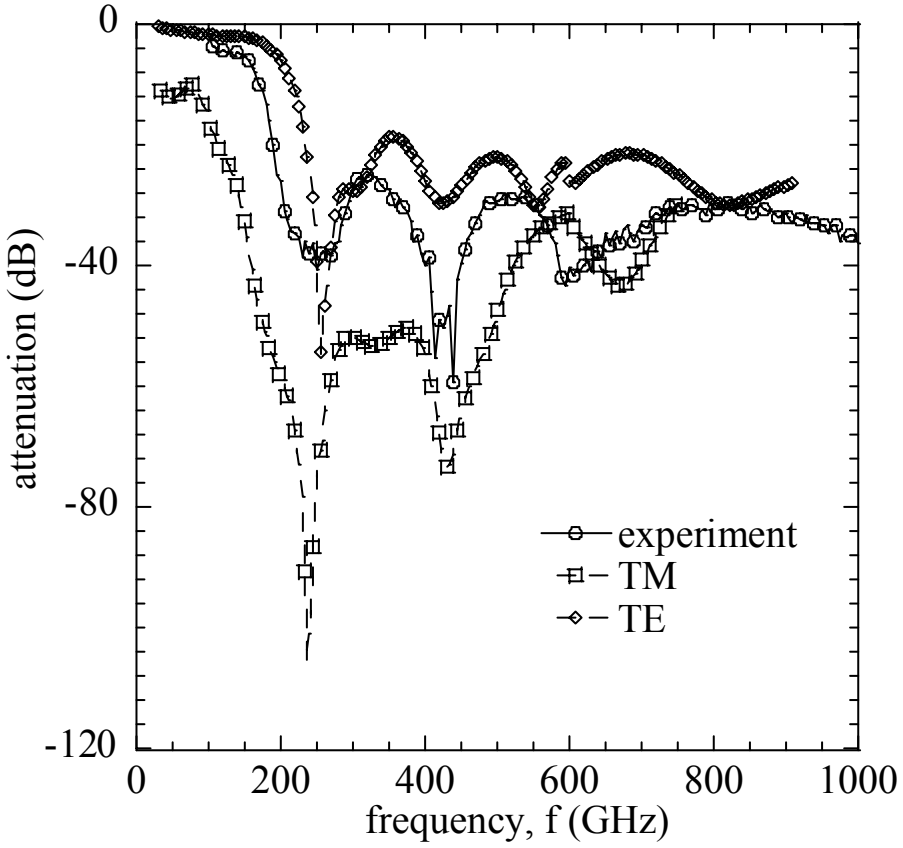


Figure 5.9 Attenuation spectra, as a function of frequency, measured along the stacking direction for a lattice composed of a ternary mixture of $BaTiO_3$, $SrTiO_3$, and $BaZrO_3$ and partially sintered to 1100°C. Primary band gap lay between 133 - 288 GHz

For this structure a primary band gap was found to have band edges between $f_{low}$=133 GHz and $f_{high}$=288 GHz with a mid-gap frequency at $f_{mid}$=210 GHz and $\Delta f$=155 GHz as shown in Figure 5.9. An attenuation of 20 dB/unit cell was measured in the

primary band gap. Higher band gaps were found to be centered at 400 GHz and 575 GHz respectively. For comparison, both the TM (transverse magnetic, electric field parallel to 1st layer of rods) and TE (transverse electric, electric field perpendicular to 1st layer of rods) simulations were performed using the measured lattice parameters and estimating $\varepsilon_r$ and $\varepsilon_i$ to be 34 and 8 respectively. The measurement on the lattice was done using TEM polarized THz waves and hence it is expected that actual band structure would lie in-between TM and TE simulations and this was found to be the case. The range of primary band gaps predicted for the TM and TE modes were 75 GHz-288 GHz (attenuation=-90 dB) and 152 GHz-355 GHz (attenuation=-55dB) respectively. Averaging the TM and TE primary band gaps predicted the band gap for the structure to lie in the range 133 GHz-320 GHz ($f_{mid}$=226 GHz) with an attenuation of 72 dB. Actual measurement indicated that the primary band gap ranged from 133-288 GHz with $f_{mid}$= 210 GHz. Attenuation was lower at 40 dB indicating lesser loss than that measured on the bulk film sample. Both the TM and TE simulations showed higher order band gaps near 450 GHz, 550-600 GHz (TE) or 650 GHz (TM) in agreement with measurement.

#### 5.3.1.3. Pure $SrTiO_3$ (medium permittivity) lattice

Figure 5.10 shows the band structure for a lattice composed of strontium titanate measured for propagation of THz waves in the stacking direction while the inset shows the variation in dielectric constant and loss with increasing frequency. Considerably higher permittivity and loss values across the measured frequency range were recorded for the strontium titanate bulk film as compared to the previous two samples.

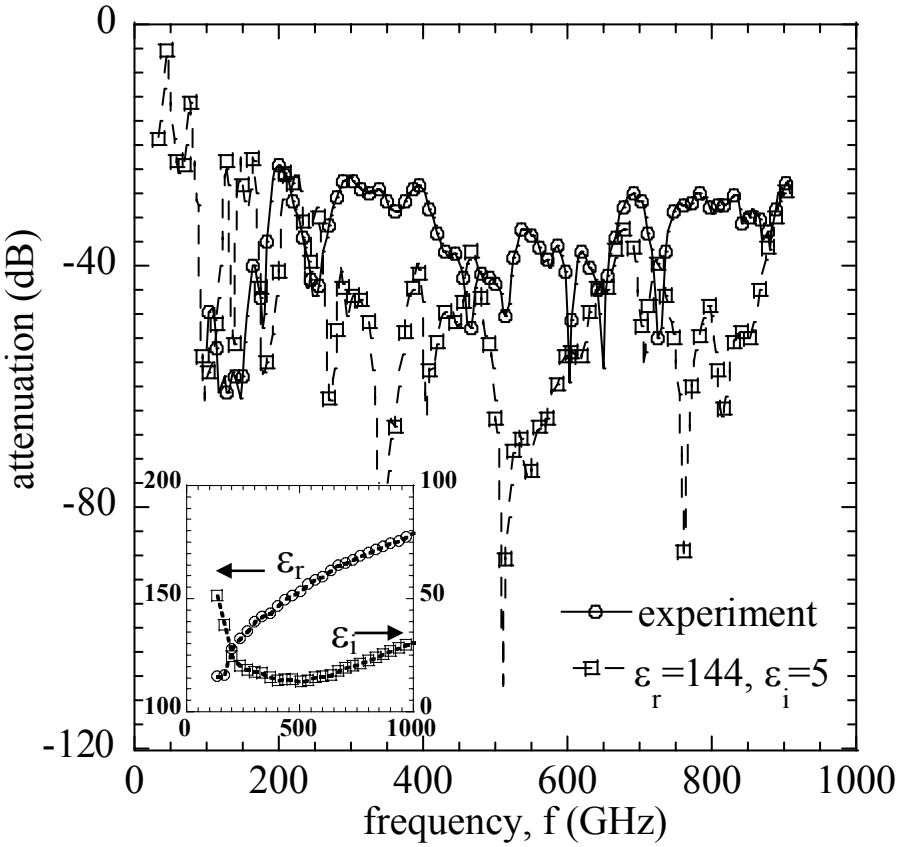


Figure 5.10 Attenuation spectra measured along the stacking direction for a lattice composed of $SrTiO_3$. Primary band gap was observed to lie below 100 GHz. Inset describes variation of dielectric properties with frequency of incident THz radiation.

A broad range for $\varepsilon_r$ ranging from 115 to 180 was recorded and $\varepsilon_i$ ranged from 12 to 50. The rod diameter, pitch and unit cell thickness were determined to be 131 μm, 397 μm and 430 μm respectively. The band structure was modeled using these measured lattice parameters in the TMM method assuming $\varepsilon_r$= 144 and $\varepsilon_i$=5. Modeling results predicted that a primary band gap would lie between $f_{low}$=77 GHz to $f_{high}$=127 GHz with an attenuation of -60 dB. At the time of these measurements, the THz setup had a lower

detection limit of 100 GHz. From the experiment it was determined that at 100 GHz there was already an attenuation in transmission at approximately 45 dB, perhaps indicating that frequencies at 100 GHz were already within the primary band gap. A band edge was observed at $f_{high}$= 160 GHz with a maximum attenuation beyond 100 GHz at 60 dB. Comparing experiment and modeled band structure indicated that while the primary band gap appeared to be approximately in the region predicted by model, higher frequency band structure did not show a very good match to prediction. The high loss in the material caused transmissions to lie below 5% (~26 dB) beyond the primary band gap.. While measured $\varepsilon_i$ ranged from 12-50, actual lattice transmission was in general higher than that predicted by model (assuming $\varepsilon_i$=5) indicating that loss for the ST composing the lattice was not as high as that measured in the bulk film.

#### 5.3.1.4. Pure $BaTiO_3$ (high permittivity) lattice

Figure 5.11 shows the attenuation spectrum recorded for a barium titanate lattice with final lattice parameters: rod diameter= 119 μm, pitch= 360 μm and unit cell thickness = 430 μm. The dielectric constant and loss for a barium titanate thick film, as displayed in the inset in Figure 5.11, ranged from 450~125 and 250~70 respectively. The high dielectric constant tended to shift the primary band gap to below 100 GHz, less than the detection limit of the THz-TDS setup. Consequently, at 100 GHz, transmission was recorded on the order of -40 dB (1%), indicating that the primary band gap indeed lay below 100 GHz. The attenuated band structure was observed to extend up to 700 GHz where a recovery in transmission was recorded at ~-18 dB. The maximum attenuation was observed to be -60 dB and could be attributed in a large part to dielectric loss

mechanisms rather than a due to the formation of a photonic band gap. Due to the absence of reliable data below 100 GHz, i.e. at the location of the primary band gap, the band structure was not modeled.

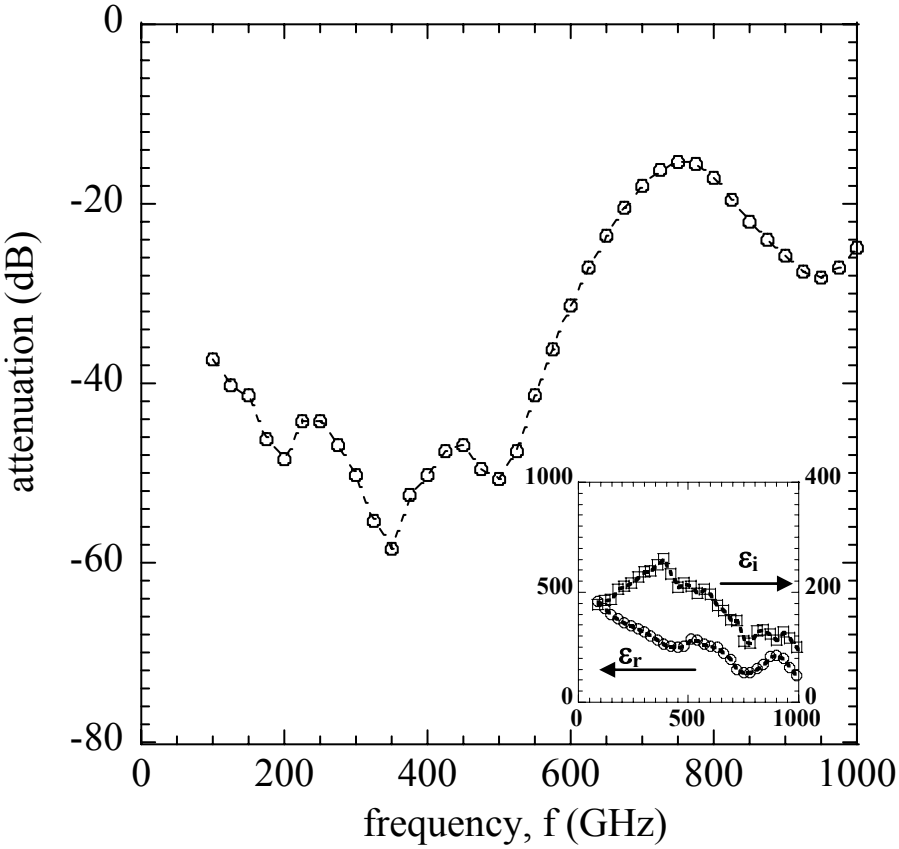


Figure 5.11 Attenuation spectra for a barium titanate lattice having a high permittivity and a primary band gap predicted to lie below 100 GHz. Inset shows the change in dielectric properties as a function of frequency of incident THz waves

5.3.1.5. Ternary BT: ST: BZ (high permittivity tunable) lattice

Based on the Figure of Merit (measured at 1 KHz) for dielectric tunability described in Chapter 4, the composition of BT: ST: BZ mixed in the molar ratio of 2:1:1 was expected to display a high tunability to loss ratio. Refractive index and loss measurements for a bulk film sample and transmission through a lattice made of this composition measured in the stacking direction were conducted. In the case of measurement of the dielectric constant and loss using bulk film transmission measurements, very little signal was detected through a ~100 μm bulk film. It is hypothesized that almost all incident signal was dissipated due to high absorption within the material. Nevertheless, the weak signal was converted to permittivity and loss values and plotted as inset in Figure 5.12. Extremely high permittivity values were recorded on the order of ~4500 along with loss values on the order of 500. The transmission spectrum for a lattice made of a ternary mixed composition $BaTiO_3$: $SrTiO_3$: $BaZrO_3$ mixed in the molar ratio of 2:1:1 and having lattice parameters: rod diameter= 120 μm, pitch= 410 μm and a unit cell thickness of 410 μm has been displayed in Figure 5.12. Due to the high dielectric constant, the primary band gap in transmission lay below the lower measuring limit for the THZ-TDS setup (100 GHz) and could not be detected reliably. At 100 GHz transmission was recorded at ~1% (44 dB) and recovered to almost 40% (-10 dB) at ~725 GHz. It is believed that fabricating bulk films that are much thinner than 100 μm and controlling loss mechanisms in the structure will yield specimens for which the dielectric constant and transmission spectra may be measured reliably.

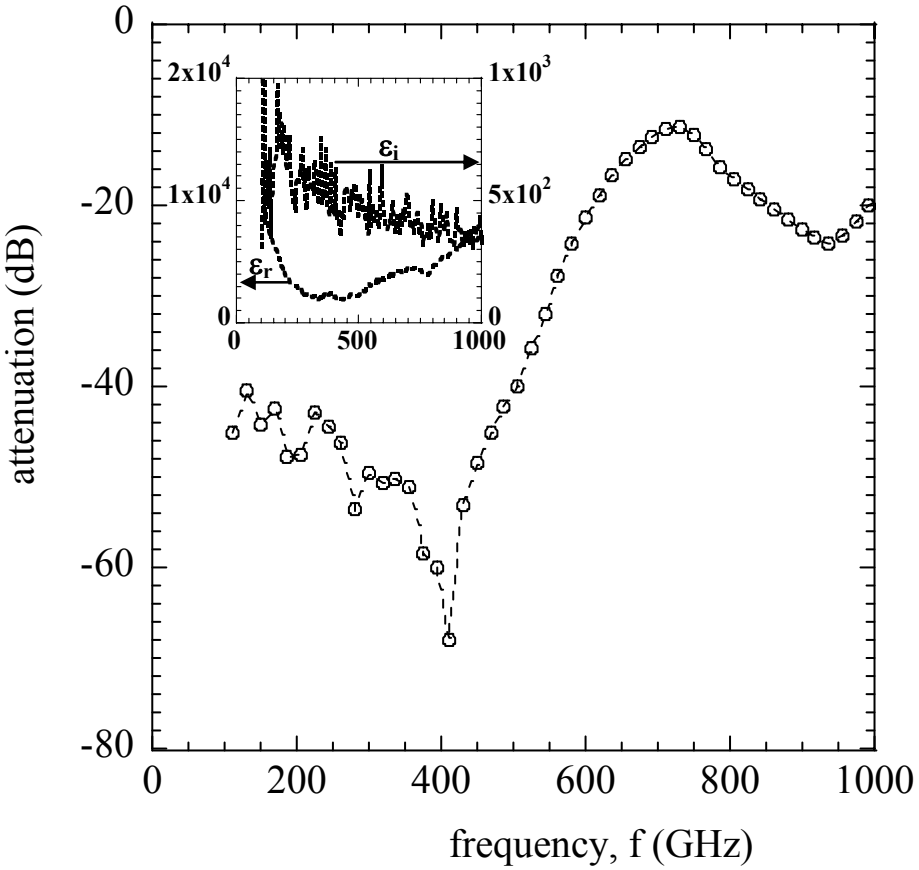


Figure 5.12 Transmission for a lattice composed of BT: ST: BZ in the molar ratio of 2:1:1 and having a primary band gap that lay below 100 GHz. Inset shows the variation of dielectric constant and loss with frequency

**5.4.Discussions**

The TMM technique was used to model the primary band edge frequency for lattices with a=150 μm, d= 500 μm, and c = 504 μm and the results are presented in Figure 5.13. The ideal assumption of a lossless dielectric ($\varepsilon_i$=0) was used in these calculations. The primary band gap frequency decreases monotonically in an exponential fashion for the photonic crystal, with an increase in the dielectric constant.

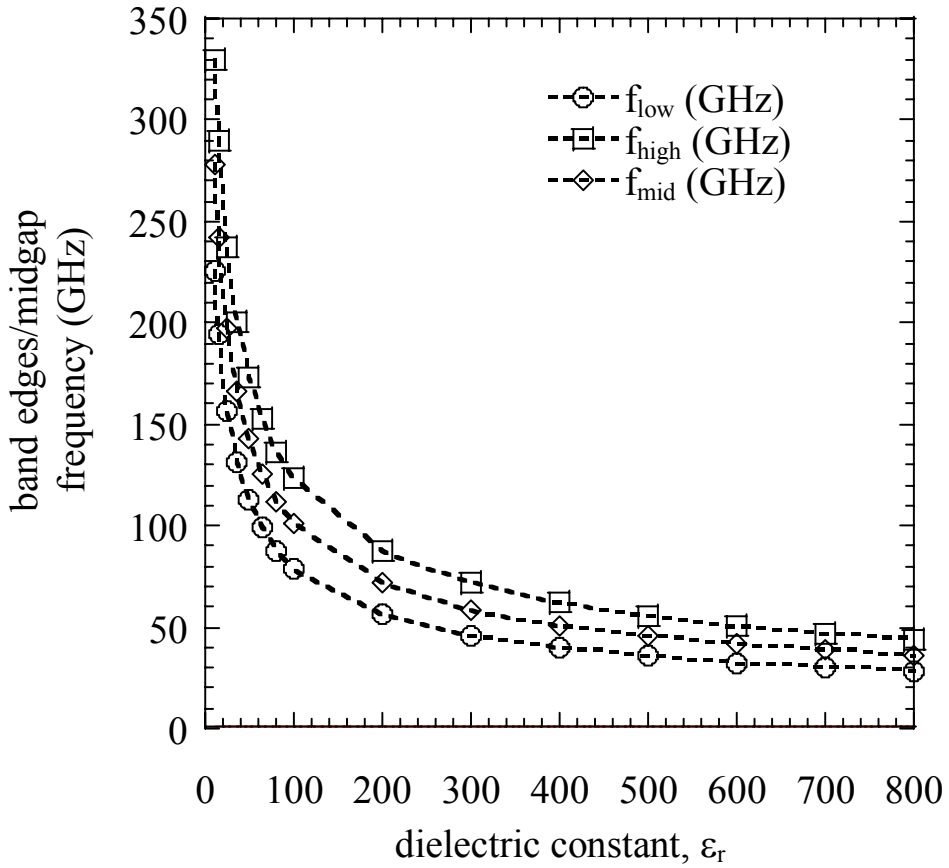


Figure 5.13 Predicted primary gap edge frequencies as a function of dielectric constant for a photonic crystal with fixed lattice parameters.

The band gap frequencies tend to decrease rapidly with dielectric constant till about $\varepsilon_r$=100 and then show a gradual decrease with increasing permittivity. The exponential decay curve could be modeled by the function:

$$f_{mid}\ (GHz) = 1.001 + 16.461e^{-.55\varepsilon r} \quad (5.9)$$

Quantitatively, the results from experiments followed simulation results for low permittivity compositions i.e. in the case of barium zirconate and BT: ST: BZ 1:2:3 as discussed in section 5.3.3.1 and 5.3.3.2. For a strontium titanate photonic crystal the primary band gap coincided with the prediction, i.e. a gap at 100 GHz, however higher order band gaps did not follow the simulation very well. For the barium titanate and the BT:ST:BZ 2:1:1 compositions, the predicted band gap lay well below 100 GHz, which is the lower limit of the present THz-TDS setup. For both barium titanate and BT:ST:BZ 2:1:1 compositions, the transmission at 100 GHz began~ 1% indicating that the primary band gap indeed lay below the 100 GHz detection limit and a remnant band structure was being detected. In order to obtain reliable data below 100 GHz the present THZ-TDS setup needs to be suitably modified. The THz-TDS setup is capable of measuring transmissions as low as 20 GHz based on decreasing the distance between transmission lines on the transmitter and receiver chips used to generate and detect THz pulses. This modification is intended for future measurements.

| Lattice | Band edge $f_{low}$ Actual/Predicted | Band edge $f_{high}$ Actual/Predicted | Transmission | $\Delta f_{mid}$% |
|---|---|---|---|---|
| Barium zirconate A | 180/200 | 330/330 | 1%/0.5% | 4.34% |
| Barium Zirconate B | 236/238 | 344/319 | 0.16%/0.07% | 3.96% |
| BT:ST:BZ 1:2:3 | 133/129 | 288/320 | 1%/0.1% | 6.65% |
| Strontium Titanate | ~100/77 | 188/127 | 0.1%/0.09% | NA |
| Barium titanate | <100/~45 | <100/~45 | Not modeled | NA |
| BT:ST:BZ 2:1:1 | <100/<100 | <100/<100 | Not modeled | NA |

Table 5.2 Summary of predicted and actual band edges and transmission minima measured for photonic crystals composed of varying compositions

Table 5.2 shows the comparison between features of actual and predicted primary band gap edges observed for the photonic lattices fabricated using robocasting. For the lower permittivity compositions (BZ and BT: ST: BZ) it was observed that the predicted mid gap frequency for primary band gap was within 7% of the actual experimentally measured value. The modeling method used a static value of relative permittivity and loss. Materials such as GaAs, which could possibly be used to develop photonic crystals operating in the optical regime, possess a low, almost frequency independent permittivity and negligible loss ($e_r$=13, $e_i$= $10^{-4}$).[17] However, perovskite mixtures studied in this thesis possess substantially high and frequency dependent permittivity and loss values. For e.g. the barium titanate composition showed almost 50% loss at 100 GHz. More accurate modeling of the photonic band structure may be accomplished by integrating the frequency dependant properties of the dielectric compositions into the TMM framework.

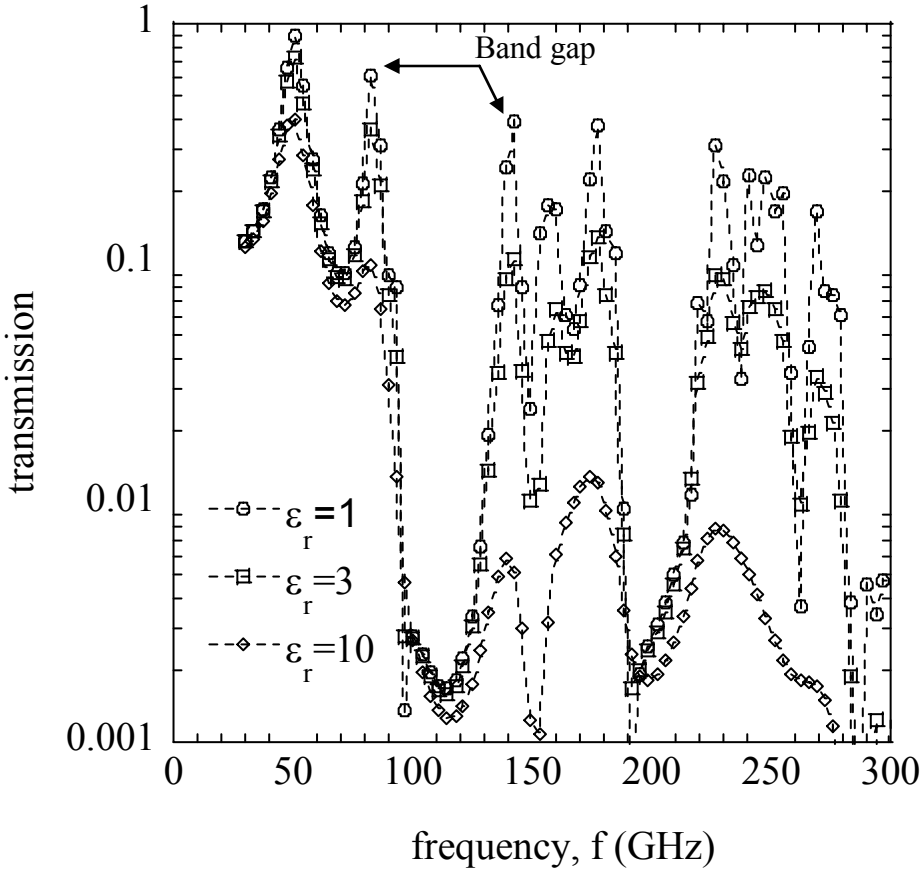


Figure 5.14 Simulated band structure for a lattice with $\varepsilon_r$=100 but with three different magnitudes for $\varepsilon_i$ at 1, 3, and 10 showing that an increase in loss leads to a decrease in transmission

To better understand the effect of increasing loss on the transmission spectra, modeling was done for a lattice with a=150 μm, d= 500 μm, c = 504 μm and a value of $\varepsilon_r$=100 but for varying $\varepsilon_i$ at 1, 3 and 10. These results are displayed in Figure 5.14. Two effects were observed as the $\varepsilon_i$ increased. First, while the lower bound for the primary band gap was unchanged, band structure at higher frequencies was different for varying

$\varepsilon_i$. Second, transmission across the entire frequency spectrum decreased as the loss increased. While the primary band edges for all three loss values coincided, transmission beyond the primary band gap was drastically reduced as the loss increased from ~40% for $\varepsilon_i$=1 to ~1% for $\varepsilon_i$=10 at 140 GHz. For PC's to serve as optical filters it is important that transmission should be attenuated only due to the interference of photons (i.e., existence of a band gap) and not from intrinsic material losses.

The effect of dielectric loss on photonic band gap behavior has also been discussed previously by Sigalas *et al.*,[17] who compared the simulated transmission for a 2-D photonic crystal composed of GaAs assuming both totally lossless and lossy transmission. This simulation reveals that the upper band edge of the primary band gap did not show a full recovery towards the pre-band edge transmission. These effects were also seen in the case of the perovskite photonic crystals where recovery was also partial and this could be attributed to the increasing loss mechanisms. Highest tunabilities are encountered near the curie point, however these are also regions of high loss.[81] It is recommended that other loss mechanisms should be studied in the perovskite structures and routes for transmission losses be eliminated in order to achieve higher transmissions. One factor for dielectric loss in barium titanate structures is the presence of oxygen vacancies.[81] The photonic crystals developed in this thesis were sintered in air, within a closed furnace, and it is suspected that this might have led to the introduction of oxygen vacancies within the compositions. A systematic study of the effect of using an open air furnace to an oxygen-rich controlled atmosphere during sintering must be conducted to understand the effect of sintering atmosphere on loss mechanisms. Another solution may be to replace the barium zirconate component with an alternative such as magnesium

titanate or magnesium oxide to reduce loss,[112, 113] while maintaining electro-optic tunability important towards development of tunable crystals.

## 5.5.Conclusions

Photonic crystal fabrication using multiple compositions composed of barium titanate, strontium titanate and barium zirconate were fabricated and tested for E.M transmission in the 100 GHz-1000 GHz range. The lower permittivity compositions showed a close match, within 10% of the predicted primary mid-gap frequency, with modeling done using the TMM method. It is, however, believed that using a frequency dependant permittivity and loss value will provide better predictive models especially in prediction of higher order band gaps. In the case of the high permittivity samples, the primary band gap lay below the detection limits of the instrument and it is recommended to suitably modify it to measure transmissions below 100 GHz. It was observed that material loss in the compositions contributed to transmission losses along with the presence of photonic band gaps. It is recommended that cause of material losses and alternative substituents should be studied to enable future developments of field tunable photonic crystals.

# 6. CONCLUSIONS AND RECOMMENDATIONS

Ternary mixtures of barium titanate (BT), strontium titanate (ST), and barium zirconate (BZ) were investigated as materials for three-dimensional, periodic, layer-by-layer structures used as photonic crystals. Highly concentrated aqueous-based ceramic gels were formulated using colloidal processing and printed using an extrusion based direct write technique called robocasting. Bulk films with a range of molar ratios were printed and their electrical characteristics determined at low frequencies to develop composition-properties maps. Based on this data, face centered tetragonal lattices were printed with varying compositions and their frequency dependent transmission spectra determined using Time Domain Terahertz Spectroscopy. The photonic band gaps found in the transmission were compared to those predicted by Transfer Matrix Method modeling of the photonic band structures and a very close match (within 10% of the primary mid-gap frequency) was found between the two. Systematic studies performed on the rheological, electrical, electro-optic, and photonic properties resulted in advances in the fields of direct write techniques, electronic materials, and photonic crystals as summarized below:

(1) Colloidal processing of barium titanate, strontium titanate and barium zirconate for direct write

(i) The effect of cationic valency of the salt in the flocculation of highly dispersed barium titanate slurries was compared. It was found that compared to monovalent cations, divalent cationic species were more effective flocculants and aided in generating gels suitable for robocasting due to the effect of bridging flocculation in addition to the ionic screening mechanism.

(ii) Similarly, a cationic polyelectrolyte, poly(ethylenimine) (PEI), was deemed an efficient flocculant due to a combination of ionic screening and bridging flocculation. The efficacy of flocculation increased with the molecular weight of the polyelectrolyte up to a threshold ($M_w$= 25,000) beyond which increasing the molecular weight of PEI had negligible effect on gel properties such as yield stress and shear modulus.

(iii) The gel recovery kinetics after a period of high shear were characterized by shear modulus measurements. The gel structure was found to recover via a two step recovery process: *i*) An instantaneous recovery (within 1-2 seconds) after cessation of shear and then *ii*) a gradual recovery (> 30 minutes) which could be modeled using an exponential decay model. The decay constant and ratio of initial modulus to final modulus was found to decrease with the concentration of PEI used, indicating a slower recovery and lower gain of the final modulus for stronger gels. This could be attributed to the relatively more compliant gel structure and the potential for more rapid structural rearrangement in weaker gels as compared to stronger ones.

(2) The dielectric properties of barium titanate: strontium titanate: barium zirconate mixtures were characterized for bulk films composed of these materials.

(i) Bulk film samples with systematically varying ratios of BT: ST: BZ ceramics were co-sintered to yield single phase solid solution perovskites and the dielectric constant was measured at a frequency of 100 KHz. It was found that increasing the ratio of $Sr^{2+}$:$Ba^{2+}$ and $Zr^{4+}$:$Ti^{4+}$ in the solid solution trended towards a decrease in the dielectric constant and dielectric loss tangent. For the former case a reduction in unit cell size, due to the smaller size of the $Sr^{2+}$ as compared to $Ba^{2+}$ caused a decrease in the dielectric function whereas in the latter case it was due to a decreased potential for the movement of the B site cation due to the larger size of $Zr^{4+}$ as compared to the $Ti^{4+}$. The dielectric constant for these compositions was found to range from ~26,000 (BT: BZ 7:1, 80°C) to ~25 (pure BZ, 80°C).

(ii) The Curie point ($T_c$) signifying the change from a tetragonal to cubic phase in the BT: ST: BZ composite lattice shifted to lower temperatures (from ~130°C for pure BT) as the ratio of ST+BZ: BT was increased. Curie-Weiss analysis was used to determine the Curie temperature ($\theta_c$) for these compositions and a linear relationship was found to exist between the $\theta_c$ and composition given by:

$\theta_c$ (°C) = 120.5- 318.12x  $Ba_{1-x}Sr_xTiO_3$ for $1<x< 0.67$  (6.1)

$\theta_c$ (°C) = 126.16- 418.96y  $BaZr_yTi_{1-y}O_3$ for $1<x< 0.50$  (6.2)

(iii) Tunabilities for the BT: ST: BZ composites were determined at 1 KHz, 25°C under a D.C. field bias of 1KV/mm. Tunabilities were found to decrease as the proportion of BT: ST+BZ decreased. While a BT: BZ 3:1 composite was found to be~67% tunable at ambient temperatures, compositions consisting mostly of BZ were found to be non-tunable. Highest Tunabilities were recorded for compositions for which the Curie Point was near the measurement temperature (25°C).

(3) Fabrication, assembly and characterization of photonic crystals composed of barium titanate: strontium titanate: barium zirconate mixtures

(i) Three dimensional periodic lattices with a range of compositions, consisting of BT, ST, BZ mixed in different molar ratios, were fabricated using robocasting. These lattices, having a face centered tetragonal symmetry, behaved as photonic crystals in the GHz regime showing photonic band gaps. For the low permittivity samples, the mid-gap frequency showed a close match, within 10%, to that predicted using Transfer Matrix Method modeling. Higher order band gaps, found at greater frequencies, deviated from prediction and this was attributed to the choice of a static dielectric constant and loss value chosen for the modeling technique.

(iii) For photonic crystals having high permittivity and tunability, the primary band gap shifted to sub-100 GHz range as predicted by the modeling. This was below the detection limit of the terahertz time domain spectroscopy device used to measure the transmission spectra. However, attenuated

transmission at 100 GHz indicated that the primary band gap indeed lay below the lower limit of the instrument. It is recommended to modify the apparatus to perform measurements below 100 GHz.

(iii) High permittivity samples also showed significantly high losses in the material which reduced the recovery in transmission beyond the band gaps. It is recommended to study and eliminate these losses in order to enhance the performance of these tunable photonic crystals. It is hypothesized that presence of oxygen vacancies led to increased losses and a study should be conducted to compare the effect of sintering furnace atmosphere on the dielectric properties for these compositions.

The work described in this thesis indicates that robocasting is a viable tool to test materials, methods and designs for fabrication of photonic crystals. In this work, a mixture of dielectrics was evaluated for its suitability towards fabrication of field tunable photonic crystals. It was found that this mixture had a variable permittivity based on the molar ratios of the constituting dielectric materials. Photonic crystals having tunability were fabricated, however it was discovered that these compositions had significant dielectric losses in the GHz-THz regime. These losses compete with the photonic band gap effect and lead to attenuation in transmitted signal. Hence, it is desirable to study loss mechanisms and minimize these to obtain functional photonic crystals. Inspite of the high losses, these crystals made using the robocasting process, could be modeled accurately using the transfer matrix method. This provided a validation of the fabrication process indicating the suitability of robocasting for fabricating photonic crystals. The modeling

technique also proved versatile in its ability to model lossy photonic crystals. Photonic crystals with such high losses are seldom fabricated however; in this case the loss accompanied the novel requirement of tunability in these compositions. Dielectric characterization of barium titanate, strontium titanate, and barium zirconate mixtures contributed important information about the dielectric characteristics such as permittivities, losses, tunabilities and Curie Temperatures. A new mechanism for development of colloidal gels using bridging flocculation between oppositely charged polyelectrolytes was studied and characterized. This mechanism can be extended to formulate robust inks of various particle systems other than those studied in this thesis. Gel structure recovery was studied and important information about the two step process towards structure recovery was obtained. In conclusion this thesis led to an increase in knowledge in multiple scientific and technological areas and provides a strong environment for future developments in the field of tunable photonic crystals.

## REFERENCES


1. Joannopoulos, J. D.; Meade, R. D.; Winn, J. N., *Photonic crystals : molding the flow of light*. Princeton University Press: Princeton, N.J., 1995; p ix, 137 p.

2. Joannopoulos, J. D.; University of California Berkeley. Dept. of Physics., The almost magical world of photonic crystals. In 1996.

3. Lin, S. Y.; Fleming, J. G.; Hetherington, D. L.; Smith, B. K.; Biswas, R.; Ho, K. M.; Sigalas, M. M.; Zubrzycki, W.; Kurtz, S. R.; Bur, J., A three-dimensional photonic crystal operating at infrared wavelengths. *Nature* **1998,** 394, (6690), 251-253.

4. Busch, K., *Photonic crystals : advances in design, fabrication, and characterization*. Wiley-VCH: Weinheim ; Cambridge, 2004; p xxvi, 354 p.

5. Joannopoulos, J. D.; Villeneuve, P. R.; Fan, S. H., Photonic crystals: Putting a new twist on light (vol 386, pg 143, 1997). *Nature* **1997,** 387, (6635), 830-830.

6. Clem, P. G.; Carroll, J. F., III; Niehaus, M. K.; Cesarano, J., III; Smay, J. E.; Lewis, J. A.; Lin, S.-Y., Materials for free-form fabrication of GHz tunable dielectric photonic crystals. *Materials Research Society Symposium Proceedings* **2003,** 758, (Rapid Prototyping Technologies), 41-46.

7. Pilleux, M. E.; Allahverdi, M.; Chen, Y. R.; Lu, K. C.; Jafari, M. A.; Safari, A., 3-D photonic bandgap structures in the microwave regime by fused deposition of multimaterials. *Rapid Prototyping Journal* **2002,** 8, (1), 46-52.

8. Smay, J. E.; Cesarano, J., III; Lin, S. Y.; Stuecker, J. N.; Lewis, J. A., Robocasting of photonic band gap structures. *Solid Freeform Fabrication Symposium Proceedings* **2001**, 175-178.

9. Smay, J. E.; Cesarano, J.; Lewis, J. A., Colloidal inks for directed assembly of 3-D periodic structures. *Langmuir* **2002,** 18, (14), 5429-5437.

10. Smay, J. E.; Gratson, G. M.; Shepherd, R. F.; Cesarano, J.; Lewis, J. A., Directed colloidal assembly of 3D periodic structures. *Advanced Materials* **2002,** 14, (18), 1279-+.

11. Yu, Z.; Ang, C.; Guo, R.; Bhalla, A. S., Dielectric properties and high tunability of Ba(Ti0.7Zr0.3)O-3 ceramics under dc electric field. *Applied Physics Letters* **2002,** 81, (7), 1285-1287.

12. Ho, K. M.; Chan, C. T.; Soukoulis, C. M.; Biswas, R.; Sigalas, M., Photonic Band-Gaps in 3-Dimensions - New Layer-by-Layer Periodic Structures. *Solid State Communications* **1994,** 89, (5), 413-416.

13. Busch, K., Tunable photonic crystals. *Advances in Solid State Physics* **2000,** 40, 529-543.

14. Lopez, C., Three-dimensional photonic bandgap materials: semiconductors for light. *Journal of Optics a-Pure and Applied Optics* **2006,** 8, (5), R1-R14.

15. Sigalas, M.; Soukoulis, C. M.; Economou, E. N.; Chan, C. T.; Ho, K. M., Photonic Band-Gaps and Defects in 2 Dimensions - Studies of the Transmission Coefficient. *Physical Review B* **1993,** 48, (19), 14121-14126.

16. Zhao, Y.; Grischkowsky, D., Terahertz demonstrations of effectively two-dimensional photonic bandgap structures. *Optics Letters* **2006,** 31, (10), 1534-1536.

17. Sigalas, M. M.; Soukoulis, C. M.; Chan, C. T.; Ho, K. M., Electromagnetic-Wave Propagation through Dispersive and Absorptive Photonic-Band-Gap Materials. *Physical Review B* **1994,** 49, (16), 11080-11087.

18. McCalmont, J. S.; Sigalas, M. M.; Tuttle, G.; Ho, K. M.; Soukolis, C. M., A layer-by-layer metallic photonic band-gap structure. *Applied Physics Letters* **1996,** 68, (19), 2759-2761.

19. Sigalas, M. M.; Chan, C. T.; Ho, K. M.; Soukoulis, C. M., Metallic Photonic Band-Gap Materials. *Physical Review B* **1995,** 52, (16), 11744-11751.

20. Pendry, J. B., Photonic Band Structures. *Journal of Modern Optics* **1994,** 41, (2), 209-229.

21. Pendry, J. B.; Mackinnon, A., Calculation of Photon Dispersion-Relations. *Physical Review Letters* **1992,** 69, (19), 2772-2775.

22. Fong, C. Y., *Topics in computational materials science*. World Scientific: Singapore ; River Edge, N.J., 1998; p xi, 382 p.

23. K. Umashankar, A. T., Computational Electromagnetics, Artech House, Boston. **1993**.

24. Markel*, V. A.; George, T. F., *Optics of nanostructured materials*. Wiley: New York, 2001; p x, 553 p.

25. Yee, K. S., IEEE Transactions on Antennas and Propagation. **1966,** 14.

26. Rancourt, J. D., *Optical thin films : user handbook*. SPIE Optical Engineering Press: Bellingham, Wash., 1996; p xii, 289 p.

27. Foresi, J. S.; Villeneuve, P. R.; Ferrera, J.; Thoen, E. R.; Steinmeyer, G.; Fan, S.; Joannopoulos, J. D.; Kimerling, L. C.; Smith, H. I.; Ippen, E. P., Photonic-bandgap microcavities in optical waveguides. *Nature* **1997,** 390, (6656), 143-145.

28. Yablonovitch, E.; Gmitter, T. J.; Leung, K. M., Photonic Band-Structure - the Face-Centered-Cubic Case Employing Nonspherical Atoms. *Physical Review Letters* **1991,** 67, (17), 2295-2298.

29. Feiertag, G.; Ehrfeld, W.; Freimuth, H.; Kolle, H.; Lehr, H.; Schmidt, M.; Sigalas, M. M.; Soukoulis, C. M.; Kiriakidis, G.; Pedersen, T.; Kuhl, J.; Koenig, W., Fabrication of photonic crystals by deep x-ray lithography. *Applied Physics Letters* **1997,** 71, (11), 1441-1443.

30. Noda, S.; Tomoda, K.; Yamamoto, N.; Chutinan, A., Full three-dimensional photonic bandgap crystals at near-infrared wavelengths. *Science* **2000,** 289, (5479), 604-606.

31. Sharp, D. N.; Campbell, M.; Dedman, E. R.; Harrison, M. T.; Denning, R. G.; Turberfield, A. J., Photonic crystals for the visible spectrum by holographic lithography. *Optical and Quantum Electronics* **2002,** 34, (1-3), 3-12.

32. Norris, D. J.; Vlasov, Y. A., Chemical approaches to three-dimensional semiconductor photonic crystals. *Advanced Materials* **2001,** 13, (6), 371-376.

33. Vlasov, Y. A.; Yao, N.; Norris, D. J., Synthesis of photonic crystals for optical wavelengths from semiconductor quantum dots. *Advanced Materials* **1999,** 11, (2), 165-169.

34. Braun, P. V.; Wiltzius, P., Microporous materials - Electrochemically grown photonic crystals. *Nature* **1999,** 402, (6762), 603-604.

35. Blanco, A.; Chomski, E.; Grabtchak, S.; Ibisate, M.; John, S.; Leonard, S. W.; Lopez, C.; Meseguer, F.; Miguez, H.; Mondia, J. P.; Ozin, G. A.; Toader, O.; van Driel, H. M., Large-scale synthesis of a silicon photonic crystal with a complete three-dimensional bandgap near 1.5 micrometres. *Nature* **2000,** 405, (6785), 437-440.

36. Miguez, H.; Meseguer, F.; Lopez, C.; Holgado, M.; Andreasen, G.; Mifsud, A.; Fornes, V., Germanium FCC structure from a colloidal crystal template. *Langmuir* **2000,** 16, (10), 4405-4408.

37. Busch, K.; John, S., Liquid-crystal photonic-band-gap materials: The tunable electromagnetic vacuum. *Physical Review Letters* **1999,** 83, (5), 967-970.

38. Kim, S.; Gopalan, V., Strain-tunable photonic band gap crystals. *Applied Physics Letters* **2001,** 78, (20), 3015-3017.

39. Li, B.; Zhou, J.; Li, L.; Wang, X. J.; Liu, X. H.; Jian, Z., Ferroelectric inverse opals with electrically tunable photonic band gap. *Applied Physics Letters* **2003,** 83, (23), 4704-4706.

40. Saado, Y.; Golosovsky, M.; Davidov, D.; Frenkel, A., Tunable photonic band gap in self-assembled clusters of floating magnetic particles. *Physical Review B* **2002,** 66, (19), -.

41. Kubo, S.; Gu, Z.-Z.; Takahashi, K.; Fujishima, A.; Segawa, H.; Sato, O., Tunable

Photonic Band Gap Crystals Based on a Liquid Crystal-Infiltrated Inverse Opal Structure. *Journal of the American Chemical Society* **2004,** 126, (26), 8314-8319.

42. Calvert, P.; Crockett, R., Chemical solid free-form fabrication: Making shapes without molds. *Chemistry of Materials* **1997,** 9, (3), 650-663.

43. Nelson, J. C.; Vail, N. K.; Barlow, J. W.; Beaman, J. J.; Bourell, D. L.; Marcus, H. L., Selective Laser Sintering of Polymer-Coated Silicon-Carbide Powders. *Industrial & Engineering Chemistry Research* **1995,** 34, (5), 1641-1651.

44. Nelson, J. C.; Xue, S.; Barlow, J. W.; Beaman, J. J.; Marcus, H. L.; Bourell, D. L., Model of the Selective Laser Sintering of Bisphenol-a Polycarbonate. *Industrial & Engineering Chemistry Research* **1993,** 32, (10), 2305-2317.

45. Marcus, H. L.; Beaman, J. J.; Barlow, J. W.; Bourell, D. L., Solid Freeform Fabrication - Powder Processing. *American Ceramic Society Bulletin* **1990,** 69, (6), 1030-1031.

46. Sachs, E.; Cima, M.; Williams, P.; Brancazio, D.; Cornie, J., 3-Dimensional Printing - Rapid Tooling and Prototypes Directly from a Cad Model. *Journal of Engineering for Industry-Transactions of the Asme* **1992,** 114, (4), 481-488.

47. Greul, M.; Pintat, T.; Greulich, M., Rapid prototyping of functional metallic parts. *Computers in Industry* **1995,** 28, (1), 23-28.

48. Gray, R. W.; Baird, D. G.; Bohn, J. H., Thermoplastic composites reinforced with long fiber thermotropic liquid crystalline polymers for fused deposition modeling. *Polymer Composites* **1998,** 19, (4), 383-394.

49. Kulkarni, P.; Dutta, D., Deposition strategies and resulting part stiffnesses in fused deposition modeling. *Journal of Manufacturing Science and Engineering-Transactions of the Asme* **1999,** 121, (1), 93-103.

50. Ziemian, C. W.; Crawn, P. M., Computer aided decision support for fused deposition modeling. *Rapid Prototyping Journal* **2001,** 7, (3), 138-147.

51. Zein, I.; Hutmacher, D. W.; Tan, K. C.; Teoh, S. H., Fused deposition modeling of novel scaffold architectures for tissue engineering applications. *Biomaterials* **2002,** 23,

(4), 1169-1185.

52. Wu, G. H.; Langrana, N. A.; Sadanji, R.; Danforth, S., Solid freeform fabrication of metal components using fused deposition of metals. *Materials & Design* **2002,** 23, (1), 97-105.

53. Evans, J. R. G., Direct ink jet printing of ceramics: experiment in teleology. *British Ceramic Transactions* **2001,** 100, (3), 124-128.

54. Cheng, C. C.; ArbetEngels, V.; Scherer, A.; Yablonovitch, E., Nanofabricated three dimensional photonic crystals operating at optical wavelengths. *Physica Scripta* **1996,** T68, 17-20.

55. Stuecker, J. N.; Miller, J. E.; Ferrizz, R. E.; Mudd, J. E.; Cesarano, J., Advanced support structures for enhanced catalytic activity. *Industrial & Engineering Chemistry Research* **2004,** 43, (1), 51-55.

56. Stuecker, J. N.; Cesarano, J.; Hirschfeld, D. A., Control of the viscous behavior of highly concentrated mullite suspensions for robocasting. *Journal of Materials Processing Technology* **2003,** 142, (2), 318-325.

57. Smay, J. E.; Cesarano, J.; Tuttle, B. A.; Lewis, J. A., Directed colloidal assembly of linear and annular lead zirconate titanate arrays. *Journal of the American Ceramic Society* **2004,** 87, (2), 293-295.

58. Li, Q.; Lewis, J. A., Nanoparticle inks for directed assembly of three-dimensional periodic structures. *Advanced Materials* **2003,** 15, (19), 1639-+.

59. Tuttle, B. A.; Smay, J. E.; Cesarano, J.; Voigt, J. A.; Scofield, T. W.; Olson, W. R.; Lewis, J. A., Robocast Pb(Zr0.95Ti0.05)O-3 ceramic monoliths and composites. *Journal of the American Ceramic Society* **2001,** 84, (4), 872-874.

60. Channell, G.; Zukoski, C., Shear and compressive rheology of aggregated alumina suspensions. *AICHE JOURNAL* **1997,** 43, (7), 1700-1708.

61. Smay, J. E.; Lewis, J. A., Structural and property evolution of aqueous-based lead zirconate titanate tape-cast layers. *Journal of the American Ceramic Society* **2001,** 84, (11), 2495-2500.

62. Tuttle, B. A.; Smay, J. E.; Cesarano, J., III; Voigt, J. A.; Scofield, T. W.; Olson, W. R.; Lewis, J. A., Robocast Pb(Zr0.95Ti0.05)O3 ceramic monoliths and composites. *Journal of the American Ceramic Society* **2001,** 84, (4), 872-874.

63. Smay, J. E.; Cesarano, J.; Tuttle, B. A.; Lewis, J. A., Piezoelectric properties of 3-X periodic Pb(ZrxTi1-x)O-3-polymer composites. *Journal of Applied Physics* **2002,** 92, (10), 6119-6127.

64. Williams, D.; Tuttle, B.; Cesarano, J., III; Rodriguez, M., Robocast high zirconia content (Pb,La,Zr,Ti)O3 dielectrics. *Proceedings - Electrochemical Society* **2004,** 2003-27, 191-199.

65. Nadkarni, S. S.; Smay, J. E., Concentrated barium titanate colloidal gels prepared by bridging flocculation for use in solid freeform fabrication. *Journal of the American Ceramic Society* **2006,** 89, (1), 96-103.

66. Cesarano, J., III; Baer, T. A., Recent developments in free-form fabrication of dense ceramics from slurry deposition. *Solid Freeform Fabrication Symposium Proceedings* **1997,** 1, 25-32.

67. Cesarano, J., III; King, B. H.; Denham, H. B., Recent developments in robocasting of ceramics and multimaterial deposition. *Solid Freeform Fabrication Symposium Proceedings* **1998**, 697-703.

68. Denham, H. B.; Cesarano, J., III; King, B. H.; Calvert, P., Mechanical behavior of robocast alumina. *Solid Freeform Fabrication Symposium Proceedings* **1998**, 589-596.

69. He, G.; Hirschfeld, D. A.; Cesarano, J., III, Processing and mechanical properties of silicon nitride formed by robocasting aqueous slurries. *Ceramic Engineering and Science Proceedings* **2000,** 21, (4, 24th Annual Conference on Composites, Advanced Ceramics, Materials, and Structures: B, 2000), 607-614.

70. He, G.; Hirschfeld, D. A.; Cesarano, J., III; Stuecker, J. N., Processing of silicon nitride-tungsten prototypes. *Ceramic Transactions* **2001,** 114, (Functionally Graded Materials 2000), 325-332.

71. He, G.; Hirschfeld, D. A.; Cesarano, J., III; Stuecker, J. N., Robocasting and cofiring of functionally graded Si3N4-W materials. *Ceramic Engineering and Science*

*Proceedings* **2001,** 22, (4, 25th Annual Conference on Composites, Advanced Ceramics, Materials, and Structures: B, 2001), 119-125.

72. Corral, E. L.; Cesarano, J., III; Stuecker, J. N.; Barrera, E. V., Processing of carbon nanofiber reinforced silicon nitride matrix composites. *Rapid Prototyping of Materials, Proceedings of [a] Symposium, Columbus, OH, United States, Oct. 7-10, 2002* **2002**, 53-62.

73. Zhu, Q.; De With, G.; Dortmans, L. J. M. G.; Feenstra, F., Mechanical properties of alumina-glass dental composites. *Key Engineering Materials* **2002,** 206-213, (Pt. 3, Euro Ceramics VII), 1603-1606.

74. Cesarano, J., III; Dellinger, J. G.; Saavedra, M. P.; Gill, D. D.; Jamison, R. D.; Grosser, B. A.; Sinn-Hanlon, J. M.; Goldwasser, M. S., Customization of load-bearing hydroxyapatite lattice scaffolds. *International Journal of Applied Ceramic Technology* **2005,** 2, (3), 212-220.

75. Miranda, P.; Saiz, E.; Gryn, K.; Tomsia Antoni, P., Sintering and robocasting of beta-tricalcium phosphate scaffolds for orthopaedic applications. *Acta biomaterialia* **2006,** 2, (4), 457-66.

76. Stuecker, J. N.; Cesarano, J., III; Miller, J. E.; Ferrizz, R. M.; Mudd, J. E., Novel three-dimensional ceramic lattices as catalyst supports and diesel particulate traps. *Society of Automotive Engineers, [Special Publication] SP* **2003,** SP-1755, (Diesel Emission Measurement and Modeling), 125-129.

77. Ferrizz, R. M.; Stuecker, J. N.; Cesarano, J., III; Miller, J. E., Monolithic Supports with Unique Geometries and Enhanced Mass Transfer. *Industrial & Engineering Chemistry Research* **2005,** 44, (2), 302-308.

78. Gratson, G. M.; Xu, M. J.; Lewis, J. A., Microporiodis structures - Direct writing of three-dimensional webs. *Nature* **2004,** 428, (6981), 386-386.

79. Gratson, G. M.; Garcia-Santamaria, F.; Lousse, V.; Xu, M. J.; Fan, S. H.; Lewis, J. A.; Braun, P. V., Direct-write assembly of three-dimensional photonic crystals: Conversion of polymer scaffolds to silicon hollow-woodpile structures. *Advanced Materials* **2006,** 18, (4), 461-+.

80. Chen, Y.; Bartzos, D.; Lu, Y.; Niver, E.; Pilleux, M. E.; Allahverdi, M.; Danforth, S. C.; Safari, A., Simulation, fabrication, and characterization of 3-D alumina photonic bandgap structures. *Microwave and Optical Technology Letters* **2001,** 30, (5), 305-307.

81. Moulson, A. J.; Herbert, J. M., *Electroceramics : materials, properties, applications*. Chapman and Hall: London ; New York, 1990; p xii, 464 p.

82. Pervez, N. K.; Hansen, P. J.; York, R. A., High tunability barium strontium titanate thin films for rf circuit applications. *Applied Physics Letters* **2004,** 85, (19), 4451-4453.

83. Lee, S.-J.; Moon, S. E.; Kwak, M.-H.; Ryu, H.-C.; Kim, Y.-T.; Kang, K.-Y., High dielectric tunability of (Ba, Sr)TiO3 thin films and their coplanar waveguide phase shifter applications. *Japanese Journal of Applied Physics, Part 1: Regular Papers, Short Notes & Review Papers* **2004,** 43, (9B), 6750-6754.

84. Wang, C.; Cheng, B. L.; Wang, S. Y.; Lu, H. B.; Zhou, Y. L.; Chen, Z. H.; Yang, G. Z., Improved dielectric properties and tunability of multilayered thin films of (Ba0.80Sr0.20)(Ti1-xZrx)O3 with compositionally graded layer. *Applied Physics Letters* **2004,** 84, (5), 765-767.

85. Manavalan, S. G.; Kumar, A.; Weller, T.; Sikder, A. K., Structural and electrical properties of Ba0.5Sr0.5TiO3 thin films for tunable microwave applications. *Materials Research Society Symposium Proceedings* **2004,** 811, (Integration of Advanced Micro- and Nanoelectronic Devices--Critical Issues and Solutions), 411-418.

86. Kageyama, K.; Takahashi, J., Tunable microwave properties of barium titanate-based ferroelectric glass-ceramics. *Journal of the American Ceramic Society* **2004,** 87, (8), 1602-1605.

87. Zimmermann, F.; Voigts, M.; Menesklou, W.; Ivers-Tiffee, E., Ba0.6Sr0.4TiO3 and BaZr0.3Ti0.7O3 thick films as tunable microwave dielectrics. *Journal of the European Ceramic Society* **2004,** 24, (6), 1729-1733.

88. Agrawal, S.; Manuspiya, H.; Guo, R.; Agrawal, D.; Bhalla, A. S., Dielectric tunability of microwave sintered BST:MgO composites. *Ceramic Transactions* **2004,** 150, (Ceramic Materials and Multilayer Electronic Devices), 299-306.

89. Jain, M.; Majumder, S. B.; Katiyar, R. S.; Bhalla, A. S., Novel barium strontium titanate Ba0.5Sr0.5TiO3/MgO thin film composites for tunable microwave devices. *Materials Letters* **2003,** 57, (26-27), 4232-4236.

90. Xie, Y.-H.; Lin, Y.-Y.; Tang, T.-A., Characteristics of BST Thin Film Prepared by Novel Chemical Solution Deposition Method for High-Density DRAM Application. *Integrated Ferroelectrics* **2002,** 47, 113-124.

91. Fitsilis, F. *MOCVD of high-K ceramic thin films for the Gbit DRAM technology*; Germany.: 2002; pp i-ii, 1-135.

92. Tomokiyo, Y.; Doira, K.; Tanaka, E.; Kuroiwa, T., Microstructures of dielectric BaxSr1-xTiO3 prepared by RF sputtering. *Materia* **2001,** 40, (12), 1015.

93. Hwang, C. S., Metal-organic chemical vapor deposition of high dielectric (Ba,Sr)TiO3 thin films for dynamic random access memory applications. *Surface Engineering Series* **2001,** 2, (Chemical Vapor Deposition), 205-241.

94. Stemmer, S.; Streiffer, S. K.; Browning, N. D.; Kingon, A. I., Microstructure and nonstoichiometry of barium strontium titanate thin films for DRAM applications. *Materials Research Society Symposium Proceedings* **1999,** 574, (Multicomponent Oxide Films for Electronics), 119-124.

95. Beitel, G.; Wendt, H.; Fritsch, E.; Weinrich, V.; Engelhardt, M.; Hasler, B.; Rohr, T.; Bergmann, R.; Scheler, U.; Malek, K. H.; Nagel, N.; Gschwandtner, A.; Pamler, W.; Honlein, W.; Dehm, C.; Mazure, C., A novel low-temperature (Ba,Sr)TiO3 (BST) process with Ti/TiN barrier for Gbit DRAM applications. *Microelectronic Engineering* **1999,** 48, (1-4), 299-302.

96. Hieda, K.; Eguchi, K.; Fukushima, N.; Aoyama, T.; Natori, K.; Kiyotoshi, M.; Yamazaki, S.; Izuha, M.; Niwa, S.; Fukuzumi, Y.; Ishibashi, Y.; Kohyama, Y.; Arikado, T.; Okumura, K., All Perovskite Capacitor (APEC) technology for (Ba, Sr)TiO3 Capacitor scaling toward 0.10mm stacked DRAMs. *Technical Digest - International Electron Devices Meeting* **1998**, 807-810.

97. Colombo, L.; Visokay, M. R.; Okuno, Y.; Khamankar, R.; Kressley, M.; Summerfelt, S.; Moise, T., High-K dielectric materials for memory devices. *Ceramic Transactions* **1998,** 86, (Integrated Thin Films and Applications), 31-40.

98. Joshi, P. C.; Tandon, R. P.; Mansingh, A., Barium strontium titanate thin films by metalorganic solution deposition technique for dynamic random access memory (DRAM) applications. *Ferroelectrics* **1997,** 197, (1-4), 775-779.

99. Vendik, O. G., Microwave Tunable Components and Subsystems Based on Ferroelectrics: Physics and Principles of Design. *Integrated Ferroelectrics* **2002,** 49, 181-190.

100. Wu, L.; Wu, S.; Chang, F.-C.; Shen, Y.-T.; Chen, Y.-C., DC field dependence of dielectric constant and loss factor of Al2O3-doped barium strontium titanate for application in phased array antennas. *Journal of Materials Science* **2000,** 35, (23), 5945-5950.

101. Chen, Y. C.; Wu, L.; Chou, Y. P.; Tsai, Y. T., Curve-fitting of direct-current field dependence of dielectric constant and loss factor of Al2O3-doped barium strontium titanate. *Materials Science & Engineering, B: Solid-State Materials for Advanced Technology* **2000,** B76, (2), 95-100.

102. Rao, J. B. L.; Patel, D. P.; Sengupta, L. C., Phased array antennas based on bulk phase shifting with ferroelectrics. *Integrated Ferroelectrics* **1998,** 22, (1-4), 307-316.

103. Sengupta, L. C.; Ngo, E.; Sengupta, S.; Stowell, S., Multi-process synthesis of novel ferroelectric oxide ceramic composites for use in phase array antennas. *Army Science Conference: Award Winning Papers, 20th, Norfolk, Va., June 24-27, 1996* **1997**, 126-134.

104. Koutsaroff, I. P.; Bernacki, T. A.; Zelner, M.; Cervin-Lawry, A.; Jimbo, T.; Suu, K., Characterization of thin-film decoupling and high-frequency (Ba,Sr)TiO3 capacitors on Al2O3 ceramic substrates. *Japanese Journal of Applied Physics, Part 1: Regular Papers, Short Notes & Review Papers* **2004,** 43, (9B), 6740-6745.

105. Kurihara, K.; Shioga, T.; Baniecki, J. D., Electrical properties of low-inductance barium strontium titanate thin film decoupling capacitors. *Journal of the European Ceramic Society* **2004,** 24, (6), 1873-1876.

106. Niwa, K.; Shioga, T.; Baniecki, J. D.; Kurihara, K., Low-inductance barium strontium titanate thin film capacitors for decoupling applications. *Ceramic Transactions* **2003,** 136, (Morphotropic Phase Boundary Pervskites, High Strain Piezoelectrics, and Dielectric Ceramics), 317-326.

107. Imanaka, Y.; Shioga, T.; Baniecki, J. D., Decoupling capacitor with low inductance for high-frequency digital applications. *Fujitsu Scientific & Technical Journal* **2002,** 38, (1), 22-30.

108. Kozyrev, A.; Buslov, O.; Keis, V.; Dovgan, D.; Kotelnikov, I.; Kulik, P.; Sengupta, L.; Chiu, L.; Zhang, X., 14 GHz tunable filters base on ferroelectric films. *Integrated Ferroelectrics* **2003,** 55, 905-913.

109. Abdelkefi, H.; Khemakhem, H.; Velu, G.; Carru, J. C.; Von der Muhll, R., Dielectric properties and ferroelectric phase transitions in BaxSr1-xTiO3 solid solution. *Journal of Alloys and Compounds* **2005,** 399, (1-2), 1-6.

110. Ravez, J.; Simon, A., Temperature and frequency dielectric response of ferroelectric ceramics with composition Ba(Ti1-xZrx)O-3. *European Journal of Solid State and Inorganic Chemistry* **1997,** 34, (11), 1199-1209.

111. Zhai, J. W.; Yao, X.; Zhang, L. Y.; Shen, B.; Chen, H., Orientation control and dielectric properties of sol-gel deposited Ba (Ti, Zr)O-3 thin films. *Journal of Crystal Growth* **2004,** 262, (1-4), 341-347.

112. Synowczynski, J.; Sengupta, L. C.; Chiu, L. H., Investigation of the effect of particle size on the 10 GHz microwave properties of Ba1-xSrxTiO3/MgO composite ceramics. *Integrated Ferroelectrics* **1998,** 22, (1-4), 861-872.

113. Alberta, E. F.; Guo, R.; Bhalla, A. S., Novel BST : MgTiO3 composites for frequency agile applications. *Ferroelectrics* **2002,** 268, 589-594.

114. Piqué, A.; Chrisey, D. B., *Direct-write technologies for rapid prototyping applications : sensors, electronics, and integrated power sources*. Academic Press: San Diego, 2002; p xxvi, 726 p.

115. Liu, X. G.; Fu, L.; Hong, S. H.; Dravid, V. P.; Mirkin, C. A., Arrays of magnetic nanoparticles patterned via "dip-pen" nanolithography. *Advanced Materials* **2002,** 14, (3), 231-234.

116. Melngailis, J., Focused Ion-Beam Technology and Applications. *Journal of Vacuum Science & Technology B* **1987,** 5, (2), 469-495.

117. Matson, D. W.; Martin, P. M.; Bennett, W. D., Laser machined components for microanalytical and chemical separation devices. *Proceedings of SPIE-The International Society for Optical Engineering* **1998,** 3519, (Microrobotics and Micromanipulation), 200-207.

118. Cesarano, J. I., Segalman Rachel, Calvert, Paul Robocasting provides moldless fabrication from slurry deposition. *Ceramic Industry* **1998,** 148, (4), 94-101.

119. Song, J. H.; Edirisinghe, M. J.; Evans, J. R. G., Formulation and multilayer jet printing of ceramic inks. *Journal of the American Ceramic Society* **1999,** 82, (12), 3374-3380.

120. Seerden, K. A. M.; Reis, N.; Evans, J. R. G.; Grant, P. S.; Halloran, J. W.; Derby, B., Ink-jet printing of wax-based alumina suspensions. *Journal of the American Ceramic Society* **2001,** 84, (11), 2514-2520.

121. Morissette, S. L.; Lewis, J. A.; Clem, P. G.; Cesarano, J.; Dimos, D. B., Direct-write fabrication of Pb(Nb,Zr,Ti)O(3 d)evices: Influence of paste rheology on print morphology and component properties. *Journal of the American Ceramic Society* **2001,** 84, (11), 2462-2468.

122. Guo, J. J.; Lewis, J. A., Aggregation effects on the compressive flow properties and drying behavior of colloidal silica suspensions. *Journal of the American Ceramic Society* **1999,** 82, (9), 2345-2358.

123. Shen, Z.-G.; Chen, J.-F.; Zou, H.-k.; Yun, J., Dispersion of nanosized aqueous suspensions of barium titanate with ammonium polyacrylate. *Journal of Colloid and Interface Science* **2004,** 275, (1), 158-164.

124. Paik, U.; Lee, S.; Hackley, V. A., Influence of barium dissolution on the electrokinetic properties of colloidal BaTiO3 in an aqueous medium. *Journal of the American Ceramic Society* **2003,** 86, (10), 1662-1668.

125. Chiang, C.-W.; Jean, J.-H., Effects of barium dissolution on dispersing aqueous barium titanate suspensions. *Materials Chemistry and Physics* **2003,** 80, (3), 647-655.

126. Chiang, C.-W.; Jean, J.-H., Effects of barium dissolution on dispersing aqueous barium titanate suspensions. *Dielectric Materials and Devices, [Proceedings of the*

*Advances in Dielectric Materials and Multilayer Electronic Devices Symposium at the 102nd Annual Meeting of the American Ceramic Society], St. Louis, MO, United States, Apr. 30-May. 3, 2000* **2002**, 247-255.

127. Larson, R. G., *The structure and rheology of complex fluids*. Oxford University Press: New York, 1999; p xxi, 663 p.

128. Kirby, G. H.; Harris, D. J.; Li, Q.; Lewis, J. A., Poly(acrylic acid)-poly(ethylene oxide) comb polymer effects on BaTiO3 nanoparticle suspension stability. *Journal of the American Ceramic Society* **2004,** 87, (2), 181-186.

129. Hunter, R. J., *Foundations of colloid science*. Clarendon Press.: 1991; p 2 v.

130. Poptoshev, E.; Claesson, P. M., Forces between glass surfaces in aqueous polyethylenimine solutions. *Langmuir* **2002,** 18, (7), 2590-2594.

131. Kotov, N. A.; Mamedov, A. A.; Guldi, D. M.; Prato, M.; Wicksted, J.; Hirsch, A., Designing ultra-strong composites by layer-by-layer assembly. *Polymeric Materials Science and Engineering* **2004,** 90, 325.

132. von Harpe, A.; Petersen, H.; Li, Y.; Kissel, T., Characterization of commercially available and synthesized polyethylenimines for gene delivery. *Journal of Controlled Release* **2000,** 69, (2), 309.

133. Nowak, A. P.; Breedveld, V.; Pakstis, L.; Ozbas, B.; Pine, D. J.; Pochan, D.; Deming, T. J., Rapidly recovering hydrogel scaffolds from self-assembling diblock copolypeptide amphiphiles. *Nature* **2002,** 417, (6887), 424-428.

134. Rueb, C.; Zukoski, C., Viscoelastic properties of colloidal gels. *Journal of Rheology* **1997,** 41, (2), 197-218.

135. Zurcher, P.; Tracy, C. J.; Jones, R. E., Jr.; Alluri, P.; Chu, P. Y.; Jiang, B.; Kim, M.; Melnick, B. M.; Raymond, M. V.; Roberts, D.; Remmel, T. P.; Tsai, T. L.; White, B. E.; Zafar, S.; Gillespie, S. J., Barium strontium titanate capacitors for embedded DRAM. *Materials Research Society Symposium Proceedings* **1999,** 541, (Ferroelectric Thin Films VII), 11-22.

136. Kotecki, D. E.; Baniecki, J. D.; Shen, H.; Laibowitz, R. B.; Saenger, K. L.; Lian,

J. J.; Shaw, T. M.; Athavale, S. D.; Cabral, C., Jr.; Duncombe, P. R.; Gutsche, M.; Kunkel, G.; Park, Y. J.; Wang, Y. Y.; Wise, R., (Ba,Sr)TiO3 dielectrics for future stacked-capacitor DRAM. *IBM Journal of Research and Development* **1999,** 43, (3), 367-382.

137. Huang, S.-c.; Chen, H.-m.; Wu, S. C.; Ya-min Lee, J., Time dependent dielectric breakdown of paraelectric barium-strontium-titanate thin film capacitors for memory device applications. *Journal of Applied Physics* **1998,** 84, (9), 5155-5157.

138. Jaffe, B.; Cook, W. R.; Jaffe, H. L., *Piezoelectric ceramics*. Academic Press: London, New York,, 1971; p ix, 317 p.

139. Zhang, L.; Zhong, W. L.; Peng, Y. P.; Wang, Y. G., A correlation between the ferroelectric phase transition and the cell volume in barium strontium titanate. *Acta Physica Sinica* **2000,** 49, (7), 1371-1376.

140. Zhang, L.; Zhong, W. L.; Wang, Y. G.; Zhang, P. L., The cell volume effect in barium strontium titanate. *Solid State Communications* **1997,** 104, (5), 263-266.

141. Alexandru, H. V.; Berbecaru, C.; Ioachim, A.; Toacsen, M. I.; Banciu, M. G.; Nedelcu, L.; Ghetu, D., Oxides ferroelectric (Ba, Sr)TiO3 for microwave devices. *Materials Science and Engineering B-Solid State Materials for Advanced Technology* **2004,** 109, (1-3), 152-159.

142. Ihlefeld, J. F.; Maria, J. P.; Borland, W., Dielectric and microstructural properties of barium titanate zirconate thin films on copper substrates. *Journal of Materials Research* **2005,** 20, (10), 2838-2844.

143. Dixit, A.; Majumder, S. B.; Dobal, P. S.; Katiyar, R. S.; Bhalla, A. S., Phase transition studies of sol-gel deposited barium zirconate titanate thin films. *Thin Solid Films* **2004,** 447, 284-288.

144. Tang, X. G.; Chew, K. H.; Chan, H. L. W., Diffuse phase transition and dielectric tunability of Ba(ZryTi1-y)O-3 relaxor ferroelectric ceramics. *Acta Materialia* **2004,** 52, (17), 5177-5183.

145. Hofer, C.; Hoffmann, M.; Boettger, U.; Waser, R., Relaxors as high-epsilon-materials for multilayer and thin film capacitors. *Ferroelectrics* **2002,** 270, 1365-1370.

146. Ravez, J.; Pouchard, M.; Hagenmuller, P., Chemical Bonding and Ferroelectric Perovskites. *European Journal of Solid State and Inorganic Chemistry* **1991,** 28, (5), 1107-1123.

147. Johnson, S. G.; Joannopoulos, J. D., *Photonic crystals : the road from theory to practice*. Kluwer Academic Publishers: Boston, 2002; p 156 p.

148. Lee, W. M.; Pruzinsky, S. A.; Braun, P. V., Multi-photon polymerization of waveguide structures within three-dimensional photonic crystals. *Advanced Materials* **2002,** 14, (4), 271-+.

149. Scrimgeour, J.; Sharp, D. N.; Blanford, C. F.; Roche, O. M.; Denning, R. G.; Turberfield, A. J., Three-dimensional optical lithography for photonic microstructures. *Advanced Materials* **2006,** 18, (12), 1557-+.

150. Ozbay, E.; Abeyta, A.; Tuttle, G.; Tringides, M.; Biswas, R.; Chan, C. T.; Soukoulis, C. M.; Ho, K. M., Measurement of a 3-Dimensional Photonic Band-Gap in a Crystal-Structure Made of Dielectric Rods. *Physical Review B* **1994,** 50, (3), 1945-1948.

151. Grischkowsky, D.; Keiding, S.; Vanexter, M.; Fattinger, C., Far-Infrared Time-Domain Spectroscopy with Terahertz Beams of Dielectrics and Semiconductors. *Journal of the Optical Society of America B-Optical Physics* **1990,** 7, (10), 2006-2015.

152. Hangyo, M.; Tani, M.; Nagashima, T., Terahertz time-domain spectroscopy of solids: A review. *International Journal of Infrared and Millimeter Waves* **2005,** 26, (12), 1661-1690.

# APPENDIX A: PRINTING OF A BARIUM TITANATE, STRONTIUM TITANATE AND BARIUM ZIRCONATE TERNARY ARRAY USING MULTI-MATERIAL DIRECT WRITE

## A.1. Introduction

Alloying of pure materials by forming a solid solution with a suitable solute is a common way to modify material characteristics from strength to electric, optic, and magnetic properties. For example, alloys of two or more metals can yield better strength (e.g. duralumin), chemical resistance (e.g. stainless steel) or in some cases aesthetic appeal (e.g. bronze). Of course, the extent of solid solution in these alloys is subject to atomic size and crystal structure limitations. The modification of properties may be due to interstitial substitution, lattice site substitution, or formation of a second phase. For ceramic applications, similar rules apply for the formation of substitutional solid solutions; however electron neutrality and substitution of cations on cation sites and anions on anion sites is paramount. For example, blending $SrTiO_3$ with $BaTiO_3$ can decrease the Curie Temperature or, alternatively, blending with lead zirconate can increase it.[138] The Curie temperature ($\theta_C$) itself may be calculated from first principles; however, experimental determination of electrical properties by combinatorial screening is a effective tool to discover compositions that lead to desired properties. Useful Figures of Merit are developed to identify regions of interest and further mixing and testing is

conducted to refine compositions to find the ideal blend for the specific application. For mixed oxide ceramics, sample preparation is often a tedious and time consuming step in the screening process since individual slurries must be formulated for each new composition. In this chapter the preliminary findings of the application of direct write[114] to combinatorial screening have been described. Using this method multiple compositions of ceramic mixtures, composed of ternary blends of barium titanate, strontium titanate and barium zirconate, were rapidly screened using the direct write method-robocasting[9, 10].

Stock inks of the pure ceramics were prepared and loaded into individual reservoirs and then co-extruded through a mixing chamber to form samples with desired compositions by controlling the flow rate ratios of the three inks through the deposition nozzles. Figure A.1 shows a schematic for the intended application where a binary and ternary array is displayed. Each apex in the ternary array represents the three pure ceramic compositions and along each side there is systematic variation in composition from pure component 1 to pure component 2, etc. The interior nodes represent ternary mixtures of the three pure components. Hence, if suitable pure inks are created, the entire composition range in the ternary space may be rapidly processed in a single ternary array printing experiment. The samples are discrete, and the composition step size can be adjusted to suit the experimenter's desires. Time consuming pre-mixing of samples is avoided and rapid screening of properties can be conducted after finishing operations. Some preliminary results of this combinatorial printing process have been described.

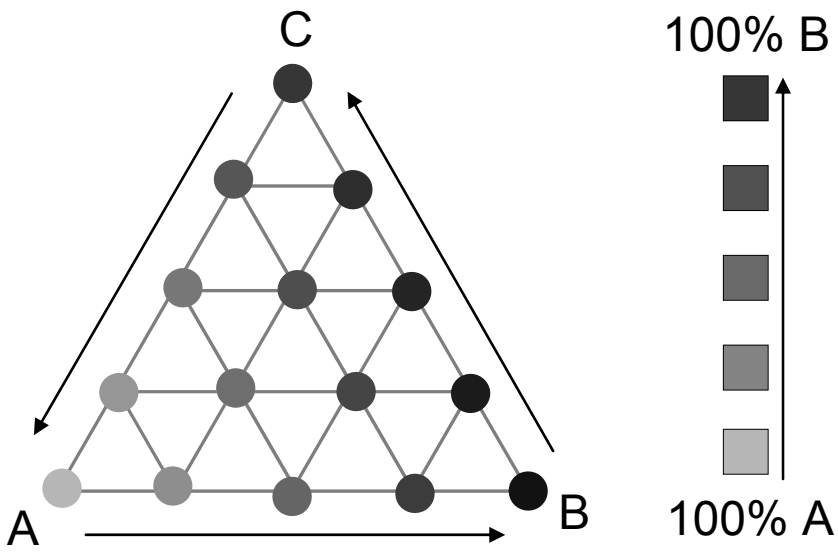


Figure A.1 An example of ternary and binary arrays of samples that can be printed using an extension of the robocasting technique to print multi-materials. Different colors represent different ratios of the three materials

## A.2. Experimental

### *A.2.1. Printing of a ternary array of barium titanate, strontium titanate and barium zirconate*

Aqueous stock inks of barium titanate (BT),[65] strontium titanate (ST) and barium zirconate (BZ) were prepared at 45% volume solids loading using techniques previously described in chapter 3. Inks were loaded into individual syringes and affixed to the modified robocasting device as shown in Figure A.2.

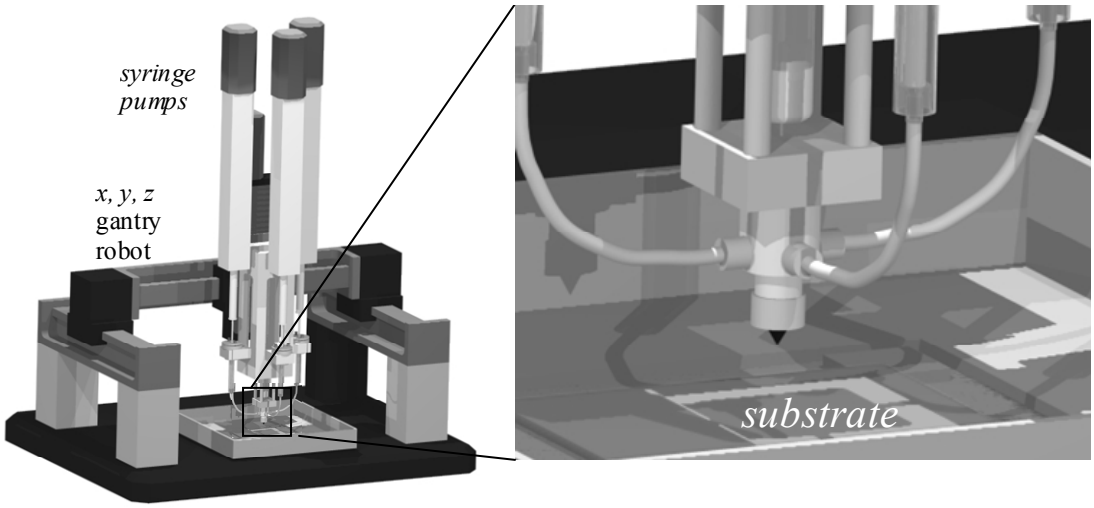


Figure A.2 Modification of the robocasting device for multi-material printing showing the mixing chamber

For the mixing chamber a special mixing assembly was designed to facilitate dynamic mixing of the three colloidal gels before extrusion. Figure A.3 shows a cross section of the mixing assembly. For clarity only two of the three ink streams have been displayed. The active mixing region is essentially a truncated cone with a paddle style agitator of diameter =1/32" flattened down to approximately 0.012". The calculated active mixing volume is ~ 30 nl.

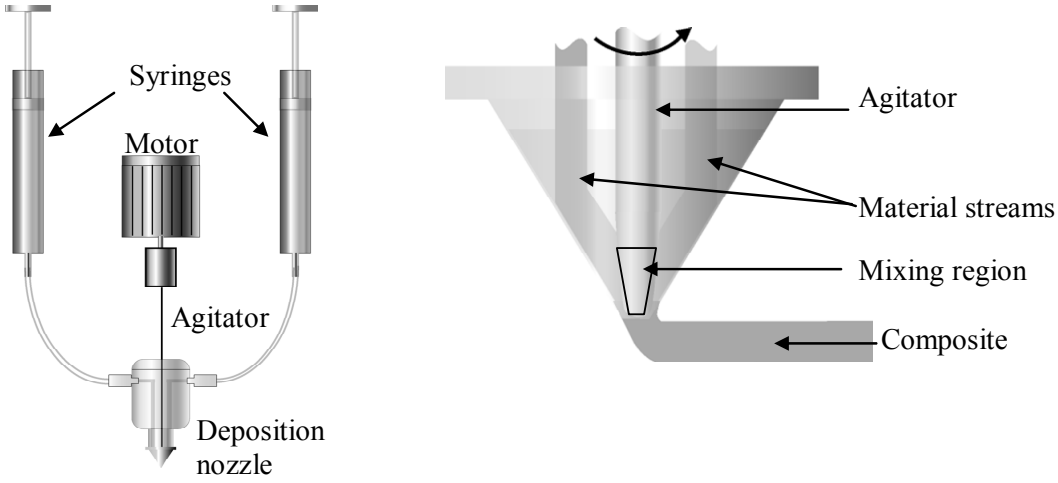


Figure A.3 Detail of the mixing chamber assembly. Separate colloidally gelled ink streams enter a common mixing chamber where they are mechanically agitated using a rotating paddle to produce a mixed extrudate

To produce ternary blends of BT, ST, and BZ a ternary array was written in the style as shown in Figure A.1. Positive displacement syringe pumps were used to push ink streams into the common mixing chamber before being co-extruded as a single filament onto the substrate or underlying layers. Agitator mixing speed was maintained at 300 rpm. Two layer, space filled cuboid samples having square cross sectional area of 5 mm X 5 mm were written at a linear speed of 5 mm/s through a conical nozzle having a bore of 450 μm. The simply calculated Reynold's Number (assuming no agitator action) for this system was ~ 0.004 (distance, D= 0.2 mm, velocity, V= 5mm/s, density, ρ= 3.3 g/cc and viscosity, μ = 800 Pa.s at a shear rate $\gamma = 10\ s^{-1}$) with an average residence time of 37.5 μs within the mixing chamber. The low Reynold's Number coupled with short residence time warranted the use of a mechanical mixing agitator to assist in blending of the inks. Samples were deposited on a flat alumina substrate immersed in oil. After

deposition, samples were removed from oil, dried in ambient air for 12 hours, bisque fired at 1100°C and examined using back scatter electron microscopy.

## A.3. Results and Discussions

### *A.3.1. Rheology*

To understand the effect of *in-situ* mixing on rheology of the ink blends, a comparison of two inks was done. To formulate the first ink, individual inks of BT, ST, and BZ were mixed in a 1:1:1 molar ratio and blended using a planetary mixer. For the second, an ink was formulated using a mixture of BT, ST, and BZ ceramic powders as described in chapter 3 and chapter 4. The shear modulus as a function of shear stress was determined for both inks. As shown in Figure A.4, the rheology of *in-situ* blended inks was similar to that of inks formed from pre-blending of ceramic powders. Both had a yield stress of $\tau_y$~ 110 Pa and a sufficiently high modulus of $G'_{eq}$~1.2X10$^5$ Pa. Mixing of individual inks did not adverse affect the rheology of inks and allowed for fabrication of 3-D patterns. This fortuitous circumstance arises from the fact that the surface chemistry of the constituents is similar in the aqueous environment. Each particle type adsorbs ammonium polyacrylate as a stabilizing layer and, hence, each can be flocculated with subsequent addition of poly(ethylenimine). The monolayer surface coverage for the three materials investigated here are slightly different, but if an excess of ammonium polyacrylate is added non-adsorbed species simply reside in the aqueous solution and are later complexed with the poly(ethylenimine).

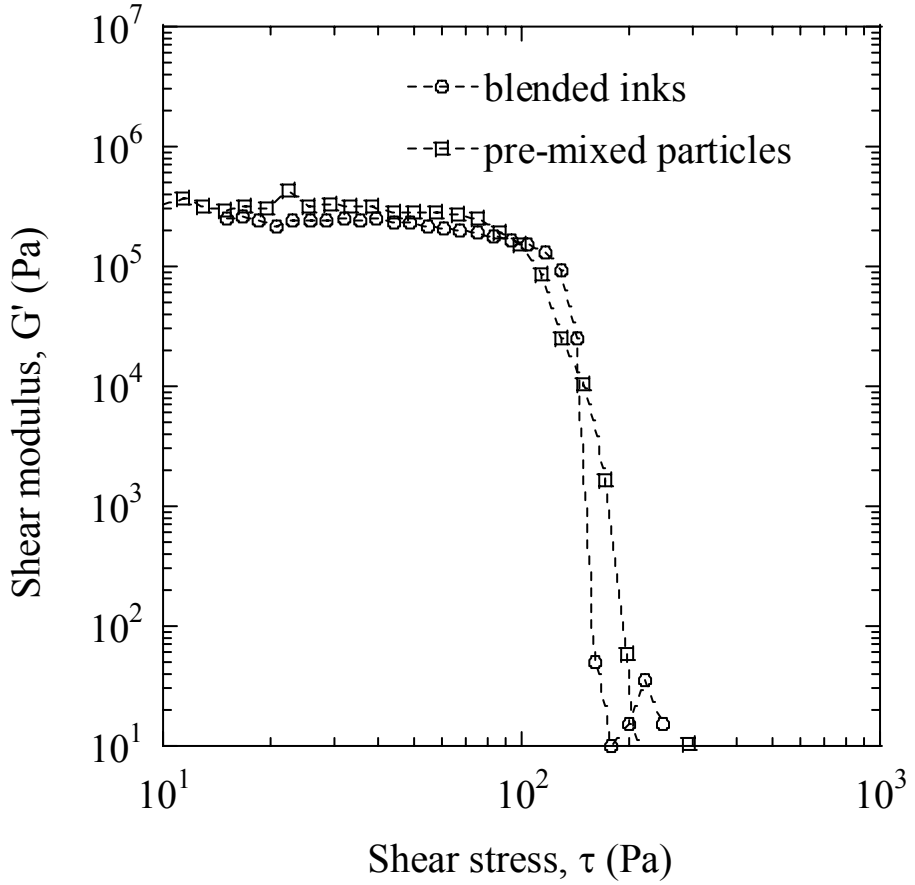


Figure A.4 Comparison of rheology of an ink mixture inks made using blended inks and a single ink using pre-mixed ceramic powders

*A.3.2. Printing and analysis*

Figure A.5 is an optical image of the multi-material samples fabricated using the robocasting process in (a) oil and (b) dried after removal from the oil in ambient air. For visual characterization the three stock inks of barium titanate, strontium titanate, and barium zirconate were labeled with green, red, and blue dyes respectively.

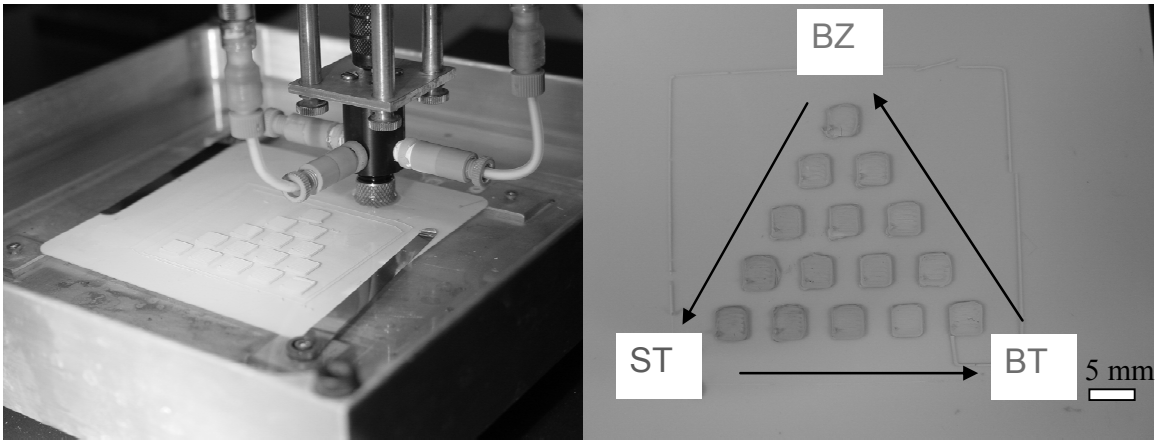


Figure A.5 Robocast multi-material ternary array deposited in (a) oil and (b) after drying

To evaluate the efficacy of the mixing nozzle on the blending of the inks before deposition, the $BaTiO_3$-$SrTiO_3$ leg from the ternary array was removed and the cross sectional region for each sample was examined using back scatter electron microscopy. The results have been presented in Figure A.6 where the dark regions represent barium rich ink and the light regions represent the strontium rich ink.

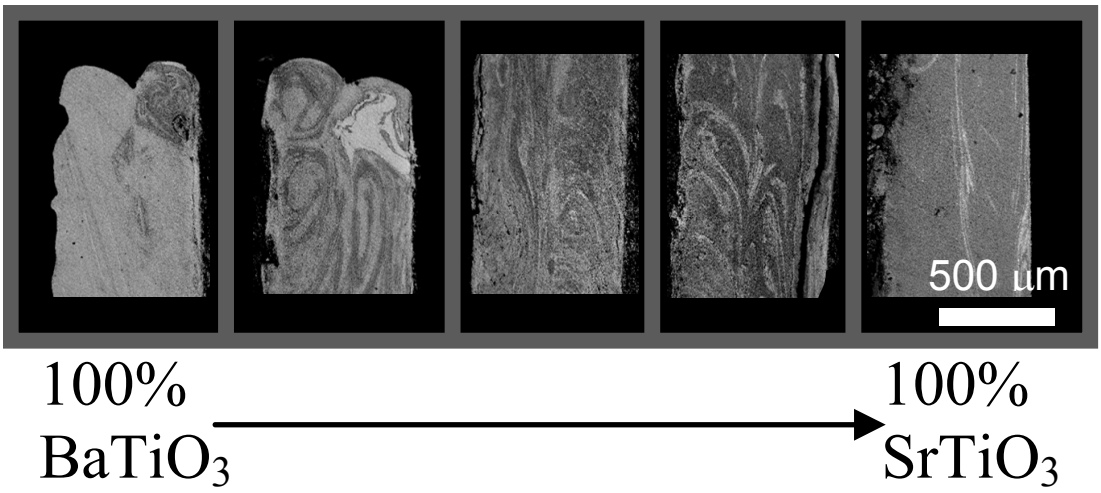


Figure A.6 A backscatter image showing the distribution of barium titanate and strontium titanate in the cross section of samples examined from the barium titanate-strontium titanate leg of the ternary array

From the back scatter analysis it was estimated that while the correct ratio of the two materials (i.e. 1:0, 3:1, 1:1, 1:3, and 0:1) was maintained in the deposited samples mixing was far from ideal as evident from the striations, approximately 10-20 μm in diameter, present to a large degree in the mixed composition samples. This effect could be attributed to the small Reynolds numbers (<<1) and the extremely high viscosities of the gels (800 Pa.s) that were being mixed. Short residence times, on the order of microseconds, for constituent streams in the mixing chamber did not allow sufficient time for mixing at the particle level.

## A.4. Conclusions

A ternary array of $BaTiO_3$-$SrTiO_3$-$BaZrO_3$ dielectric ceramics was printed using a single pass direct write method using robocasting. Constituent inks were blended *in-situ* and co-extruded for multiple composition samples. While the desired ratio of samples was achieved in samples, laminar flows and short residence times were believed to be responsible for non-homogeneous mixing. It is recommended to study the agitator rotation speed and linear speed of printing on the mixing efficiency. This technique may be useful for combinatorial screening for properties of ceramic mixtures in the future.

VITA

Sarosh Srikanth Nadkarni

Candidate for the Degree of

Doctor of Philosophy

Thesis: DESIGN, ASSEMBLY AND CHARACTERIZATION OF THREE-DIMENSIONAL PHOTONIC BAND GAP STRUCTURES FABRICATED WITH BARIUM TITANATE: STRONTIUM TITANATE: BARIUM ZIRCONATE MIXTURES

Major Field: Chemical Engineering

Biographical:

Personal Data: Sarosh Nadkarni was born on 29th of October, 1978 in Pune, India to Shrikant and Geeta Nadkarni

Education: He received his Bachelor of Technology in Chemical Engineering from Osmania University, Hyderabad, India in 2001. He completed the requirements for the Doctor of Philosophy in Chemical Engineering at Oklahoma State University in December, 2006.

Experience: Employed at Oklahoma State University, Department of Chemical Engineering as Teaching Assistant 2001- 2004
Employed at Oklahoma State University, Department of Chemical Engineering as Doctoral Research Associate, 2001-2006.

Professional Memberships: The American Ceramic Society
Indian Institute of Chemical Engineers

Name: Sarosh Srikanth Nadkarni Date of Degree: December, 2006

Institution: Oklahoma State University Location: Stillwater, Oklahoma

Title of Study: DESIGN, ASSEMBLY AND CHARACTERIZATION OF THREE-DIMENSIONAL PHOTONIC BAND GAP STRUCTURES FABRICATED WITH BARIUM TITANATE: STRONTIUM TITANATE: BARIUM ZIRCONATE MIXTURES

Pages in Study: 174 Candidate for the Degree of Doctor of Philosophy
Major Field: Chemical Engineering

Scope and Method of Study: Ternary mixtures of barium titanate (BT), strontium titanate (ST) and barium zirconate (BZ) were investigated as materials for three-dimensional, periodic, layer-by-layer structures used as photonic crystals. Highly concentrated aqueous based ceramic gels were formulated using colloidal processing and printed using an extrusion based direct write technique called robocasting. Bulk films with a range of molar ratios were printed and their electrical characteristics determined at low frequencies to develop composition-properties maps. Based on this data, face centered tetragonal lattices were printed with varying compositions and their frequency dependent transmission spectra determined using time domain terahertz spectroscopy. The experimentally obtained band structures were compared to those obtained by modeling using the transfer matrix method.

Findings and Conclusions: It was found that a cationic polyelectrolyte salt, poly(ethylenime) was an effective flocculant for aqueous slurries of co-dispersed barium titanate, strontium titanate, and barium zirconate ceramics powders dispersed using ammonium polyacrylate and yielded inks suitable for fabrication of fine lattice structures. After a pre-shear, gel modulus recovery was found to follow a two step recovery process. An instantaneous recovery on the order of 1-2 seconds and then a gradual recovery over a much longer period (at least ½ h). The gradual recovery was found to obey an exponential decay curve with the decay constant being inversely proportional to gel strength. For ternary mixtures of barium titanate: strontium titanate: barium zirconate it was discovered that compositions rich in barium titanate exhibited the highest dielectric constants, loss and tunability whereas all these properties decreased significantly as the barium titanate phase was diluted. The Curie temperature also shifted to lower temperatures as the composition became richer in $[Sr^{2+}]$ or $[Zr^{4+}]$. A range of dielectric properties were thus obtained by mixing the three dielectrics in different molar ratios. Some mixtures were used to fabricate layer by layer photonic crystals using an extrusion based robotic deposition technique called robocasting. Transmission measurements, done using terahertz time domain spectroscopy, indicated photonic band gaps that were within 10% of the predicted results obtained by using the transfer matrix method for computation of transmission spectra.

ADVISER'S APPROVAL: Dr. James E. Smay